

Doctorate Dissertation

博士論文

Reexamination of Great Earthquakes along the Japan
Trench Based on Geological Analysis and Numerical
Modeling for Tsunami Deposits

(津波堆積物の地質学的分析及び数値モデリングに
基づいた日本海溝沿いの巨大地震の再検討)

A Dissertation Submitted for Degree of Doctor of Philosophy

October 2018

平成30年10月博士（理学）申請

Department of Earth and Planetary Science, Graduate School of Science,

The University of Tokyo

東京大学大学院理学系研究科地球惑星科学専攻

Satoshi Kusumoto

楠本 聡

Abstract

In this thesis, the M9-class great earthquakes that have occurred along the Japan Trench, especially the 869 Jogan earthquake, are reexamined using a geological analysis of tsunami deposits and numerical modeling of tsunami sediment transportation.

Chapter 1 summarizes the world's earthquakes that have caused large tsunamis, as well as the history, current status, limitations of tsunami deposit studies, and tsunami sediment transport modeling. Chapter 2 summarizes the great earthquakes along the Japan Trench, previous studies of them, and the sedimentary environment and previous studies of three study sites (Idagawa lowland, Minami-Soma City in Fukushima Prefecture, the Sendai plain in Miyagi Prefecture, and the Numanohama marsh, Miyako City in Iwate Prefecture). In this study, both a geological survey and sediment transport modeling were performed for at the Idagawa lowland, and the modeling results were compared with previous geological surveys for the Sendai plain and Numanohama marsh.

Chapter 3 summarizes the methods (i.e., sedimentological analysis, microfossil and diatom analysis, radiocarbon dating, Bayesian age-depth model for depositional ages, and recurrence intervals of event deposits) for the tsunami deposit surveys. After that, the methodology for the hydrodynamic sediment transport modeling is described in detail. The sediment transport modeling is a method of solving the equations of continuity in the suspended load and bedload layers and the exchange rate between these layers. This method considers a single grain size, but the present study applied it to multiple-sized sand particles. Three representative diameters were selected based on a grain size distribution measured from tsunami deposits and modeling performed after estimating model parameters. Tsunami reduction due to the effect of coastal forest is also modeled and verified.

Chapter 4 summarizes the results of tsunami deposit surveys at the Idagawa lowland.

Seven sandy event layers from the past 3800 years were identified. Based on the sedimentological structure of the event deposits and diatom assemblages above and below event deposits, five of them were judged as being caused by tsunamis, and the others by storm surges. The average recurrence interval for the tsunamis was 560-950 years, and the depositional age of the second event layer was constrained between AD 800 and AD 1310. Thus it might correspond to the 869 Jogan tsunami deposits. Two storm deposits were also formed just after the tsunami events (<200 years) and the sediment environment inferred from diatom assemblages was a marine to brackish inner bay or lagoon. Therefore the large tsunamis might have collapsed a sand dune and the lagoon or mudflats were more susceptible to storm impacts before the redevelopment of the dune.

Chapter 5 summarizes the results of the two-dimensional tsunami inundation simulation and the one-dimensional sediment transport modeling applied to the 2011 Tohoku tsunami deposits at the Idagawa lowland, Sendai plain, and Numanohama marsh. Eleven scenarios with variable slip amounts and distributions based on previous models were prepared and the results were compared with the observations. Regarding the Idagawa lowland and Sendai plain, the results from previous model well matched with the observations by considering tsunami reduction due to coastal forest. Conversely, the results were not able to reproduce the observations of the Numanohama marsh, probably because the tsunami deposit was coarser than those of the Idagawa lowland and the Sendai plain. In addition to the effects of coastal forest, the effects of duration of the sediment transport modeling, water depth at the offshore boundary and model parameters (i.e., coefficients of bedload and pick-up rates) are also examined and the model validity, sensitivity, and accuracy of estimating the source model of an earthquake from tsunami deposit data is discussed.

Chapter 6 summarizes the estimated magnitude and source location of the 869 Jogan

earthquake derived from the tsunami inundation simulation and sediment transport modeling to the tsunami deposits at the Idagawa lowland and the Sendai plain. The results from models with a large slip area off Miyagi Prefecture reproduced the observations. Thus, it is concluded that the 869 Jogan earthquake was an M9-class giant earthquake, but the magnitude and fault length was slightly smaller than the 2011 Tohoku earthquake.

Chapter 7 presents the conclusions for this thesis. The recurrence interval for giant earthquakes along the Japan Trench and the limitations of evaluating earthquakes from tsunami deposits and numerical simulation are discussed.

Contents

CHAPTER 1. Introduction	1
1-1. Background	1
1-2. History of Tsunami Deposit Study	2
1-3. Current Issues of Tsunami Deposit Study	4
1-4. Purpose of This Study	5
CHAPTER 2. Study Sites.....	7
2-1. Overview	7
2-2. Earthquake and Tsunami History of Japan Trench.....	7
2-3. Idagawa Lowland, Fukushima Prefecture	10
2-4. Sendai Plain, Miyagi Prefecture	16
2-5. Numanohama Marsh, Iwate Prefecture	20
CHAPTER 3. Methods and Data	24
3-1. Geological Analysis	24
3-1-1. Field Survey and Geological Core Sampling	24
3-1-2. Sedimentological Analysis.....	25
3-1-3. Nannofossil Analysis	26
3-1-4. Radiocarbon Dating.....	27
3-1-5. Age-Depth Models.....	27
3-2. Numerical Model of Tsunami Sediment Transport.....	31
3-2-1. Tsunami Hydrodynamics	31
3-2-2. Sediment Transport	32
3-2-2-1. Continuity Equation in the Bedload Layer	33
3-2-2-2. Continuity Equation in the Suspended Load Layer	34

3-2-3. Pick-up Rate	35
3-2-4. Bedload Rate	36
3-2-5. Settling Velocity.....	36
3-2-6. Critical Shear Velocity.....	37
3-2-7. Approach for Multiple-sized Sand Particles	39
3-3. Bathymetry and Topography.....	40
3-4. Coastal Forest.....	41
3-5. Initial Parameters and Boundary Conditions.....	42
3-6. Tsunami Source Models	42
3-7. Model Accuracy.....	44
CHAPTER 4. Tsunami Deposit Survey at the Idagawa Lowland ..	
.....	46
4-1. Sedimentary Facies and Stratigraphy	46
4-2. Lateral Continuity of Event Deposits	56
4-3. Diatom and Foraminiferal Assemblages	58
4-4. Identification of Tsunami Deposits.....	62
4-5. Depositional Ages and Recurrence Intervals	65
4-6. Sedimentary Environment Changes Inferred from Nannofossil Assemblages	70
4-7. Comparison with Historical Earthquakes	71
CHAPTER 5. Numerical Modeling of Tsunami Inundation and Sediment Transport for the 2011 Tohoku Tsunami	74
5-1. Tsunami Inundation.....	74
5-2. Erosion and Deposition	83
5-3. Sediment Thickness	85

5-4. Time Duration	92
5-5. Water Depths at the Offshore Boundary	94
5-6. Model Parameters –Bedload and Pick-up Rates–	97
5-7. Model Validity, Sensitivity, and Accuracy	99
CHAPTER 6. Application to the 869 Jogan Tsunami Deposit ..	102
6-1. Model Uncertainties.....	102
6-2. Comparison Between Tsunami Inundation Distances and the Maximum Extents of the 869 Jogan Tsunami Deposits	105
6-3. Uncertainty for Beach Ridge Elevation	107
6-4. Comparison with the Observations	111
CHAPTER 7. Conclusion.....	114
Acknowledgments	116
References	117

List of Figures

Fig. 1-1. Tsunami events with $M > 8$ earthquakes since 1990	1
Fig. 2-1. Rupture zones for major historical earthquakes and slip distribution of the 2011 Tohoku earthquake	8
Fig. 2-2. Location and topographic profiles of the Idagawa lowland in Fukushima Prefecture	12
Fig. 2-3. Historical topographic maps and aerial photographs of the Idagawa lowland	13
Fig. 2-4. The 2011 Tohoku tsunami heights and inundation limit in the Idagawa lowland	14
Fig. 2-5. Tsunami damages to the Idagawa lowland	15
Fig. 2-6. Location and topographic profiles of the Sendai plain in Miyagi Prefecture	16
Fig. 2-7. The observed 2011 Tohoku tsunami run-up heights and inundation limit on the Sendai plain.....	17
Fig. 2-8. Sampling locations and sediment thicknesses for the 2011 and 869 Jogan tsunami deposits along the Sendai airport transect	18
Fig. 2-9. Grain size distributions for the 2011 Tohoku tsunami deposits in the Sendai plain	19
Fig. 2-10. Location and topographic profiles of the Numanohama marsh in Iwate Prefecture	20
Fig. 2-11. The observed 2011 Tohoku tsunami run-up heights and inundation limit in the Numanohama marsh.....	21
Fig. 2-12. Sampling locations and sediment thicknesses for the 2011 Tohoku and 869 Jogan tsunami deposits along the Numanohama marsh transect	22

Fig. 2-13. Grain size distributions for the 2011 Tohoku and 869 Jogan tsunami deposits in the Numanohama marsh.....	23
Fig. 3-1. Sampling locations and topographic profiles for the Idagawa lowland.....	24
Fig. 3-2. Diagram of sediment transport modeling due to tsunami.....	32
Fig. 3-3. Model parameters for different grain size.....	38
Fig. 3-4. Approach for sediment transport modeling of multiple grain sizes.....	40
Fig. 3-5. Diagram of the simulated coastal forest.....	42
Fig. 3-6. Fault models for initial tsunami source.....	44
Fig. 4-1. Photograph, CT image, and simple sketch with sedimentary structures of the sediment at the cores A02, A04, A06, A08, and B01	46
Fig. 4-2. Vertical variation in grain size distributions of the EV1 unit.....	49
Fig. 4-3. Vertical variation in grain size distributions of the EV2 unit.....	50
Fig. 4-4. Vertical variation in grain size distributions of the EV3 unit.....	51
Fig. 4-5. Vertical variation in grain size distributions of the EV4 unit.....	51
Fig. 4-6. Vertical variation in grain size distributions of the EV5 unit.....	52
Fig. 4-7. Vertical variation in grain size distributions of the EV6 unit.....	53
Fig. 4-8. Vertical variation in grain size distributions of the EV7 unit.....	54
Fig. 4-9. Grain size distributions of event and ordinary deposits.....	54
Fig. 4-10. Stratigraphic comparison along transect A-A'	56
Fig. 4-11. Stratigraphic comparison along transect B-B'	58
Fig. 4-12. Diatom assemblages in the core A02	60
Fig. 4-13. Micrographs of typical diatoms in the core A02.....	61
Fig. 4-14. Vertical changes in appearance levels and count number for <i>Coccoliths</i> , <i>Sponge spicules</i> , and <i>Slicoflagellates</i> in the core A02.....	62
Fig. 4-15. Photographs, CT images, and sketches of the EV2 and EV3 units	64

Fig. 4-16. Age-depth models with different k values	67
Fig. 4-17. Depositional ages of event deposits and time intervals between event deposits estimated from the cores A01 and B02	69
Fig. 4-18. Summary of reported tsunami deposits and historical earthquakes in northern Fukushima and southern Miyagi Prefectures	73
Fig. 5-1. Maximum sea surface displacements for each model.....	75
Fig. 5-2. The calculated tsunami waveforms of each model incident from the offshore boundary of the computational domain in the Idagawa lowland, Sendai plain, and Numanohama marsh.....	75
Fig. 5-3. Topographic profile and maximum water surface for each model along transect in the Idagawa lowland	77
Fig. 5-4. Maximum flow depth computed from Model 1 and distributions of tsunami deposits in the Idagawa lowland	78
Fig. 5-5. Topographic profile and maximum water surface for each model along transect in the Sendai plain.....	80
Fig. 5-6. Maximum flow depth computed from Model 1 and distributions of tsunami deposits in the Sendai plain.....	80
Fig. 5-7. Topographic profile and maximum water surface for each model along transect in the Numanohama marsh.....	82
Fig. 5-8. Maximum flow depth computed from Model 1 and distributions of tsunami deposits in the Numanohama marsh	82
Fig. 5-9. Comparison of the observed and simulated sediment thickness with a single grain size of the 2011 Tohoku tsunami deposits in the Idagawa lowland	86
Fig. 5-10. Comparison of the observed and simulated sediment thickness with multiple grain sizes of the 2011 Tohoku tsunami deposits in the Idagawa lowland	87

Fig. 5-11. Comparison of the observed and simulated sediment thickness with a single grain size of the 2011 Tohoku tsunami deposits in the Sendai plain	88
Fig. 5-12. Comparison of the observed and simulated sediment thickness with multiple grain sizes of the 2011 Tohoku tsunami deposits in the Sendai plain	89
Fig. 5-13. Comparison of the observed and simulated sediment thickness with a single grain size of the 2011 Tohoku tsunami deposits in the Numanohama marsh	91
Fig. 5-14. Comparison of the observed and simulated sediment thickness with multiple grain sizes of the 2011 Tohoku tsunami deposits in the Numanohama marsh.....	91
Fig. 5-15. Comparison of the observed and simulated sediment thickness with the two-dimensional modeling of the 2011 Tohoku tsunami deposits in the Numanohama marsh	92
Fig. 5-16. Time series of the simulated sediment thickness with distances from the coast in the Idagawa lowland and Sendai plain.....	93
Fig. 5-17. Relationship between the values of geometric mean and water depth at the offshore boundary	95
Fig. 5-18. The calculated sediment thickness for different water depths in the Idagawa lowland, Sendai plain, and Numanohama marsh	96
Fig. 5-19. Different coefficients of bedload and pick-up rates.....	98
Fig. 5-20. Comparison between the observed and calculated values with different coefficient of bedload and pick-up rates	98
Fig. 5-21. The simulated sediment thickness for different coefficients of bedload and pick-up rates	99
Fig. 5-22. Summary of results for model validity, sensitivity, and accuracy of sediment transport modeling using the 2011 Tohoku tsunami deposits	101
Fig. 6-1. Ground surface in the Idagawa lowland in AD 869.....	103

Fig. 6-2. Ground surface in the Sendai plain in AD 869	104
Fig. 6-3. Ground surface in the Numanohama marsh in AD 869	104
Fig. 6-4. Maximum water surfaces for each model along transects in the Idagawa lowland, Sendai plain, and Numanohama marsh	106
Fig. 6-5. The <i>K</i> values for different beach ridge elevations	107
Fig. 6-6. The observed and simulated sediment thickness for different beach ridge elevations in the Idagawa lowland	108
Fig. 6-7. The observed and simulated sediment thickness for different beach ridge elevations in the Sendai plain.....	109
Fig. 6-8. Comparison of the observed and simulated sediment thickness of the 869 Jogan tsunami deposits when the topographic data of a 1 m high beach ridge with/without a coastal forest are used in the Idagawa lowland	112
Fig. 6-9 Summary of the comparison between the simulated tsunami inundation distance and sediment thickness and the observation of the 869 Jogan tsunami deposits.....	113

List of Tables

Table 3-1. Sampling locations for the Idagawa lowland	25
Table 3-2. Distances between stratigraphic marker layers	28
Table 3-3. Poisson parameter for each core.....	30
Table 3-4. Event-Free Depth scale for the cores A01 and B02	31
Table 3-5. Model parameters for the 2011 Tohoku tsunami deposits for a single grain size	38
Table 3-6. Model parameters for the 2011 Tohoku tsunami deposits for multiple grain sizes.....	39

Table 3-7. Model parameters for the 869 Jogan tsunami deposits for multiple grain sizes	39
Table 3-8. Tsunami source models examined in this study	43
Table 4-1. Sedimentological structures of event deposits	55
Table 4-2. Detailed results of radiocarbon dating.....	66
Table 4-3. Depositional ages for different k values	68
Table 4-4. Recurrence intervals of event deposits for different k values.....	69
Table 5-1. The 2011 tsunami inundation heights and inundation areas computed from each model in the Idagawa lowland	77
Table 5-2. The 2011 tsunami inundation heights and inundation areas computed from each model in the Sendai plain.....	79
Table 5-3. The 2011 tsunami inundation heights and inundation areas computed from each model in the Numanohama marsh	81
Table 5-4. Comparison of the simulated tsunami heights, inundation distance, and inundation area with the observations of the 2011 Tohoku tsunami deposits.....	83
Table 5-5. Total net deposition and erosion for Model 1.....	85
Table 5-6. Statistical comparison of the observed and computed sediment thickness in the Idagawa lowland	86
Table 5-7. Statistical comparison of the observed and computed sediment thickness in the Sendai plain.....	88
Table 5-8. Statistical comparison of the observed and computed sediment thickness in the Numanohama marsh.....	90
Table 6-1. Statistical comparison of the observed and simulated sediment thickness for different beach ridge elevations in the Idagawa lowland.....	110
Table 6-2. Statistical comparison of the observed and simulated sediment thickness for	

different beach ridge elevations in the Sendai plain	110
Table 6-3. Statistical comparison of the observed and simulated sediment thickness with/without a coastal forest in the Idagawa lowland.....	112

CHAPTER 1. Introduction

1-1. Background

Tsunamis can be generated by earthquakes, volcanic eruptions, landslides, glacier calvings, and meteorite impacts. Large earthquakes with tsunamis occur most frequently in the Pacific Ocean because of seismic and volcanic activity associated with tectonic plate boundaries along the Pacific Ring of Fire (Fig. 1-1).

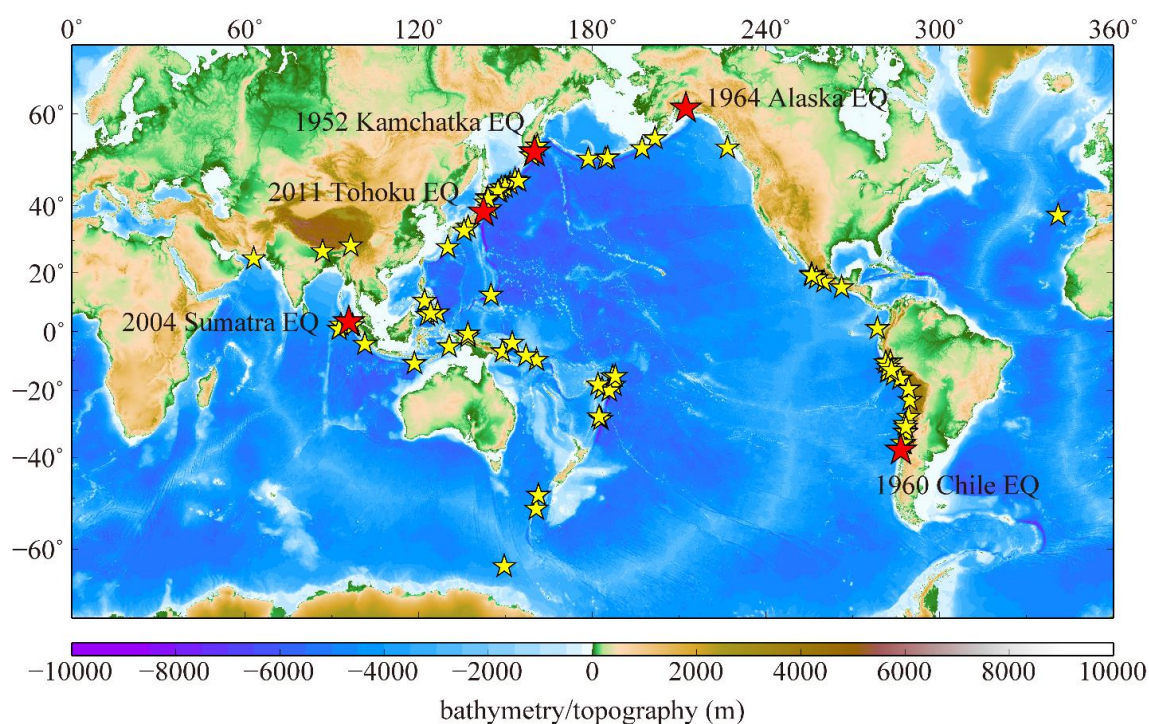


Figure 1-1. Tsunami events with $M > 8$ earthquakes since 1990 (NGDC/WDS Global Historical Tsunami Database: http://www.ngdc.noaa.gov/hazard/tsu_db.shtml). The red and yellow stars show the hypocenters of M9-class and M8-class earthquakes, respectively.

Particularly, the 1952 Kamchatka earthquake (M_w 9.0) at 16:58:30 UTC on 4 November, the 1960 Chile earthquake (M_w 9.5) at 19:11:14 UTC on 22 May, the 1964 Alaska earthquake (M_w 9.2) at 03:36 UTC on 28 March, the 2004 Sumatra-Andaman earthquake

(Mw 9.1-9.3) at 00:58:53 UTC on 26 December, and the 2011 Tohoku earthquake (Mw 9.0) at 05:46:24 UTC on 11 March caused huge tsunamis that resulted in catastrophic damage to coastal areas. Onshore and offshore sediment deposits, generally called “tsunami deposits”, were formed by these tsunamis. Tsunami deposits generally consist of sand or mud and contain a significant amount of information. For example, the distribution may enable for an estimation of the tsunami inundation distance. The biggest advantage of tsunami deposits is that they enable us to be able to quantitatively evaluate paleo-tsunamis where no instrument observations or historical records exist. Therefore, this study investigates paleo-tsunami deposits to trace the history of prehistorical tsunamis.

1-2. History of Tsunami Deposit Study

The study of tsunami deposits started after the 1960 Chile earthquake. The sediment transport (sand deposition and erosion) due to the tsunami was first observed between Hachinohe and Kuji cities, between Taro and Kamaishi cities, and between Ofunato and Shigawa cities in the Sanriku coastal region by Kon'no (1961), Iwai *et al.* (1961), Onuki *et al.* (1961), and Kitamura *et al.* (1961). They concluded that the sediment can be classified as either crumble deposits, over-flow-scour deposits, passage-spread deposits, deposits of suspended materials, adhesive materials, deposits of graded beddings of mono- and multicycle, deposits of drifted materials, or deposits of evaporates. The sediment might have also originated from the seafloor of a harbor on the basis of nannofossil assemblages. After the 1983 Sea of Japan earthquake, Minoura *et al.* (1987) proposed that traces of prehistoric earthquakes with huge tsunamis are recorded in the sediments of coastal regions. In the same year, tsunami deposits were also confirmed in wetlands in the northwestern part of the United States and southwestern part of Canada

(Atwater, 1987), and paleo-tsunami deposit studies began globally. At the same time, numerical modeling of sediment transport due to tsunamis was performed by coastal engineers (e.g., van Rijn, 1984a; van Rijn, 1984b; Watanabe *et al.*, 1984; van Rijn, 1993; Soulsby, 1997; Takahashi *et al.*, 1992; 1993; 1999).

Sixteen major tsunamis occurred in the 1990s. The characteristics of the tsunami deposits have been analyzed in many field surveys (e.g., Clague and Bobrowsky, 1994; Benson *et al.*, 1997; Gelfenbaum and Jaffe, 2003). In Japan, tsunami deposit surveys were conducted around the Sagami Trough (Fujiwara *et al.*, 1997; 1999; 2000), on the Pacific coast of the Tohoku region (Minoura and Nakaya, 1991; Minoura *et al.*, 1994), and the eastern Pacific coast of Hokkaido (e.g., Hirakawa *et al.*, 2000; Nanayama *et al.*, 2003a; 2003b), and prehistoric tsunami deposits were identified in the alluvial plains and lake sediments. The tsunami deposit with the A.D. 869 Jogan earthquake, which is considered as a predecessor of the 2011 Tohoku-Oki earthquake, was first confirmed in the Ishinomaki and Sendai plains (Abe *et al.*, 1990; Minoura and Nakaya, 1991).

By the time of the 2004 Indian Ocean tsunami, the importance of tsunami deposits for earthquake evaluation was widely accepted and as a result detailed surveys were performed after the event. The results have been used to clarify the recurrence interval of megathrust earthquakes occurring in the Nankai, Suruga, Sagami Troughs (e.g., Usami, 2003; Fujiwara, 2004; Nanayama and Shigeno, 2006; Komatsubara and Fujiwara, 2007), and Japan Trench (e.g., Sawai *et al.*, 2007; Shishikura *et al.*, 2007). In addition, tsunami hazard risks and historical earthquakes have been quantitatively evaluated using tsunami deposits and numerical simulation (e.g., Satake *et al.*, 2008; Namegaya *et al.*, 2010). Various models of forward tsunami sediment transport (Delft3D, XBeach, C-HYDRO3D, STM, TsuSedMod, and TSUFLIND) have been published and applied to a number of case studies of the 2004 Indian Ocean and 2009 Samoa tsunamis (e.g., Gelfenbaum *et al.*,

2007; Takahashi *et al.*, 2008; Apotsos *et al.*, 2011a; 2011b; 2011c; Li *et al.*, 2012; Gusman *et al.*, 2012; Tang and Weiss, 2015).

Tsunami science developed massively following the 2011 Tohoku earthquake because the tsunami run-up heights and flow speeds were obtained from the digital photographs and aerial videos taken by residents (e.g., Fritz *et al.*, 2012; Foytong *et al.*, 2013; Koshimura and Hayashi, 2012; Hayashi and Koshimura, 2013). Studies combining modern tsunami deposits and the sediment transport modeling have also been presented (e.g., Jaffe *et al.*, 2012; Sugawara *et al.*, 2014a; 2014b Gusman *et al.*, 2018). Since the 2011 Tohoku earthquake, tsunami deposits have been recognized as one of the most important factors in enabling a quantitative understanding of past tsunamis.

1-3. Current Issues of Tsunami Deposit Study

Generally, it is essential to perform the quantitative surveys on the sub-regional scale (10s or 100s of kilometers in scale) in order to estimate past tsunamis using prehistorical tsunami deposits. It is also useful to distinguish between tsunamis and the other causative events (e.g., storm surges caused by typhoons). However, the spatial distribution of survey locations are biased, in the case of northeast Japan. The Pacific coasts of Miyagi and Iwate Prefectures have been investigated, while Aomori, Fukushima, and Ibaraki Prefectures have hardly been studied. By ignoring this problem, past tsunamis may be underestimated or overlooked. The need for a geological survey in Fukushima and Ibaraki Prefectures was pointed out before the 2011 Tohoku earthquake (e.g., Satake *et al.*, 2008; The Headquarters for Earthquake Research Promotion, 2006; 2007; 2008; 2009; 2010; Sugawara *et al.*, 2012; Kusumoto *et al.*, 2018).

Recently, researchers attempted to reproduce the sediment thickness and spatial distribution of tsunami deposits from forward sediment transport modeling using tsunami

source models which is known by tsunami waveform and teleseismic body-wave inversion (e.g., Jaffe *et al.*, 2012; Sugawara *et al.*, 2014a; 2014b; Gusman *et al.*, 2018). The results are in good agreement with the observations, but the technique may not be applicable to prehistoric tsunamis because the tsunami source and inundation distance are usually unknown. Hence, the model validity, sensitivity, accuracy, and response to model parameters should be evaluated in advance.

1-4. Purpose of This Study

In this study, in order to reexamine the great earthquakes, especially the 2011 Tohoku and 869 Jogan earthquakes, along the Japan Trench, I aim to propose a new approach for estimating the magnitude of historical earthquakes and tsunamis using a combination of modern and historical tsunami deposits and sediment transport simulation for the 2011 Tohoku and 869 Jogan tsunamis.

First, the tsunami history is investigated from geological records at a coastal lowland in the central Fukushima Prefecture. In order to estimate the depositional ages and recurrence intervals of large tsunamis, the age-depth models incorporated in the OxCal program are used. These results and discussions are presented in chapter 4.

Next, the simulated results and the observations of the 2011 Tohoku tsunami deposits at the Idagawa lowland in Fukushima Prefecture, the Sendai plain in Miyagi Prefecture, and the Numanohama marsh in Iwate Prefecture are compared to assess the model validity, sensitivity, and the accuracy, and response of the model parameters used in the sediment transport modeling developed by Takahashi *et al.* (1999; 2011) and Gusman *et al.* (2012; 2018). The results and discussions are presented in chapter 5.

Finally, the tsunami source model for the 869 Jogan earthquake is investigated using tsunami inundation and sediment transport modeling and paleo-tsunami deposits in the

Idagawa lowland, Sendai plain, and Numanohama marsh. The results are discussed in chapter 6.

CHAPTER 2. Study Sites

2-1. Overview

The Pacific coast of the Tohoku region along the Japan Trench was selected for this study. This is because the following four conditions must be satisfied in order to test the performance of the sediment transport modeling: (1): M9-class earthquake with a large tsunami, (2): known tsunami source parameters, (3): Both modern and historical tsunami deposits can be investigated, (4): High-resolution topographic data before and after the megathrust earthquake are available.

2-2. Earthquake and Tsunami History of Japan Trench

Large interplate earthquakes and tsunamis occur repeatedly along the Japan Trench (e.g., Utsu, 1990; Usami, 2003). Especially, the 9 July 869 (Jogan) Tohoku, 12 December 1454 (Kyotoku) Tohoku, 2 December 1611 (Keicho) Tohoku, 15 June 1896 (Meiji) Sanriku, 3 March 1933 (Showa) Sanriku, and 11 March 2011 Tohoku earthquakes are associated with large tsunamis (Fig. 2-1).

The 869 Jogan earthquake occurred in the night of 9 July. The tsunami damage is described in “The Nihon Sandai Jitsuroku” (e.g., Watanabe, 2000; 2001; Sawai *et al.*, 2007). According to the descriptions, the tsunami quickly reached the center of Tagajo town, spread thousands of miles from the beach, and killing approximately 1,000 people. Tsunami deposits have been also identified in Iwate, Miyagi, and Fukushima Prefectures (e.g., Minoura and Nakaya, 1991; Minoura *et al.*, 2001; Sugawara *et al.*, 2001; Shishikura *et al.*, 2007; Sawai *et al.*, 2007; 2012; Ishimura and Miyauchi, 2015; Takada *et al.*, 2016; Inoue *et al.*, 2016; Kusumoto *et al.*, 2018). The estimated moment magnitude was at least 8.6 from a comparison of the distribution of tsunami deposits with tsunami inundation simulation (Satake *et al.*, 2008; Namegaya *et al.*, 2010; Namegaya and Satake, 2014).

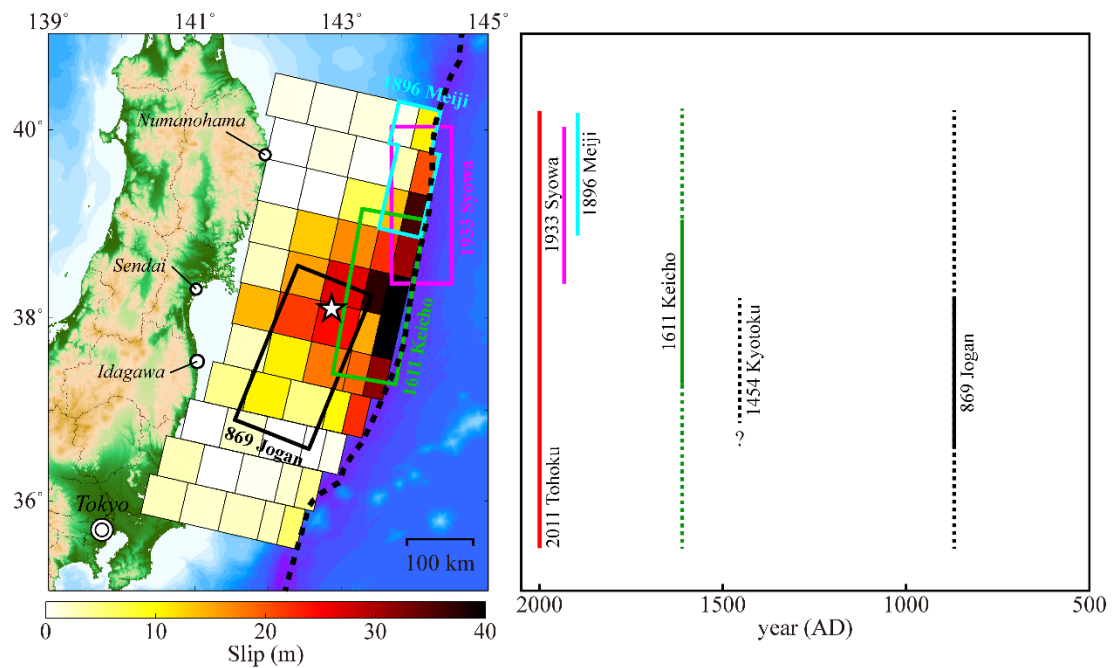


Figure 2-1. Rupture zones for major historical earthquakes and slip distribution of the 2011 Tohoku earthquake (Satake *et al.*, 2013) along the northeastern Honshu Coast. The white star is the epicenter of the 2011 Tohoku earthquake. The black, green, light blue, and purple rectangles show source areas for the 869 Jogan (Namegaya *et al.*, 2010), 1611 Keicho (Hatori, 1987), 1896 Meiji (Satake *et al.*, 2017), and 1933 Syowa (Kanamori, 1971) earthquakes, respectively. The dashed curve indicates the trench axis.

The 1454 Kyotoku earthquake occurred in the midnight of 12 December. The damage is documented in several historical records (Namegaya and Yata, 2014), but the hypocenter and magnitude are still unknown because of the limited amount of information about the earthquake. The 1611 Keicho earthquake occurred in the early afternoon of 2 December. The damages due to the earthquake and tsunami are recorded in Vizcaino's report and other historical documents (Ebina and Takahashi, 2014; Ebina and Imai, 2014). According to the literatures, the tsunami height was up to 30 m and there was over 5,000

casualties. Tsunami deposits were confirmed in Miyako, Kirikiri, and Koyadori in Iwate Prefecture (Ishimura and Miyauchi 2015; Takada *et al.*, 2016; Ishimura, 2017). Although 15-16th century event deposit was also identified at the Ishinomaki and Sendai plains in Miyagi Prefecture, there are several opinions on whether they should be attributed to the 1454 Kyotoku or 1611 Keicho tsunamis (e.g., Abe *et al.*, 1990; Sawai *et al.*, 2006; 2015). The magnitude of the 1611 Keicho earthquake was estimated as 8.1 (Hatori, 1975), but it may have been an M9-class earthquake according to recent studies (e.g., Koketsu *et al.*, 2012; Ebina, 2017; Fukuhara and Tanioka, 2017).

The 15 July 1896 Meiji tsunami was one of the most destructive seismic events in Japanese history, with approximately 22,000 casualties (Shuto *et al.*, 2007). This earthquake was a typical example of a “tsunami earthquake” which is defined as a seismic event from which the magnitude of the resultant tsunamis is significantly larger than that expected from surface waves (Kanamori, 1972; Tanioka and Satake, 1996a). The seismic magnitude ($M=6.8$) was estimated from Japanese seismological data (Utsu, 1979). The surface wave magnitude ($M_s=7.2$) was assigned from global data (Abe, 1994). The moment magnitude (M_w) was estimated as 8.0-8.2 from a comparison of aftershock activity for other large earthquakes (Utsu, 1994). The tsunami magnitude (M_t) was determined as 8.6 from global data (Abe, 1979) and 8.2 from Japanese data (Abe, 1981). The tsunami struck the Pacific coast between Hokkaido and Miyagi Prefecture and a maximum tsunami height of 38.2 m was recorded at the Ryori in Iwate Prefecture (Matsuo, 1933; Miyoshi, 1987). The 3 March 1933 Showa earthquake was a normal fault earthquake in the outer-trench slope regions (Kanamori, 1971). The moment magnitude was estimated as 8.4 (Kanamori, 1977). The tsunami associated with the earthquake struck the Sanriku coast, destroyed over 7,000 homes, and led to over 3,000 deaths (Central Meteorological Observatory, 1933). The maximum tsunami height of 28.7 m was

recorded at the Ryori in Iwate Prefecture (Kunitomi, 1933; Usami, 1966). However, there have been few studies of the 1896 Meiji and 1933 Showa tsunami deposits. This is because the tsunami deposits were not preserved as sand sheets due to human activity.

The 2011 Tohoku earthquake was the largest interplate earthquake in Japanese history. The tsunami generated by the earthquake, with heights of 11.5-15.5 m above mean sea level, caused catastrophic damage to the Fukushima Daiichi Nuclear Power Station (NPS). The damage to the emergency diesel generator resulted in a core melt-down and hydrogen explosions. The tsunami also killed almost 16,000 people and completely destroyed 83,000 homes in Japan (National Police Agency of Japan, 2018). A maximum tsunami height of 40.1 m was measured at the Ofunato in Iwate Prefecture. The 2011 tsunami deposits were observed by survey teams on the Pacific coast from Aomori to Chiba Prefecture (e.g., Fujiwara *et al.*, 2012; Goto *et al.*, 2011; 2012; Okazaki and Ooki, 2012; Sawai *et al.*, 2012b; Szczuciński *et al.*, 2012; Jaffe *et al.*, 2012; Richmond *et al.*, 2012; Yamada and Fujino, 2013; Ishimura and Miyauchi, 2015; Goto *et al.*, 2015; 2017; Shinozaki *et al.*, 2015; Ishimura, 2017; Kusumoto *et al.*, 2018).

To test, assess, and apply the sediment transport modeling, it is necessary to select study sites where both the 2011 Tohoku and 869 Jogan tsunami deposits have been identified. In this study, the Idagawa lowland, Sendai plain, and Numanohama marsh were selected as study sites representing in Fukushima, Miyagi, and Iwate Prefectures, respectively.

2-3. Idagawa Lowland, Fukushima Prefecture

The Idagawa lowland is a polder located about 12 km north of the Fukushima Daiichi NPS in Fukushima Prefecture and about 75 km south of Sendai City (Fig. 2-2). The polder extends 4.5 km east-west and 1.3 km north-south. It has an area of approximately 5.8 km²

and is located behind a 3-4 m high beach ridge that is covered with concrete blocks (Minami-soma City Education Committee, 2010). Although some trees were planted behind the ridge before the 2011 earthquake, they were mostly swept away by the tsunami. The elevation of most of the polder is below mean sea level (-1 to -2 m) extending to within about 2 km from the shore.

Relative sea level changes during the Holocene, estimated from lowland sediments between coastal ridges on the Sendai plain (Matsumoto, 1984; Matsumoto and Ito, 1998), indicate periods of high sea level (<3 m above mean sea level) about 700, 2000, and 5000 years ago, separated by periods of low sea level (<-2.5 m below mean sea level).

Holocene estuary fill sediments for the last about 10,000 years in this lowland are well preserved (Kakubari *et al.*, 2017). The sedimentary environment has been inferred to be characteristic of a lagoon or an inner bay from historical topographic maps drawn in the 19th and 20th centuries (Fig. 2-3; Minami-soma City Education Committee, 2009). Land was reclaimed between 1919 and 1925, before the Miyata and Idagawa River channels were artificially constructed in the center of the lowland. The lowland was used to grow rice until the 2011 Tohoku earthquake (Minami-soma City Education Committee, 2009).

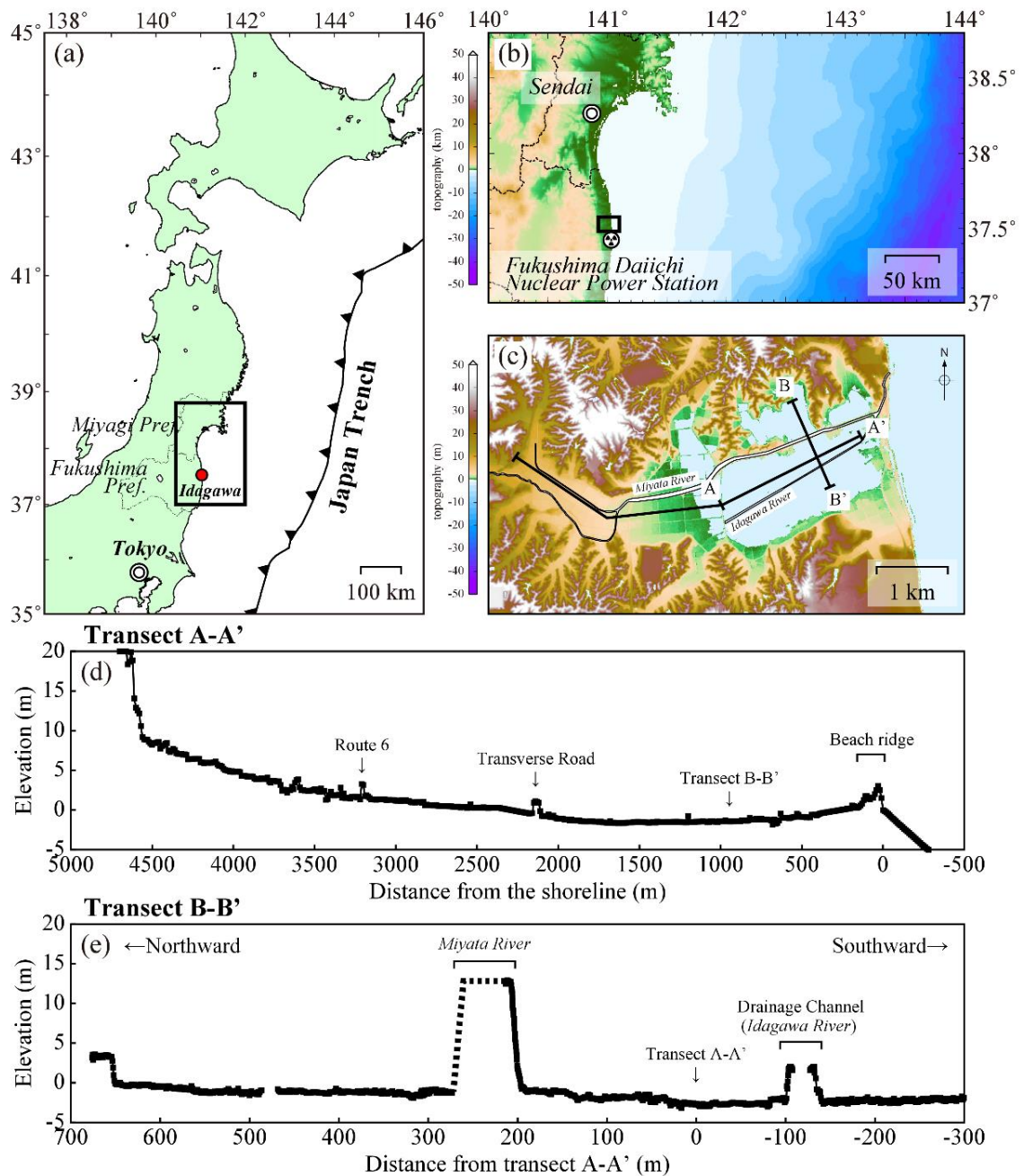


Figure 2-2. Location and topographic profiles of the Idagawa lowland in Fukushima Prefecture. (a) Overview of northeastern Japan along the Japan Trench. The red dot shows the location of the Idagawa lowland. (b) Detailed map of the Idagawa lowland, (c) Topography of the Idagawa lowland. The solid lines indicate transects (A-A' and B-B') for tsunami deposit surveys. (d), (e) Topographic profiles along transects A-A' and B-B', respectively.

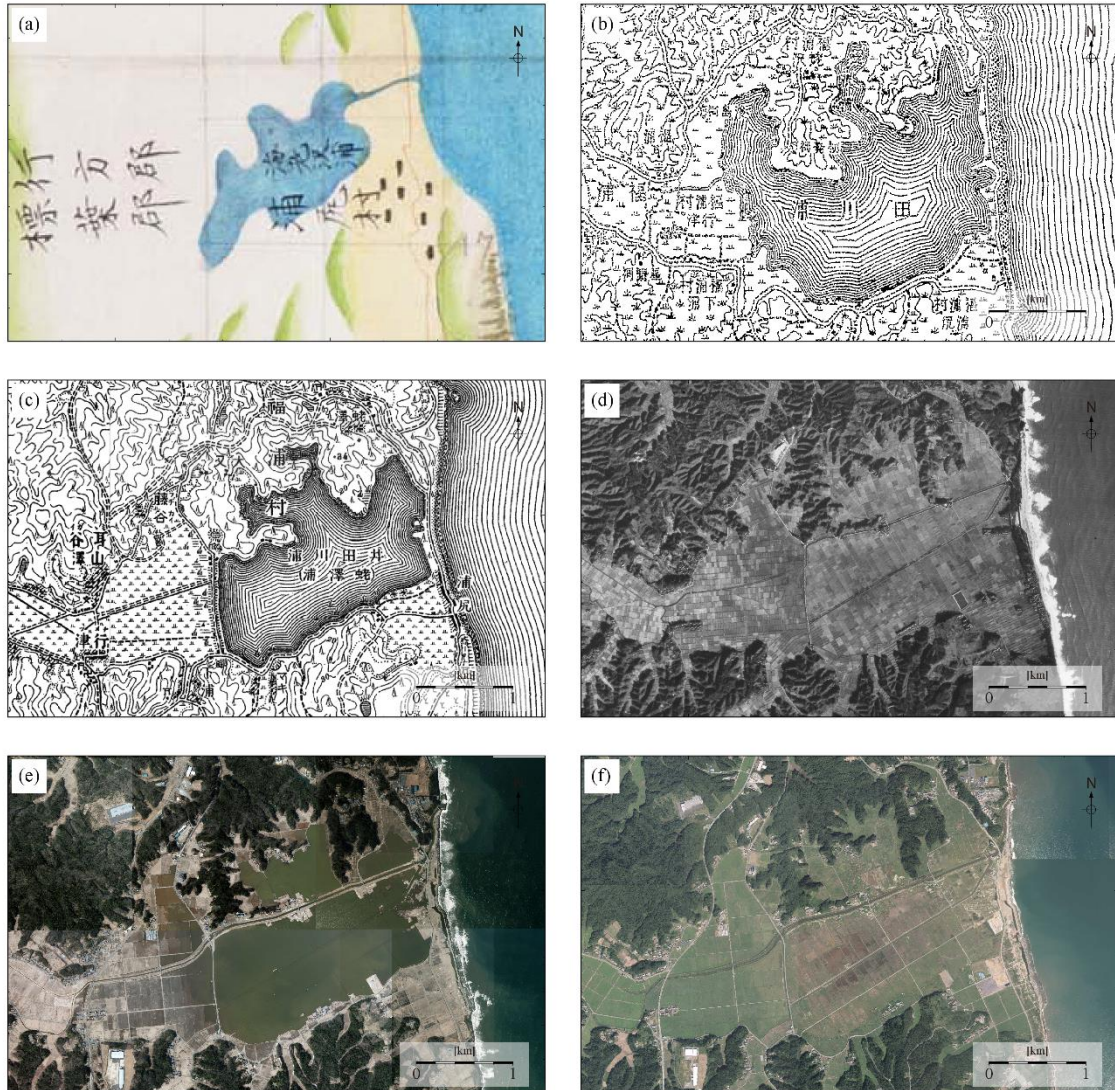


Figure 2-3. Historical topographic maps and aerial photographs of the Idagawa lowland from (a) AD 1821, (b) AD 1893, (c) AD 1910, (d) AD 1947, (e) AD 2012, and (f) AD 2016. These were provided by the Geospatial Information Authority of Japan.

According to documents from AD 1540 and the 19th century, six large storms have attacked in Miyagi and Fukushima Prefectures (Sawai *et al.*, 2007), and modern data record 64 typhoons since 195, indicating that a large storm occurs 1-2 times/year

(Kitamoto, 2018). River flooding also occurred in 1966, 1969, 1980, 1986, 1989, and 1992 along the Miyata River (Fukushima Prefecture River Council, 2004). The maximum tidal range between high and low tides is 100-150 cm, and the highest tidal level in history was 132 cm above mean sea level (Japan Meteorological Agency, 2017).

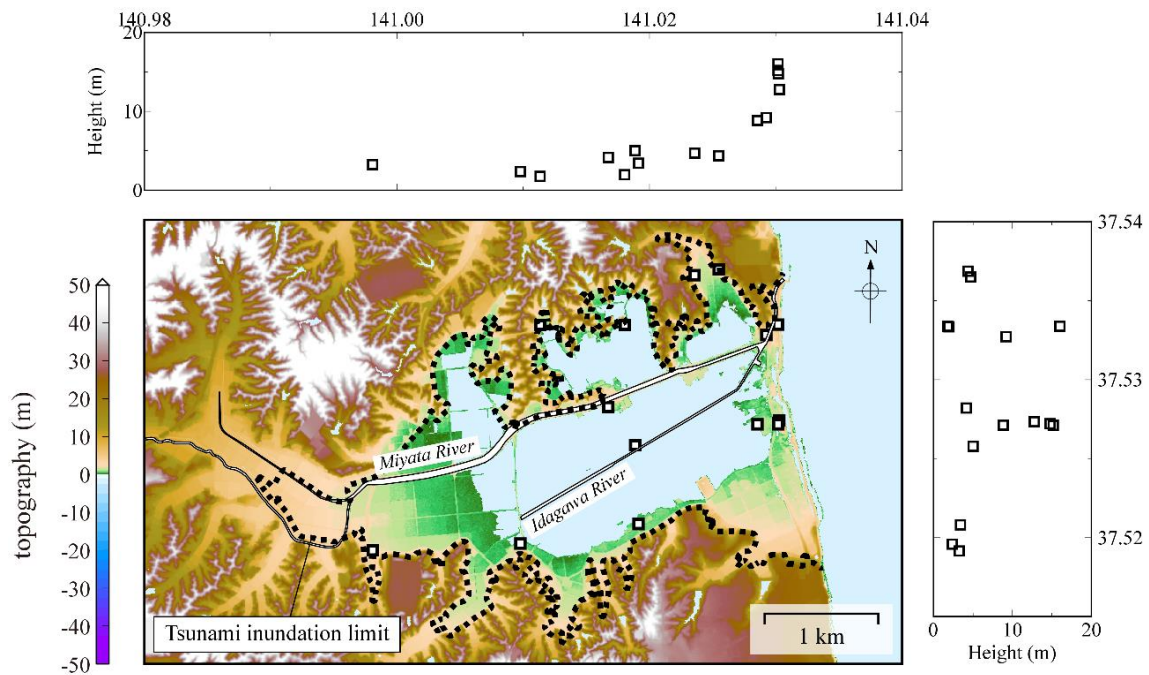


Figure 2-4. The 2011 Tohoku tsunami heights and inundation limit in the Idagawa lowland. The dotted line shows the tsunami inundation limit. The squares indicate the observed wave heights for the 2011 Tohoku tsunami (Mori *et al.*, 2012; Sato *et al.*, 2014).

The 2011 tsunami reached heights of 11-13 m around the Idagawa lowland (Mori *et al.*, 2012; Sato *et al.*, 2014). Aerial photographs indicate that the tsunami inundated an area of about 4.7 km² up to about 3.7 km from the coast (Fig. 2-4; Association of Japanese Geographers, 2011). Oota and Hoyanagi (2014) and Oota *et al.* (2017) have discussed in detail the sedimentary patterns, depositional processes and sedimentary thickness associated with the 2011 Tohoku tsunami deposit in the lowland. The tsunami completely destroyed houses, coastal structures and a drainage pump facility near the shoreline (Fig.

2-5). Because of the damage to the drainage facility, which pumped water from the lowland, the lowland was submerged between 2011 and 2014 until the facility was repaired. The current environment is a wetland.

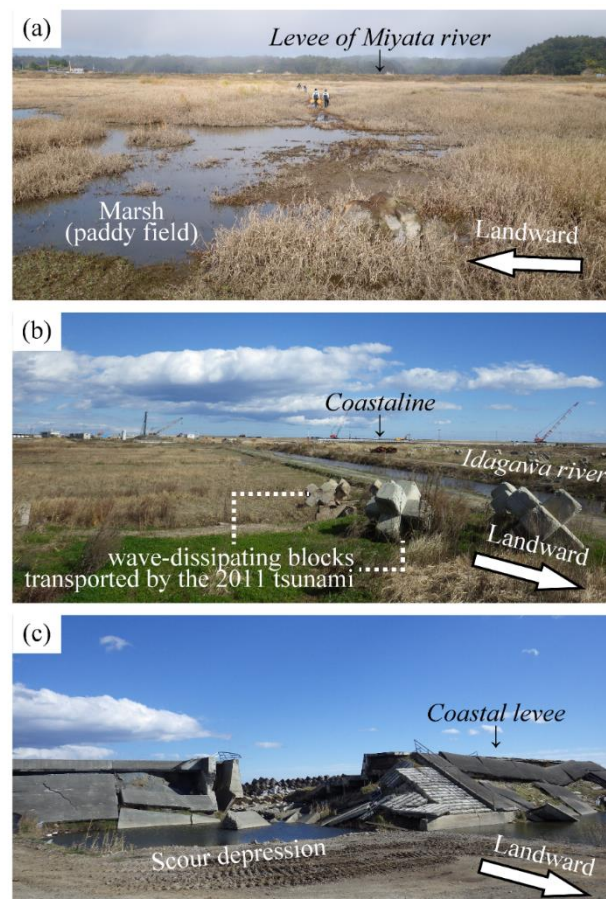


Figure 2-5. Tsunami damages to the Idagawa lowland. The photographs show (a) the center of the lowland, (b) the transverse road along the Idagawa River, and (c) coastal protection.

Several studies have investigated the tsunami deposits in this lowland both before and after the 2011 tsunami, and the tsunami recurrence interval has been estimated to be approximately 600 years (Goto and Aoyama, 2005a, 2005b; Oikawa *et al.*, 2011; Kakubari *et al.*, 2017). However, these studies relied on a small number of cores and samples.

2-4. Sendai plain, Miyagi Prefecture

The Sendai plain is an alluvial plain with sandy beach ridges between Sendai and Natori Cities in Miyagi Prefecture (Fig. 2-6).

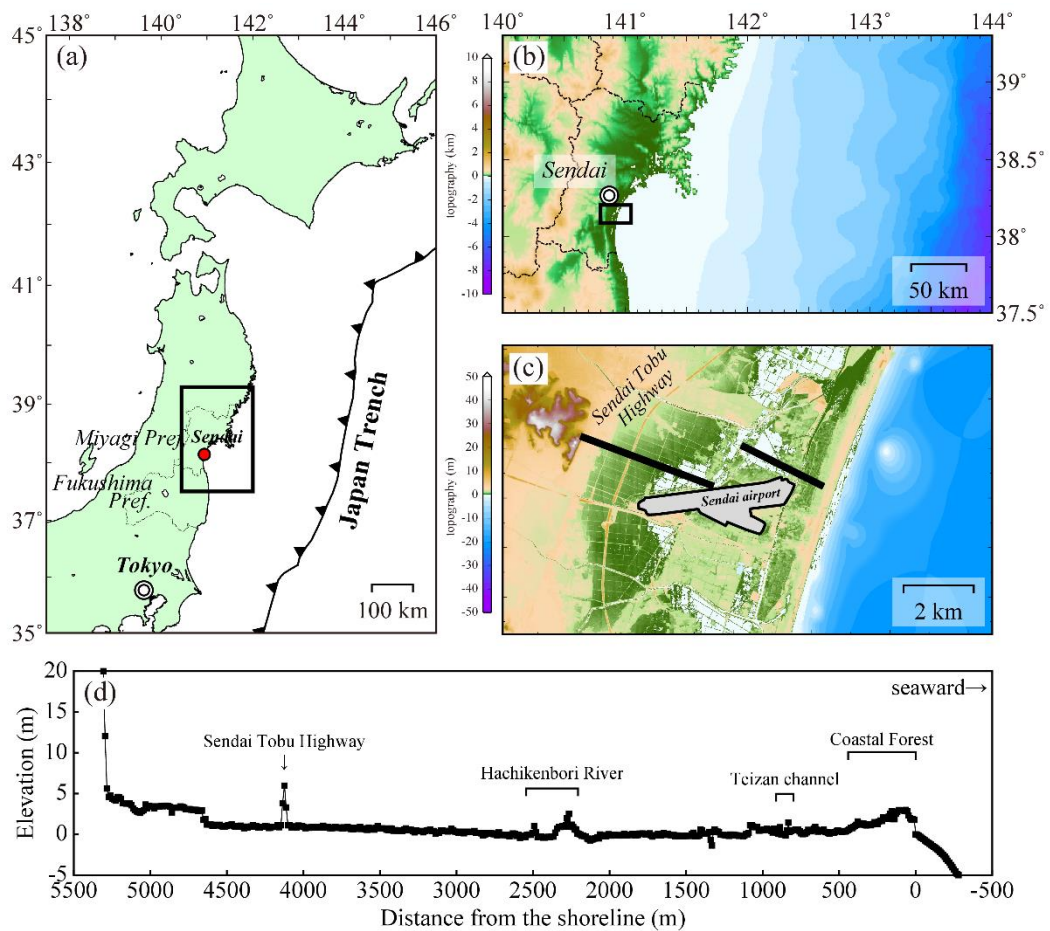


Figure 2-6. Location and topographic profiles of the Sendai plain in Miyagi Prefecture. (a) Overview of northeastern Japan along the Japan Trench. Red dot shows the location of the Sendai plain. (b) Detailed map around the Sendai plain, (c) Topography of the Sendai plain. Solid lines indicate transect for tsunami deposit surveys (e.g., Sawai *et al.*, 2007; 2008; Goto *et al.*, 2011; Richmond *et al.*, 2012; Szczuciński *et al.*, 2012). (d) Topographic profiles along transect.

The plain was formed by rapid shoreline progradation marked by six complex beach ridges (I, I', II, IIIa, IIIb, and IIIc) of 0.8-3.1 m high, which developed around 5000–4500 years BP, 3100-3000 years BP, 2800–1600 years BP, 1300-1100 years BP, 1100 years BP, and 350 years BP, and the present, respectively (Matsumoto, 1984; Ito, 2005). Among them, the youngest beach ridges are covered with pine forests artificially planted since the 1600s (e.g., Goto *et al.*, 2013). The elevation is nearly 0 m or lower behind the youngest beach ridge and increases gradually landward. The Sendai Tobu Highway, the embankment of which is approximately 8 m high, runs north-south at approximately 4.5 km from the shoreline.

The 2011 Tohoku tsunami inundated up to about 5.2 km inland. The observed tsunami flow depth was over 10 m near the coastal dune ridges and decreased landward to less than 3 m close to the inundation limit (Fig. 2-7; Mori *et al.*, 2012).

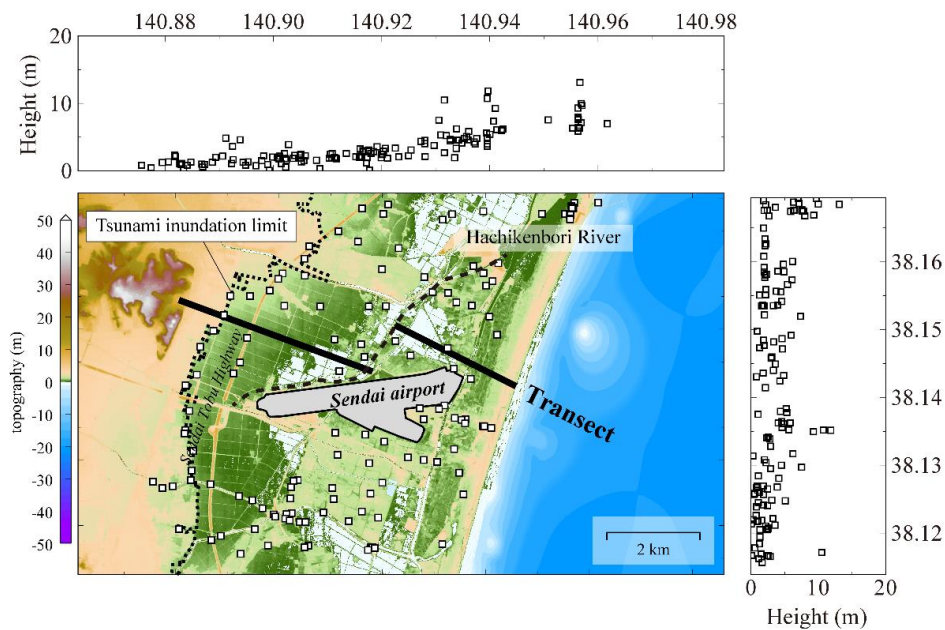


Figure 2-7. The observed 2011 Tohoku tsunami run-up heights and inundation limit on the Sendai plain. The dotted curve shows the inundation limit for the 2011 tsunami. The dashed line indicates the Hachikenbori River.

The tsunami was almost stopped by the Sendai Tobu Highway, although it further inundated the underpasses of the highway in some locations. The tsunami deposits were described and sampled for facies analysis, geochemistry and micropaleontology at more than 120 pits (Goto *et al.*, 2011; Richmond *et al.*, 2012; Szczuciński *et al.*, 2012). They generally became thin inland with a maximum thickness of around 30 cm (Fig. 2-8).

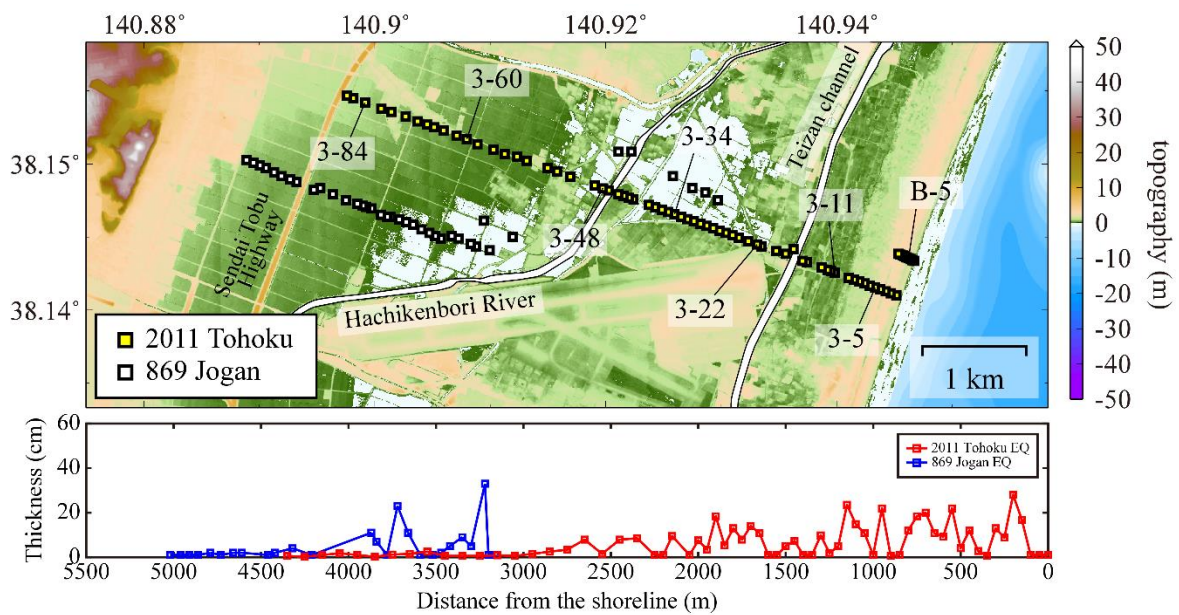


Figure 2-8. Sampling locations and sediment thicknesses for the 2011 and 869 Jogan tsunami deposits along the Sendai airport transect (e.g., Sawai *et al.*, 2007; 2008; Goto *et al.*, 2011; Richmond *et al.*, 2012; Szczuciński *et al.*, 2012). The red and blue lines show the sediment thicknesses for the 2011 Tohoku and 869 Jogan tsunami deposits, respectively.

Up to 1.0 and 1.2 km inland from the shore, the deposit is composed of sand of variable grain size and thickness. The sand is massive, graded or laminated, often with soil rip-up clasts at or near the base. Between 1.2 and 2.8 km inland, the deposit is sand-dominated with mud laminae and rip-up clasts. Further inland (2.8-4.5 km), the deposit is mud-dominated (<3.5 cm in thick) with a thin and patchy sand lamina (one to a few grains thick) at the base and, rarely, within the mud itself (Fig. 2-9). The tsunami deposit with a

thicker than 0.5 cm-thick sand layer extended approximately 2.8 km inland (about 62% of the inundation distance), although the layer was not continuous.

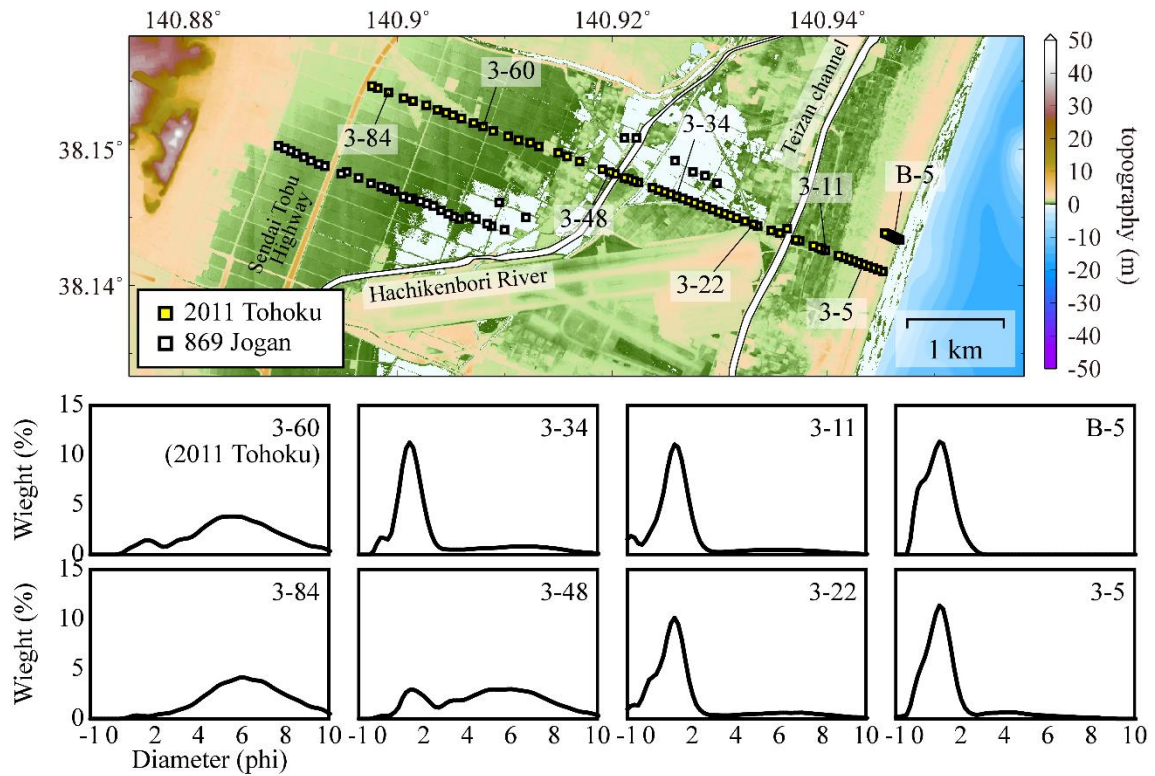


Figure 2-9. Grain size distributions for the 2011 Tohoku tsunami deposits in the Sendai plain (e.g., Jaffe *et al.*, 2012; Szczuciński *et al.*, 2012).

The 869 Jogan tsunami deposits were also identified just below a volcanic ash (AD 915 To-a tephra) in a total of 26 geological core samples collected by Abe *et al.* (1990), Minoura and Nakaya (1991), and Sawai *et al.* (2006; 2007; 2008). They conclude that the tsunami deposits were distributed 3.2-5.0 km distance from the current shoreline, and the coastline in AD 869 was about 1 km inland from the present one. The thickness varies from 1 to 33 cm and becomes thinner landward (Fig. 2-8). Additionally, the grain size also became finer toward inland.

2-5. Numanohama marsh, Iwate Prefecture

The Numanohama marsh is a lowland back marsh surrounded by high and steep cliffs, which is located about 13 km north of Miyako City in Iwate Prefecture (Fig. 2-10). The marsh extends about 1000 m east-west and 250 m north-south and is isolated from the Pacific Ocean by a beach ridge with a height of about 4.5 m. A small narrow river with a presumed water catchment area of approximately 2 km × 1 km streams in the central part of the study site.

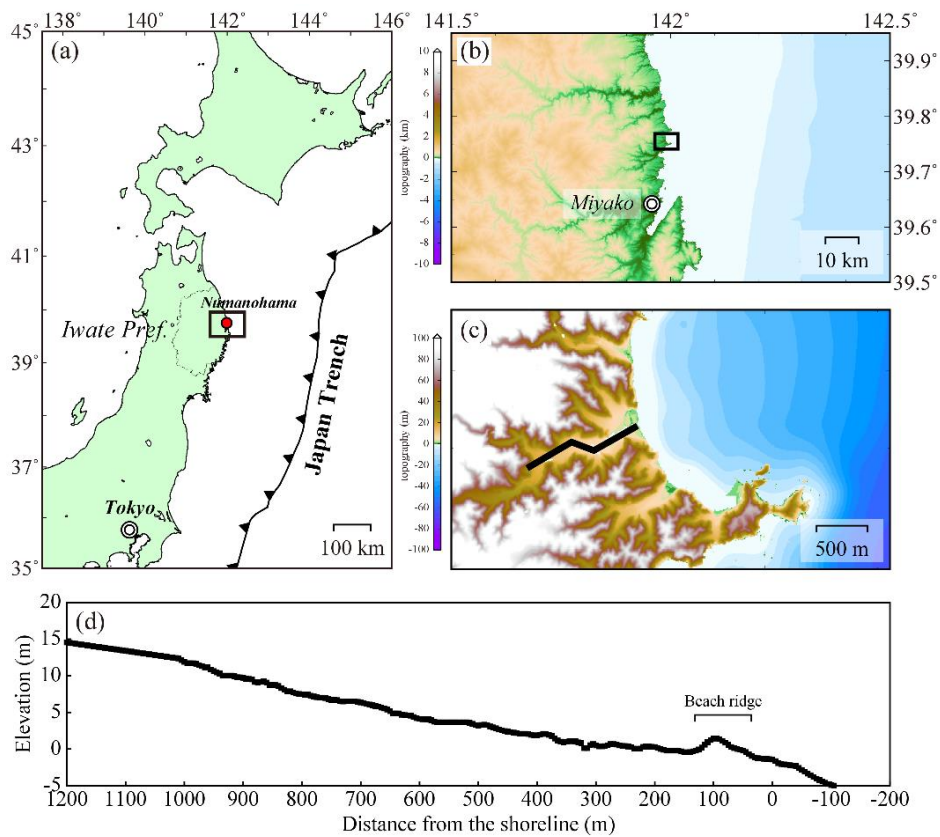


Figure 2-10. Location and topographic profiles of the Numanohama marsh in Iwate Prefecture. (a) Overview of northeastern Japan along the Japan Trench. The red dot shows the location of the Numanohama marsh. (b) Detailed map around the Numanohama marsh, (c) Topography of the Numanohama marsh. The solid line indicates transect for tsunami deposit surveys (Goto *et al.*, 2015; 2017; 2019). (d) Topographic profiles along transect.

The 2011 Tohoku tsunami inundated up to about 1 km inland. The tsunami height was from 16.5 to 30.1 m (Fig. 2-11; Tsuji *et al.*, 2011, 2014). In addition to the 2011 tsunami, several historical tsunamis have also struck according to reports and previous studies. For example, the tsunami heights were about 24.2 m for the 1896 Meiji Sanriku-Oki earthquake (Yamana, 1896; Unohana and Ota, 1988), 7.2 m for the 1933 Syowa Sanriku-Oki earthquake (Earthquake Research Institute, 1934), and 2.2 m for the 1960 Chile earthquake (Committee for Field Investigation of the Chilean Tsunami, 1960-1961), respectively.

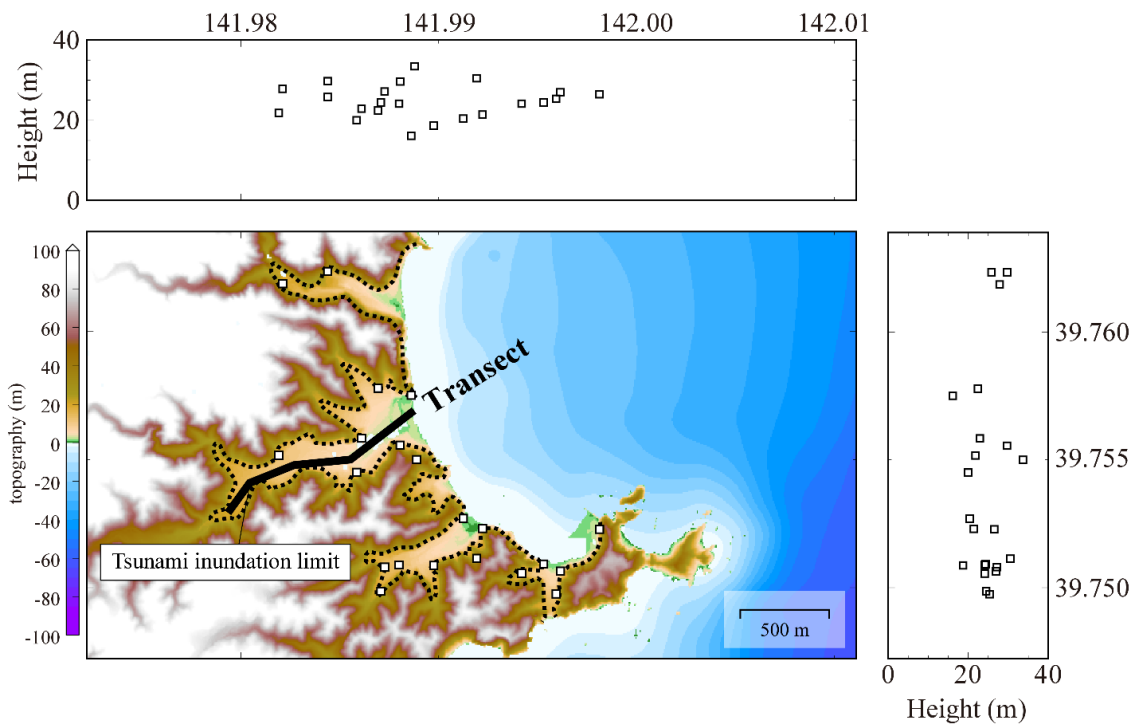


Figure 2-11. The observed 2011 Tohoku tsunami run-up heights and inundation limit in the Numanohama marsh. The dotted curve shows the inundation limit of the 2011 tsunami.

In this marsh, tsunami deposit surveys have already been conducted (Goto *et al.*, 2015; 2017; 2019). According to the results, the 2011 Tohoku tsunami deposits were collected in a total of 20 core samples between 140 and 990 m from the coast. The sediment

thickness varies from 4 to 23 cm (Fig. 2-12). It is composed of medium and coarse sand with angular, sub-angular, and round gravels/pebbles (Fig. 2-13). The 2011 tsunami deposit obtained at sampling location P5, which is the most inland location, contains abundant angular gravels. This P5 site is very close to a slope and river valley, therefore that the gravels were probably introduced by other mechanisms (e.g., the strong motion of the mainshock and aftershock).

The 869 Jogan tsunami deposits are confirmed in six core samples. The thickness is about 15 cm or more (Fig. 2-12). It is composed mainly of medium sand to granules containing round pebbles and very angular gravels (Fig. 2-13).

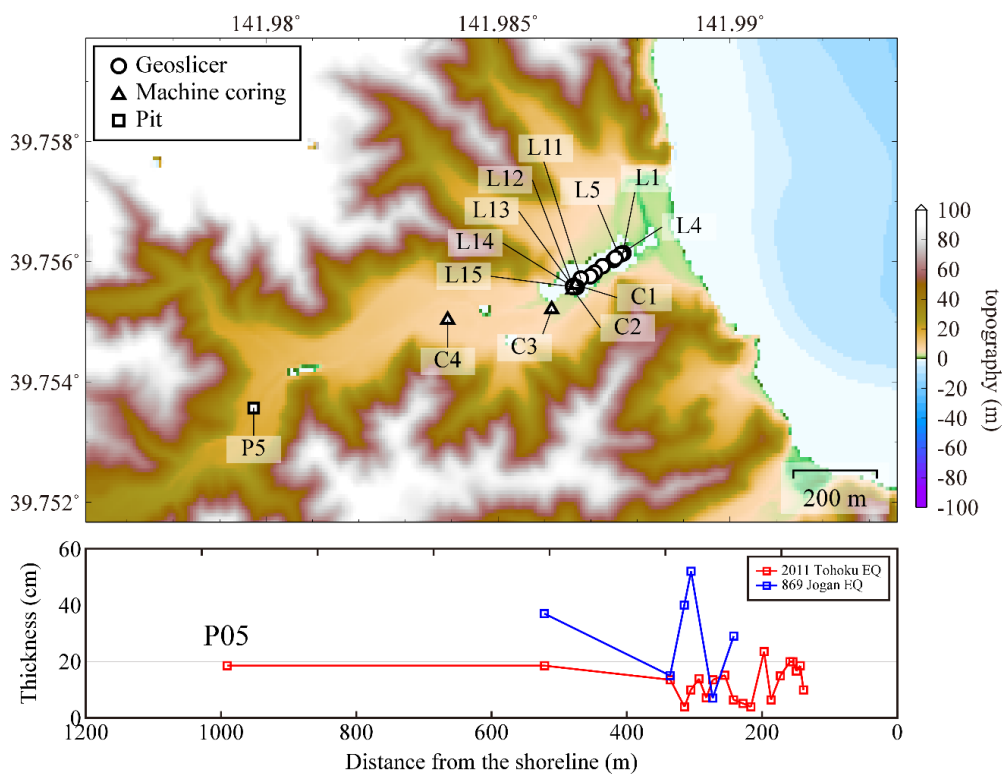


Figure 2-12. Sampling locations and sediment thicknesses for the 2011 Tohoku and 869 Jogan tsunami deposits along the Numanohama marsh transect (Goto *et al.*, 2015; 2017; 2019). The red and blue lines show the sediment thicknesses for the 2011 Tohoku and 869 Jogan tsunami deposits, respectively.

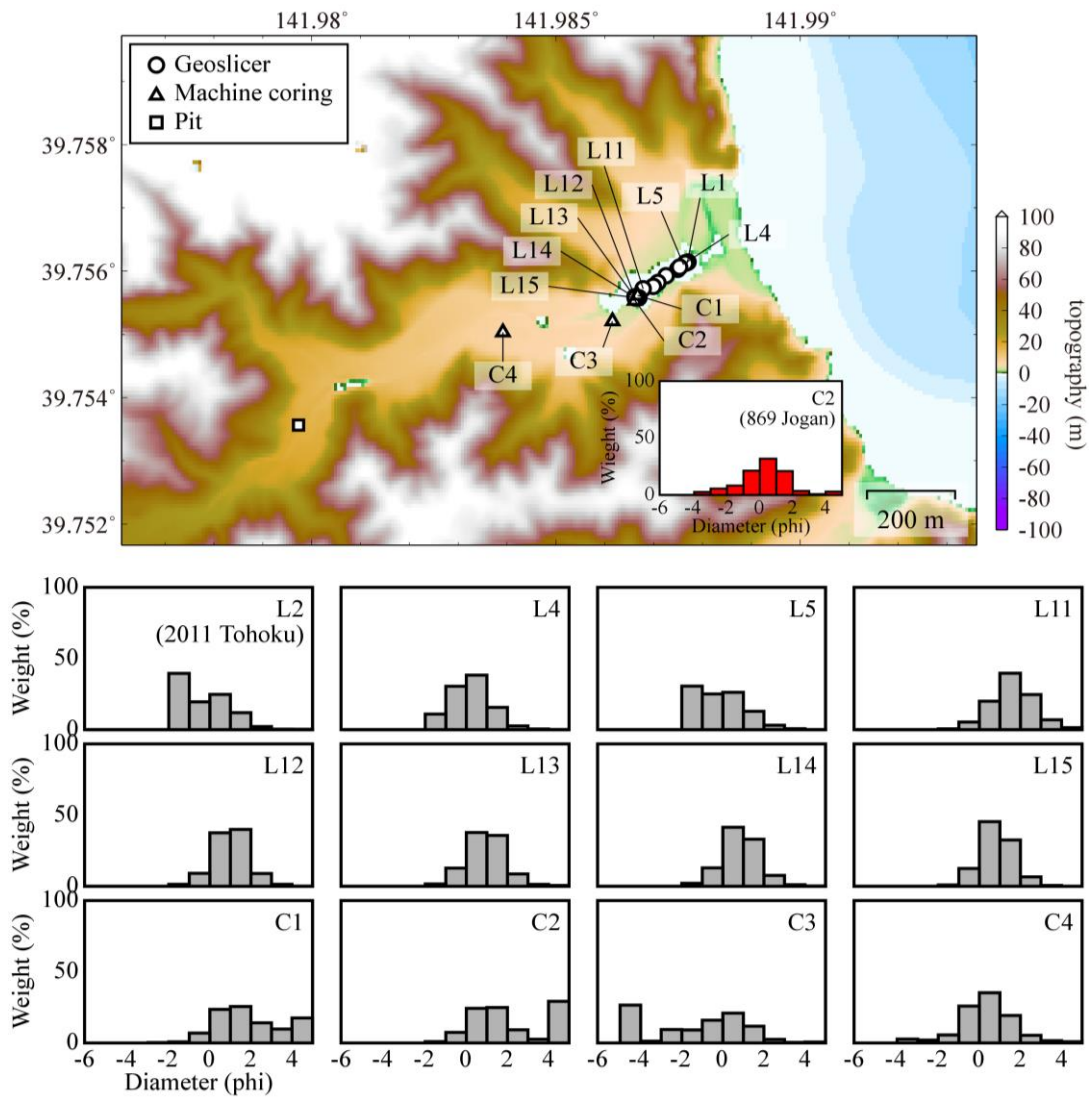


Figure 2-13. Grain size distributions for the 2011 Tohoku and 869 Jogan tsunami deposits in the Numanohama marsh (Goto *et al.*, 2015; 2017; 2019). The gray and red histograms show the grain size distributions for the 2011 Tohoku and 869 Jogan tsunami deposits, respectively

CHAPTER 3. Methods and Data

3-1. Geological Analysis

3-1-1. Field Survey and Geological Core Sampling

To obtain geological core samples in the Idagawa lowland, two transects, A-A' and B-B', were established perpendicular and parallel to the current shoreline, respectively. The elevation along the transects was measured with a Global Navigation Satellite System receiver (ProMark Field 120, Ashtech). A total of 16 cores (A01-A09, B01-B07) were obtained at distances of 600-1900 m from the coast using a Handy Geoslicer with lengths of either 1.5 m or 3.0 m length (Fig. 3-1 and Table 3-1).

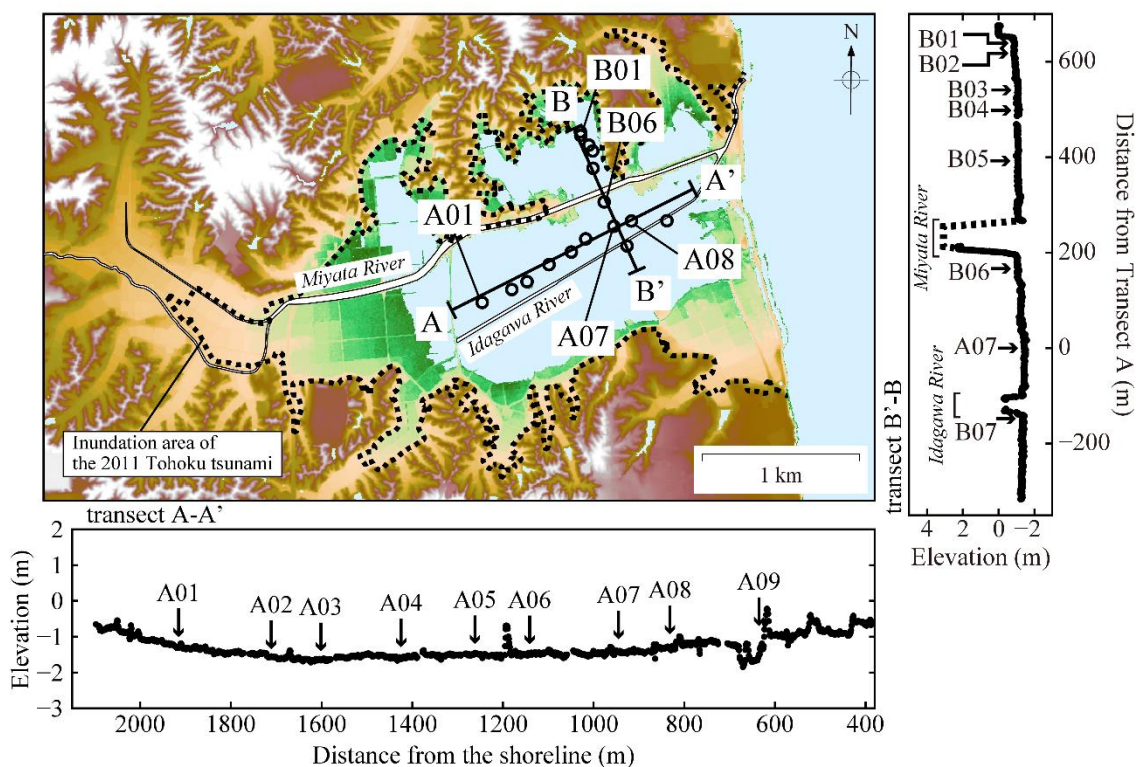


Figure 3-1. Sampling locations and topographic profiles for the Idagawa lowland.

Table 3-1. Sampling locations for the Idagawa lowland.

Core No.	Latitude (deg)	Longitude (deg)	Elevation (m)	Length (m)	Distance from the coast (m)
A01	37.52339167	141.01165830	-1.32	2.35	1916
A02	37.52413611	141.01379444	-1.55	2.41	1711
A03	37.52460000	141.01489440	-1.66	1.66	1601
A04	37.52557777	141.01649444	-1.62	1.27	1425
A05	37.52630278	141.01810280	-1.45	1.66	1262
A06	37.52705833	141.01913333	-1.46	1.18	1141
A07	37.52778611	141.02116390	-1.43	2.14	945
A08	37.52809166	141.02243055	-1.33	2.35	832
A09	37.52810833	141.02499720	-1.51	2.86	635
B01	37.53320555	141.01875277	-0.88	2.15	1584
B02	37.53300833	141.01878330	-0.87	2.66	1563
B03	37.53244553	141.01936845	-1.10	2.02	1486
B04	37.53211752	141.01964610	-1.09	2.47	1443
B05	37.53111111	141.01966940	-1.07	1.70	1338
B06	37.52917773	141.02046253	-1.10	2.58	1112
B07	37.52665327	141.02212895	-1.35	1.82	1093

3-1-2. Sedimentological Analysis

Photographs were firstly taken of each core sample, and then the sedimentary facies, patterns, and structures, such as bedforms, laminae, erosional basal contact, color, and grain size were described. Computed Tomography (CT) scanning was used to examine the three-dimensional sedimentological structures of five cores (A02, A04, A06, A08, and B01). The CT image scanning was performed using a CT scanner (Aquilion PRIME, Toshiba Medical Systems Corporation) at the Kochi Core Center. Grain size analysis was performed on seven representative cores (A01, A02, A07, B02, B03, B06, and B07). Subsamples were taken at about 1 cm vertical intervals from the core sediments. They were immersed in a dispersion solution (aqueous solution of sodium hexametaphosphate) and stirred until the particle density became constant. The grain size was then measured with a laser granulometer (SALD-3000S, Shimadzu Corporation) at the Graduate School

of Frontier Science, the University of Tokyo. The sediment was classified into seven categories (silt, very fine, fine, medium, coarse, very coarse sand, and gravel) according to the Wentworth grain size classification scheme (Wentworth, 1922). Statistical parameters were calculated using the phi scale (Krumbein, 1938; Folk and Ward, 1957).

3-1-3. Nannofossil Analysis

To estimate the sedimentary environment change before and after events, the number of nannofossils (i.e., diatoms, *coccoliths*, *Silicoflagellates*, and *Sponge spicules*) contained in the sediment was detected. The subsamples were collected at 5 or 10 cm vertical intervals from the core A02, and smear slides were prepared for counting. Diatom analysis was performed by the Paleoenvironment Research Institute Co.,Ltd, and nannofossil analysis was performed by Dr. Tomoko Goto (the University of Tokyo).

At least 200 diatoms were identified and counted using a biological microscope with a magnification of 600x to 1500x. The diatom identification was based on Lowe (1974) for environmental requirements and pollution tolerance of diatoms, Kosugi (1986) for terrestrial diatoms, Ando (1986) for fresh-water diatoms, and Kosugi (1988) for brackish-water and marine-water diatoms.

Coccoliths, *Sponge spicules*, and *Silicoflagellates* were counted under a polarizing microscope with a magnification of 400x. The total number of *coccoliths* producing individuals in 10 visual fields for each sample was classified into 15 appearance groups; level 0 (no appearance), level I (1–10 counts), level II (11–20 counts), level III (21–30 counts), level IV (31–40 counts), level V (41–50 counts), level VI (51–100 counts), level VII (101–200 counts), level VIII (201–300 counts), level IX (301–400 counts), level X (401–500 counts), level XI (501–600 counts), level XII (601–700 counts), level XIII (701–800 counts), level XIV (801–900 counts).

3-1-4. Radiocarbon Dating

Organic samples (e.g., seeds, charcoals, plant fragments, wood, and shells) were collected above and below event deposits for radiocarbon dating using Accelerator Mass Spectrometry (AMS) measurements. A total of 33 samples from the cores A01, A05, A07, A09, and B02 were measured; 14 samples by the Institute of Accelerator Analysis Ltd., Japan (IAA), and the other 19 samples by the Laboratory of Radiocarbon Dating at the University Museum, the University of Tokyo (UMUT). Isotope fractionation effects were corrected with $\delta^{13}\text{C}$ values to estimate radiocarbon ages. Corrected radiocarbon (^{14}C) ages were calibrated to calendar ages with the OxCal 4.3 program and the IntCal13 and Marine13 calibration curves (Bronk Ramsey, 2009; Reimer *et al.*, 2013). The uncertainty of the ^{14}C ages was taken to be 2σ , where σ is the standard deviation. For marine or brackish shell samples, it is necessary to correct the global and local marine reservoir effects. The local marine reservoir effect (ΔR) has been reported as 82 ± 33 years in the southern Kanto district closest to the Idagawa lowland (Shishikura *et al.*, 2007) and 393 ± 32 years on the east coast of Hokkaido and Sakhalin (Yoneda *et al.*, 2007). The ΔR value depends on the ocean current; hence it is hard to estimate the values for the Idagawa lowland because the Kuroshio and Oyashio Currents converge off the Sanriku coast. Thus, the local effect was not corrected for brackish shell samples in this study.

3-1-5. Age-Depth Models

Age-depth models were constructed for the cores A01 and B02 based on individual dating data and the Poisson process-deposition model incorporated in the OxCal program (Bronk Ramsey, 2008). The following assumption were also made; (1) the law of superposition is established, (2) the sedimentary rate is always positive, (3) the depositional ages of event deposits are the same for both cores, and (4) the arrival times

of the increments $N = k(d_{i+1} - d_i)$ occurring at an arbitrary depth (from d_i to d_{i+1}) form a Poisson process. Here, k is the Poisson parameter which is the increment per unit length and depends on grain size. The value of k is likely to be around 1 cm^{-1} if a coarse sediment with gravels is considered, whereas a fine sediment might have a value of up to 10 cm^{-1} (Bronk Ramsey, 2008). To estimate an appropriate k value from direct measurement, Bronk Ramsey (2008) proposed that it was determined from the distance between stratigraphic marker layers. In this study, event deposits were used as the marker layers (Table 3-2).

Table 3-2. Distances between stratigraphic marker layers (units are cm).

Core No.	EV1-EV2	EV2-EV3	EV3-EV4	EV4-EV5	EV5-EV6	EV6-EV7
A01	36	26	6	50	12	-
A02	37	42	19	67	-	-
A03	44	28	4	28	2	-
A04	33	35	3	-	-	-
A05	40	36	14	30	-	-
A06	13	50	4	-	-	-
A07	21	37	2	44	4	-
A08	10	48	14	22	18	-
B01	29	8	0	44	15	48
B02	21	25	9	31	9	34
B03	42	6	4	5	4	50
B04	26	23	0	39	9	48
B05	26	39	0	24	15	29
B06	22	17	4	42	7	-
B07	8	20	7	8	17	-

By measuring the distance (u , v , w , x , and z) between event deposits in multiple cores, the ratios (U , V , W , X , and Z) of the distance and total thickness excepting event deposits were firstly calculated from the distances at each core i ;

$$U_i = \frac{u_i}{(u_i + v_i + w_i + x_i + z_i)}$$

$$V_i = \frac{v_i}{(u_i + v_i + w_i + x_i + z_i)}$$

$$W_i = \frac{w_i}{(u_i + v_i + w_i + x_i + z_i)}$$

$$X_i = \frac{x_i}{(u_i + v_i + w_i + x_i + z_i)}$$

$$Z_i = \frac{z_i}{(u_i + v_i + w_i + x_i + z_i)}$$

Next, the following relations hold between increment N and mean ($\mu_U, \mu_V, \mu_W, \mu_X$, and μ_Z), standard deviation ($\sigma_U, \sigma_V, \sigma_W, \sigma_X$, and σ_Z);

$$\sigma_U \sigma_V \sigma_W \sigma_X \sigma_Z \approx \mu_U \mu_V \mu_W \mu_X \mu_Z \frac{1}{N}$$

$$N \approx \frac{\mu_U \mu_V \mu_W \mu_X \mu_Z}{\sigma_U \sigma_V \sigma_W \sigma_X \sigma_Z}$$

Substituting into $N = k(d_{i+1} - d_i)$, an estimate for the best Poisson parameter for each core i can be found;

$$k_i = \frac{\mu_U \mu_V \mu_W \mu_X \mu_Z}{\sigma_U \sigma_V \sigma_W \sigma_X \sigma_Z} \frac{1}{(u_i + v_i + w_i + x_i + z_i)}$$

The calculated values of k ranged from 9 to 26 cm^{-1} (Table 3-3).

Table 3-3. Poisson parameter for each core.

Core No.	U_i	V_i	W_i	X_i	Y_i	Z_i	k_i
A01	0.28	0.20	0.05	0.38	0.09	-	12
A02	0.22	0.25	0.12	0.41	-	-	9
A03	0.42	0.26	0.04	0.26	0.02	-	15
A04	0.46	0.49	0.04	-	-	-	22
A05	0.33	0.30	0.12	0.25	-	-	13
A06	0.19	0.75	0.06	-	-	-	23
A07	0.19	0.34	0.02	0.41	0.04	-	14
A08	0.09	0.43	0.13	0.20	0.16	-	14
B01	0.20	0.06	0.00	0.31	0.10	0.33	11
B02	0.16	0.19	0.07	0.24	0.07	0.26	12
B03	0.38	0.05	0.04	0.05	0.04	0.45	14
B04	0.18	0.16	0.00	0.27	0.06	0.33	11
B05	0.20	0.29	0.00	0.18	0.11	0.22	12
B06	0.24	0.18	0.04	0.46	0.08	-	17
B07	0.13	0.33	0.12	0.13	0.28	-	26
aver.	0.26	0.29	0.07	0.28	0.10	0.35	18
stdev.	0.11	0.18	0.05	0.12	0.08	0.09	-

Additionally, in order to evaluate the variances of depositional ages and recurrence intervals with the values of k , the age-depth models constrained from different values ($k=5, 10, 15, 20, 40, 60, 80, \text{ and } 100 \text{ cm}^{-1}$) are compared. The models were constrained for only terrestrial samples because no corrections for the reservoir effect of marine and brackish samples were conducted. The Event Free Depth (EFD) scale was applied after excluding the thickness of event deposits from the total depth (Table 3-4), because the sedimentation rates of sand and silt were significantly different (Bronk Ramsey *et al.*, 2012). The depositional ages and recurrence intervals were calculated from the constructed models.

Table 3-4. Event-Free Depth scale for the cores A01 and B02.

core A01				core B02			
From [cm]	To [cm]	EFD [cm]	Seismite	From [cm]	To [cm]	EFD [cm]	Seismite
0	6	d	-	0	5	d	-
6	24	6	EV1	5	19	5	EV1
24	60	d-18	-	19	40	d-14	-
60	78	42	EV2	40	45	26	EV2
78	104	d-36	-	45	70	d-19	-
104	116	68	EV3	70	82	51	EV3
116	122	d-48	-	82	91	d-31	-
122	125	74	EV4	91	92	60	EV4
125	175	d-51	-	92	123	d-32	-
175	205	124	EV5	123	146	91	EV5
205	217	d-81	-	146	155	d-55	-
217	235	136	EV6	155	169	100	EV6
				169	203	d-69	-
				203	209	134	EV7
				209	252	d-75	-

3-2. Numerical Model of Tsunami Sediment Transport

3-2-1. Tsunami Hydrodynamics

Tsunami propagation and inundation are expressed by non-linear shallow water theory, which consists of the equations of the conservation of mass and momentum using the Finite Difference Method (FDM) in the Cartesian coordinate system (e.g., Satake, 1995; Baba *et al.*, 2015). The two-dimensional equations are as follows;

$$\frac{\partial h}{\partial t} + \frac{\partial M}{\partial x} + \frac{\partial N}{\partial y} = 0 \quad (1)$$

$$\frac{\partial M}{\partial t} + \frac{\partial}{\partial x} \left(\frac{M^2}{D} \right) + \frac{\partial}{\partial y} \left(\frac{MN}{D} \right) + gD \frac{\partial h}{\partial x} + \frac{gn^2}{D^3} M \sqrt{M^2 + N^2} = 0 \quad (2)$$

$$\frac{\partial N}{\partial t} + \frac{\partial}{\partial x} \left(\frac{MN}{D} \right) + \frac{\partial}{\partial y} \left(\frac{N^2}{D} \right) + gD \frac{\partial h}{\partial y} + \frac{gn^2}{D^3} N \sqrt{M^2 + N^2} = 0 \quad (3)$$

where t is time, h is water level, D is total water depth ($D=h+d$), M and N are discharge fluxes along the x - and y -axes, g is gravitational acceleration ($=9.8 \text{ m/s}^2$), and n is Manning's roughness coefficient ($=0.025 \text{ m}^{-1/3}/\text{s}$). In this study, the two-dimensional numerical simulation is adopted for tsunami propagation and inundation.

3-2-2. Sediment Transport

The movement of sand by water flow can be classified as either bedload or suspension movement. The bedload represents a movement type in which the sediment is transported by sliding, rolling and saltation, and the suspension refers to a movement in which the sediment is held in the water and carried with the flow. The regions where the sand is carried by the bedload and suspension are generally called the bedload layer and suspended load layers, respectively. For the numerical modeling of tsunami sediment transport, it is conceptually separated from the suspended load and bedload layers (Fig. 3-2; e.g., Takahashi *et al.*, 1999; 2000; Gusman *et al.*, 2012; Sugawara *et al.*, 2014a; 2014b). The one-dimensional sediment transport simulation is basically carried out for the sediment transport modeling.

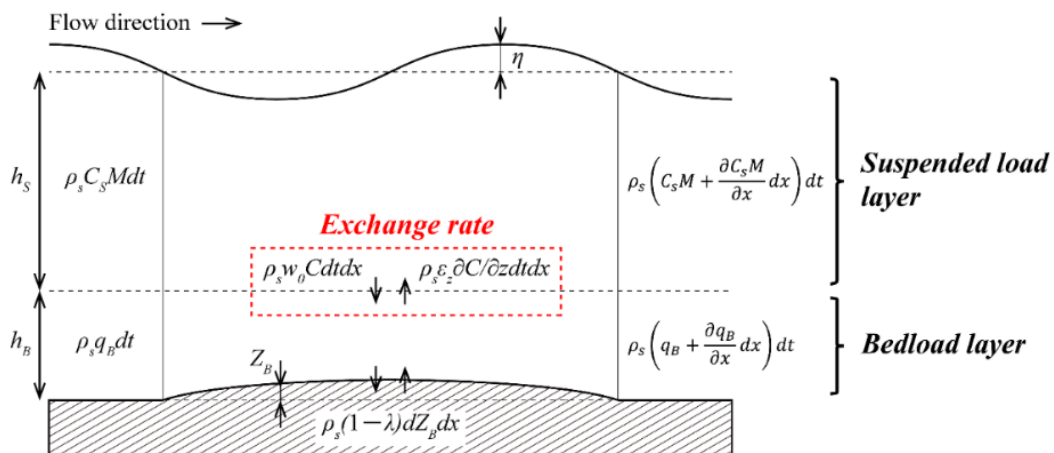


Figure 3-2. Diagram of sediment transport modeling due to tsunami.

3-2-2-1. Continuity Equation in the Bedload Layer

First, the mass conservation in the bedload layer is considered. In this layer, the following four terms (i to iv) are balanced for the incoming and outgoing sand;

(i) The exchange rate between the bedload layer and the bed

$$\rho_s(1 - \lambda)\delta Z_B \delta x$$

where ρ_s is the density of sand particles, λ is the porosity, and Z_B is the bed level change. The difference between the simulated pre- and post-tsunami elevations is the apparent erosion and deposition for erodible beds. The net erosion and net deposition can be calculated from the difference between the initial elevation and the lowest elevation and the difference between the final elevation and the lowest elevation, respectively (Li *et al.*, 2012).

(ii) The sediment moved in the downward direction in the bedload layer

$$\rho_s \left(q_B + \frac{\partial q_B}{\partial x} \delta x \right) \delta t - \rho_s q_B \delta t = \rho_s \frac{\partial q_B}{\partial x} \delta x \delta t$$

where q_B is the bedload rate. As described by Watanabe *et al.* (1984) and Tanaka *et al.*, (1989), the bedload rate affects the bed slope in bedload transport and can be written as;

$$Q_B = q_B - |q_B| \varepsilon_z \frac{\partial Z_B}{\partial x}$$

where Q_B is the bedload rate with the effect of bed slope. The vertical diffusion coefficient for the sediment (ε_z) is assumed to be 2.0. This formula indicates that the bedload rate is higher if the flow is moving down, and smaller if the flow is climbing up the slope.

(iii) The sediment of rising-up to the suspension due to diffusion

$$\rho_s \varepsilon_z \frac{\partial \bar{C}}{\partial z} \delta x \delta t$$

where \bar{C} is the mean concentration of sediment in the suspended load layer.

(iv) The sediment settling down from the suspended load layer

$$\rho_s \omega_0 \bar{C} \delta x \delta t$$

where ω_0 is the settling velocity of sand particles.

Summarizing the above terms, the equation of mass conservation for the bedload layer is given as follows;

$$\frac{\partial Z_B}{\partial t} + \frac{1}{1-\lambda} \left(\frac{\partial Q_B}{\partial x} + W_{ex} \right) = 0 \quad (4)$$

where,

$$W_{ex} = \varepsilon_z \frac{\partial \bar{C}}{\partial z} - w_0 \bar{C} = q_{rise} - \omega_0 \bar{C}$$

Here, W_{ex} is the exchange rate, which is a balance between sediment settling from the suspended load layer and the sediment rising-up to the suspension and the pick-up rate (q_{rise}).

3-2-2-2. Continuity Equation in the Suspended Load Layer

Next, the mass conservation in the suspended load layer is considered. In this layer, the following four terms (v to viii) are balanced;

(v) The sediment moved downward direction in the suspended load layer

$$\rho_s \left(\bar{C} M + \frac{\partial \bar{C} M}{\partial x} \delta x \right) \delta t - \rho_s \bar{C} M \delta t = \rho_s \frac{\partial \bar{C} M}{\partial x} \delta x \delta t$$

The mean concentration of sediment in the suspended load layer is limited to 1% for each grain size (Takahashi *et al.*, 1999; Gusman *et al.*, 2018).

(vi) The sediment of rising-up to the suspension caused by diffusion

$$\rho_s \varepsilon_z \frac{\partial \bar{C}}{\partial z} \delta x \delta t$$

(vii) The sediment settling down from the suspended load layer

$$\rho_s w_0 \bar{C} \delta x \delta t$$

(viii) Total balance of sediment in the suspended load

$$\rho_s \frac{\partial \bar{C} D}{\partial t} \delta x \delta t$$

Summarizing the above terms, the equation of mass conservation for the suspended load layer is expressed as the following;

$$\frac{\partial \bar{C} D}{\partial t} + \frac{\partial \bar{C} M}{\partial x} - W_{ex} = 0 \quad (5)$$

The discharge fluxes (M) and total depth (D) are calculated from the numerical simulation. The bedload and exchange rates are also determined from tsunami hydraulic experiments (Takahashi *et al.*, 1999; Takahashi *et al.*, 2011).

3-2-3. Pick-up Rate

The pick-up rate (q_{rise}) from the hydraulic experiment results is expressed by

$$q_{rise} = w_\alpha \sqrt{sgd} \tau_*^2$$

where w_α is a coefficient for pick-up rate as a function of grain size, s is the submerged specific gravity of sand (=1.65), and d is mean diameter of sand particles. The Shields parameter (τ_*) is defined as $\tau_* = u_*^2 / sgd$, in which u_* is the shear velocity calculated by the Manning formula ($u_*^2 = gn^2 M |M| / D^{7/3}$). The non-dimensional pick-up function ($\psi_{rise} = w_\alpha \tau_*^2$) was determined from tsunami hydraulic experiments by Takahashi *et al.* (2011). The coefficients (w_α) with three grain sizes (0.166, 0.267, and 0.394 mm) are expressed by

$$w_{\alpha} = \begin{cases} 7.0 \times 10^{-5} & (d = 0.166 \text{ mm}) \\ 4.4 \times 10^{-5} & (d = 0.267 \text{ mm}) \\ 1.6 \times 10^{-5} & (d = 0.394 \text{ mm}) \end{cases}$$

To simulate the sediment transport for various grain sizes, the following equation interpolated/extrapolated from hydraulic experiment results is used (Fig. 3-3 and Tables 3-5, 3-6, and 3-7; Gusman *et al.*, 2018).

$$w_{\alpha} = 19.193 \times 10^{-5} \times \exp(-6.058d) \quad (6)$$

3-2-4. Bedload Rate

The bedload rate (q_B) is experimentally expressed by

$$q_B = w_{\beta} \sqrt{sgd^3} \tau_*^{\frac{3}{2}}$$

where w_{β} is a coefficient for the bedload rate as a function of grain size. The dimensionless bedload rate ($\psi_{bed} = w_{\beta} \tau_*^{\frac{3}{2}}$) was also determined from tsunami hydraulic experiments by Takahashi *et al.* (2011). The coefficients (w_{β}) with three grain sizes (0.166, 0.267, and 0.394 mm) are expressed by

$$w_{\beta} = \begin{cases} 5.6 & (d = 0.166 \text{ mm}) \\ 4.0 & (d = 0.267 \text{ mm}) \\ 2.6 & (d = 0.394 \text{ mm}) \end{cases}$$

As with the coefficient of pick-up rates, the following equation interpolated/extrapolated from hydraulic experiments is used (Fig. 3-3 and Tables 3-5, 3-6, and 3-7; Gusman *et al.*, 2018).

$$w_{\beta} = 9.8044 \times \exp(-3.366d) \quad (7)$$

3-2-5. Settling Velocity

The sand particles have a different settling velocity (ω_0) for each grain size (Rubey, 1933; Ponce, 1989). The settling velocity in oscillating water is given as follows;

$$\omega_0 = \sqrt{\frac{4gd\rho_s - \rho}{3C_D\rho}} \quad (8)$$

where ρ_s is the sediment density, ρ is the water density, and C_D is the drag coefficient. Morrison (2013) reported a relationship between the drag coefficient and Reynolds number (Re) that was derived from experimental results,

$$C_D = \frac{24}{Re} + \frac{26\frac{Re}{5}}{1 + \left(\frac{Re}{5}\right)^{1.52}} + \frac{0.411\left(\frac{Re}{263000}\right)^{-7.94}}{1 + \left(\frac{Re}{263000}\right)^{-8.00}} + \frac{Re^{0.8}}{461000}$$

where

$$Re = \frac{\omega_0 d}{\nu}$$

In the above equation, ν is the kinematic viscosity ($0.8296 \times 10^{-6} \text{ m}^2/\text{s}$). The calculation of the settling velocity for each grain size was done by iterating these equations until the values of ω_0 and C_D converged (Fig. 3-3 and Tables 3-5, 3-6, and 3-7).

3-2-6. Critical Shear Velocity

The critical shear velocity (τ_{cr}), which is the flow velocity required for the sand particles to start moving, also differs for each grain size (Fig. 3-3 and Tables 3-5, 3-6, and 3-7). Shields (1936) formulated a dimensionless parameter that is equal to the ratio of the critical shear stress to the gravitational weight of the grain. As a criterion for incipient motion, the following critical dimensionless parameter is used as the Shield parameter from Soulsby and Whitehouse (1997);

$$\tau_{cr} = \frac{0.3}{1 + 1.2D_*} + 0.055[1 - \exp(-0.02D_*)] \quad (9)$$

where the dimensionless grain size (D_*) is expressed by

$$D_* = \left[\frac{g \left(\frac{\rho_s}{\rho} - 1 \right)}{v^2} \right]^{\frac{1}{3}} d$$

Both the pick-up and bedload rates are zero when the simulated Shields parameter is smaller than the critical Shields parameter.

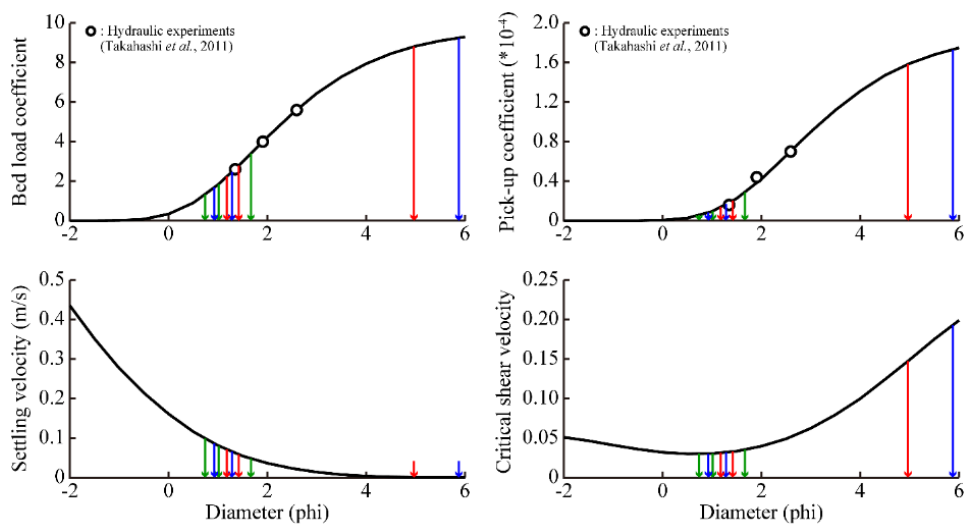


Figure 3-3. Model parameters (Pick-up coefficient, Bedload rate coefficient, settling velocity, and critical shear velocity) for different grain size. The red, blue, and green arrows show grain sizes of the 2011 tsunami deposits at the Idagawa lowland, Sendai plain, and Numanohama marsh, respectively.

Table 3-5. Model parameters for the 2011 Tohoku tsunami deposits for a single grain size.

Study sites	diameter (mm)	Pick-up rate	Bedload rate	Settling velocity	Critical shear velocity
Idagawa	0.408	1.62E-05	2.48	6.461E-02	3.187E-02
Sendai	0.455	1.22E-05	2.13	7.307E-02	3.096E-02
Numanohama	0.582	5.65E-06	1.39	9.538E-02	2.992E-02

Table 3-6. Model parameters for the 2011 Tohoku tsunami deposits for multiple grain sizes.

Study sites	diameter (mm)	Pick-up rate	Bedload rate	Settling velocity	Critical shear velocity
Idagawa	0.032	1.58E-04	8.84	9.868E-04	1.475E-01
	0.374	1.99E-05	2.80	5.846E-02	3.280E-02
	0.442	1.32E-05	2.22	7.074E-02	3.118E-02
Sendai	0.017	1.73E-04	9.295	2.805E-04	1.930E-01
	0.412	1.58E-05	2.460	6.534E-02	3.178E-02
	0.526	7.92E-06	1.675	8.571E-02	3.018E-02
Numanohama	0.316	2.84E-05	3.395	4.798E-02	3.515E-02
	0.496	9.53E-06	1.854	8.038E-02	3.044E-02
	0.600	5.05E-06	1.304	9.845E-02	2.989E-02
	3.922	9.24E-15	1.86E-05	4.300E-01	5.085E-02

Table 3-7. Model parameters for the 869 Jogan tsunami deposits for multiple grain sizes.

Study sites	diameter (mm)	Pick-up rate	Bedload rate	Settling velocity	Critical shear velocity
Idagawa	0.053	1.42E-04	9.57	2.703E-03	1.112E-01
	0.341	2.63E-05	3.12	5.249E-02	3.400E-02
	0.359	2.31E-05	2.94	5.574E-02	3.331E-02
Sendai	0.017	1.73E-04	9.295	2.805E-04	1.930E-01
	0.412	1.58E-05	2.460	6.534E-02	3.178E-02
	0.526	7.92E-06	1.675	8.571E-02	3.018E-02

3-2-7. Approach for Multiple-sized Sand Particles

The above method assumes a single grain size (Gaussian distribution with an arbitrary median diameter), and hence additional theory is necessary if it is to be applied to tsunami deposits composed of grains with multiple sizes. In this study, the multiple grain sizes in actual tsunami deposits are first represented as the sum of several Gaussian distributions (Fig. 3-4). The number of Gaussian distribution (N) is determined by a minimum value when the residual between the observation and the sum of Gaussian distributions is closest to zero. Furthermore, if the interference between different sand particles could be ignored,

the complex problem of multiple grain sizes can be considered as the monotonic problem of a single grain size which corresponds to mean values of each Gaussian distribution.

This approach is applied to actual tsunami deposits. For the 2011 Tohoku tsunami deposits, the smallest N value is 3 at the Idagawa lowland and Sendai plain, and 4 at the Numanohama marsh (Table 3-6). The coarsest single grain size for the Numanohama marsh is 3.922 mm, which is presumed to be gravels supplied from a riverbed or a slope. The sediment with a particle size of 3.922 mm is not considered in this study because such gravels might be transported by an event other than a tsunami. For the 869 Jogan tsunami deposits, the values of N are 3 at all study sites (Table 3-7).

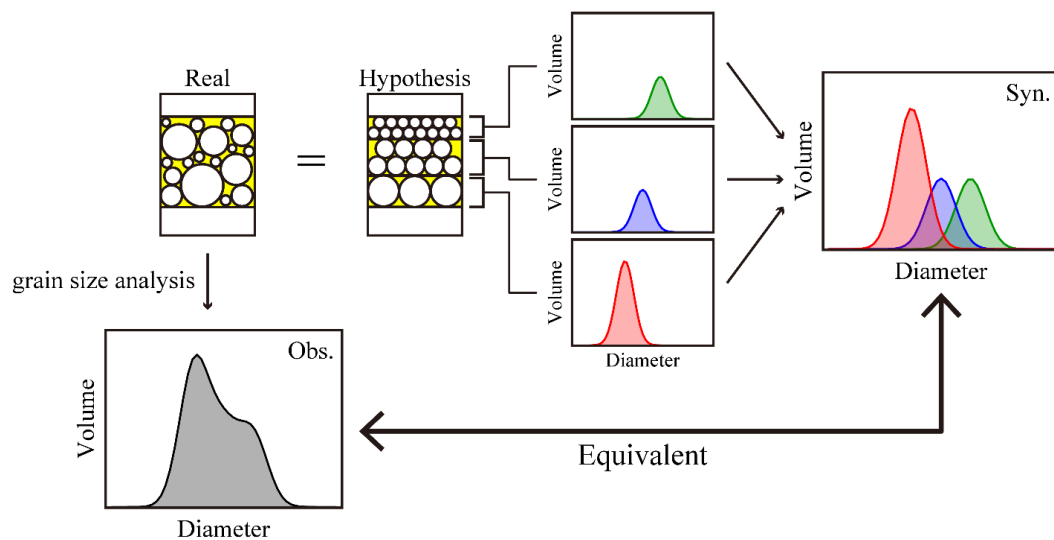


Figure 3-4. Approach for sediment transport modeling of multiple grain sizes.

3-3. Bathymetry and Topography

Different resolution bathymetric and topographic data are used for calculating tsunami propagation, inundation, and sediment transport. A nesting grid of five computational domains covers the offshore areas with lower resolution grids (135 and 405 m in grid intervals) and the nearshore areas with higher resolution grids (5, 15, and 45 m in grid intervals). For the Pacific Ocean, 135 and 405 m interval grids are resampled from the

General Bathymetry Chart of the Oceans (GEBCO) provided by the British Oceanographic Data Centre (BODC). For the nearshore, 5, 15, and 45 m interval grids resampled from digital bathymetry charts (M7000 series) provided by the Marine Information Research Institute (MIRC) and the Digital Elevation Model (DEM) provided by the Geospatial Information Authority of Japan (GSI) are used. In the Idagawa lowland and Sendai plain, topographic data with and without the coastal pine forest is used for sediment transport modeling. The offshore boundary of the computation domain of sediment transport modeling is set at a water depth of 500 m. The results with varying water depth at the offshore boundary are shown in chapter 5-5.

3-4. Coastal Forest

Since coastal forest can reduce flow speed and wave height when a tsunami passes through it (e.g., Shuto, 1985; Harada *et al.*, 2000; Harada and Imamura, 2003a; 2003b; Harada and Kawata, 2004; 2005; Imai *et al.*, 2013; Hayashi *et al.*, 2014), the sediment transport is strongly influenced by such forest because the amount of sand in the suspended load layer depends on the tsunami flow speed. In this study, in order to reproduce tsunami reduction due to a coastal forest, poles with a height of 10 m were placed in grid patterns along the coastline (Fig. 3-5). These poles are set to unmovable and non-destructive. The two-dimensional sediment transport modeling is used for calculations using the topographic data with a coastal forest.

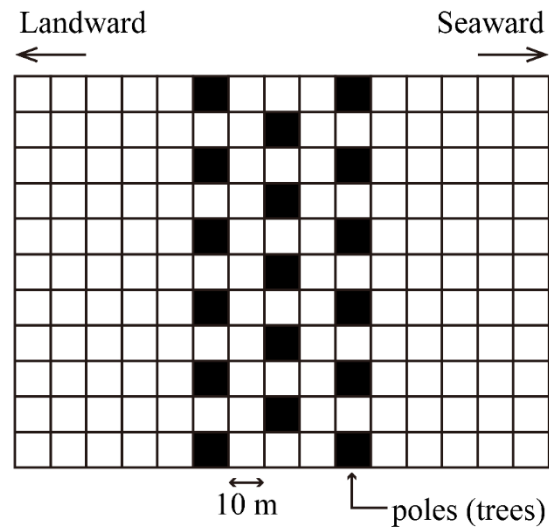


Figure 3-5. Diagram of the simulated coastal forest.

3-5. Initial Parameters and Boundary Conditions

A computational time step of 0.1 sec was used to satisfy the computational stability for the FDM in the finest grid, and the simulation time was 12 hours after the earthquake. Boundary conditions for tsunami run-up computation were determined from a judgment of a cell being wet or dry. Discharge fluxes across the boundary between two grids were calculated if the ground height in the dry cell was lower than the water level in the submerged; otherwise, the discharge fluxes were considered to be zero. The sediment supply beneath the seafloor and at the beach was not limited, whereas the dikes, levees, roads, and coastal protections were set as the non-erosional surface.

3-6. Tsunami Source Models

In order to assess the validity, sensitivity, and accuracy of the sediment transport modeling, 11 scenarios (Models 1-11) from the 55-subfaults model of the 2011 tsunami estimated from tsunami waveform inversion (Satake *et al.*, 2013) by using the 2011 Tohoku tsunami deposit were considered (Fig. 3-6 and Table 3-8). Models 1 to 11 were

all variable-slip models. Rupture propagation was considered only Models 1 and 7, and the rupture was considered to be instantaneous for the other models. In Models 3, 4, and 5, the slip amounts of the subfaults in Model 2 were multiplied by 0.5, 1.5, and 2.0, respectively. The slip distributions for Models 6 and 7 were interchanged with the north and south of the slip distributions of Models 1 and 2, respectively. Models 8 and 9 were ruptures in the only deep/shallow part of the plate interface in Model 2. Models 10 and 11 were also ruptures of only the north/south sides of all subfaults in Model 2.

Next, assuming that the 869 Jogan earthquake ruptured a part or all subfaults of the 2011 Tohoku earthquake, a total of 13 scenarios including the 11 models above plus the previously estimated two models for the 869 Jogan tsunami (Models 12 and 13) inferred from the distribution of historical tsunami deposits in the Sendai plain were considered (Fig. 3-6 and Table 3-8; Namegaya *et al.*, 2010; Namegaya and Satake, 2014). Models 12 and 13 were uniform-slip models with depths of 15 and 31 km. The statistical seafloor displacement was calculated using a rectangular fault model assuming an elastic half-space (Okada, 1985). The effects of horizontal displacement in regions of a steep bathymetric slope were also considered (Tanioka and Satake, 1996b).

Table 3-8. Tsunami source models examined in this study

Models	Mw	Name	Slip distribution	Fault rupture	Reference
1	9.0	55subf_multirup	variable	delayed slip	Satake <i>et al.</i> (2013)
2	9.0	55subf	variable	instantaneous	Satake <i>et al.</i> (2013)
3	8.8	slipx0.5	variable	instantaneous	Satake <i>et al.</i> (2013)
4	9.0	slipx1.5	variable	instantaneous	Satake <i>et al.</i> (2013)
5	9.1	slipx2.0	variable	instantaneous	Satake <i>et al.</i> (2013)
6	9.0	opposite	variable	instantaneous	Satake <i>et al.</i> (2013)
7	9.0	opposite_multirup	variable	delayed slip	Satake <i>et al.</i> (2013)
8	8.8	deep	variable	instantaneous	Satake <i>et al.</i> (2013)
9	8.8	shallow	variable	instantaneous	Satake <i>et al.</i> (2013)
10	8.9	north	variable	instantaneous	Satake <i>et al.</i> (2013)
11	8.8	south	variable	instantaneous	Satake <i>et al.</i> (2013)
12	8.4	869Jogan-Model10	uniform	instantaneous	Namegaya <i>et al.</i> (2010)
13	8.4	869Jogan-Model11	uniform	instantaneous	Namegaya <i>et al.</i> (2010)

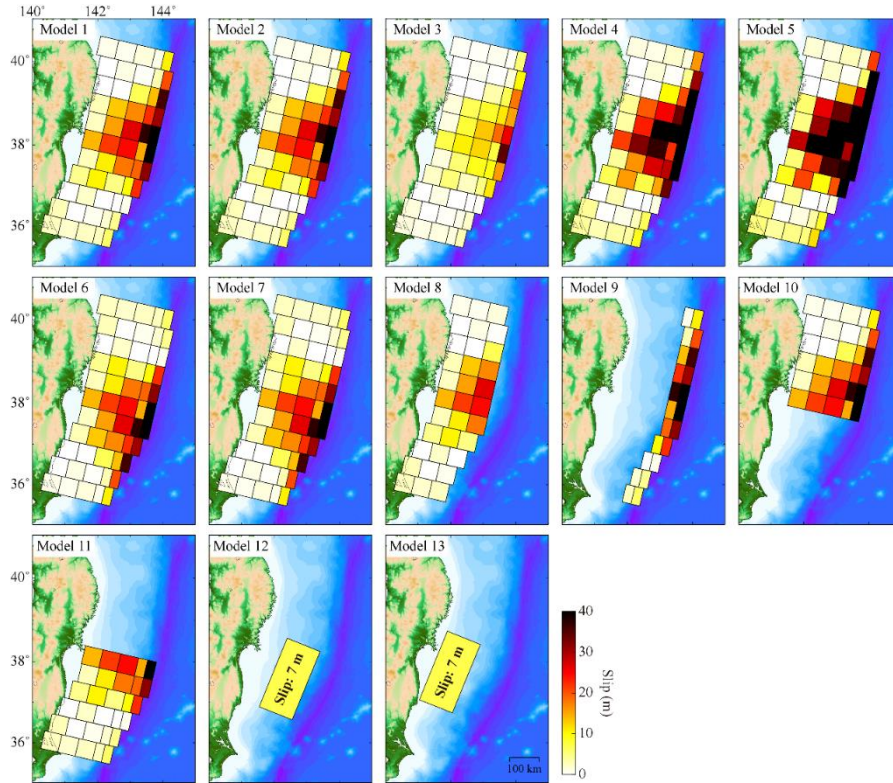


Figure 3-6. Fault models for initial tsunami source based on Satake *et al.* (2013) and Namegaya *et al.* (2010). Rupture propagation was considered only in Models 1 and 7, and the rupture was assumed to be instantaneous for the other models.

3-7. Model Accuracy

To assess the performance between the observations and simulations, statistical parameters (geometric mean: K , standard deviation: κ) were evaluated using the ratio of observed (O_i) and simulated (S_i) thickness at point i (Aida, 1978). The parameters were calculated by

$$\log K = \frac{1}{N} \sum_{i=1}^N \log \left(\frac{O_i}{S_i} \right)$$

$$\log \kappa = \sqrt{\frac{1}{N} \sum_{i=1}^N \left(\left(\log \left(\frac{O_i}{S_i} \right) \right)^2 - (\log K)^2 \right)}$$

Here, N is the total number of observations. The simulated results are better if the K and κ values are close to 1. The result indicates an underestimation of the observation result if the K value is larger than 1, whereas it shows an overestimation if the K value is smaller than 1. In this study, the numerical modeling is satisfactory if the K value is between 0.8 and 1.2 and roughly matches the observation if the value of K is from 0.6 to 1.4. In the same way, the tsunami inundation simulation agrees with the observations if the ratio of the observed and computed inundation areas ranges from 80 to 120 %.

CHAPTER 4. Tsunami Deposit Survey at the Idagawa Lowland

4-1. Sedimentary Facies and Stratigraphy

The sediment samples with a core length of 118-286 cm were collected (Table 3-1). The core sediments were mainly composed of sand with modern debris and terrestrial plants, agricultural soil containing many roots of terrestrial plants, gray to olive-gray silt, and six sand layers with shell fragments and heavy material laminae (Fig. 4-1). The seven sand layer units in the sediment were numbered from EV1 to EV7 in order from the top.

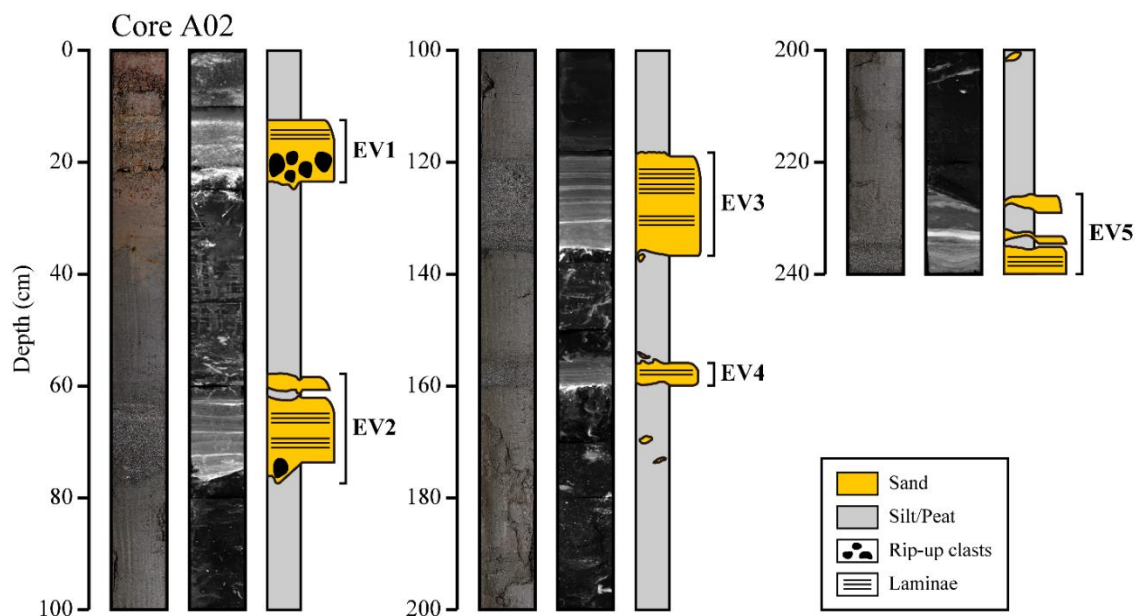


Figure 4-1. Photograph, CT image, and simple sketch with sedimentary structures of the sediment at the cores A02, A04, A06, A08, and B01.

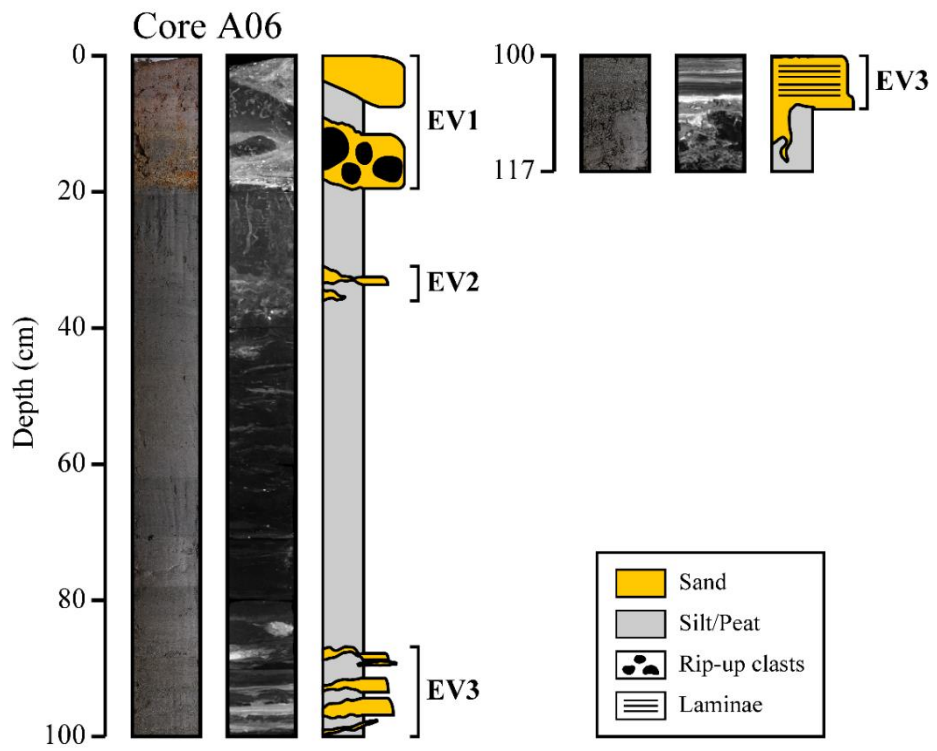
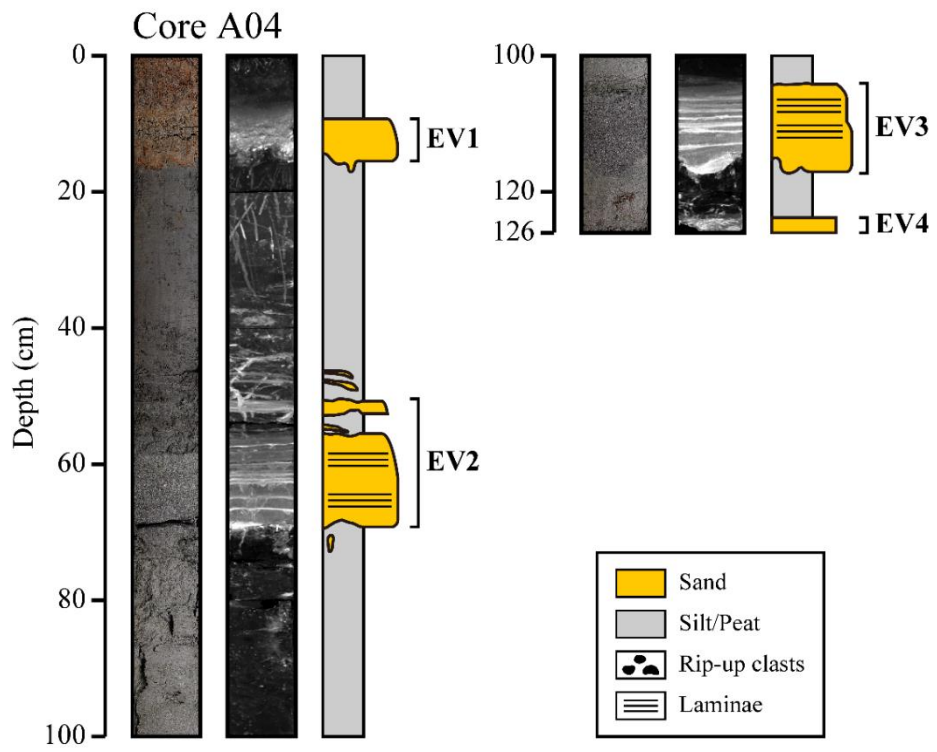


Figure 4-1. (continued)

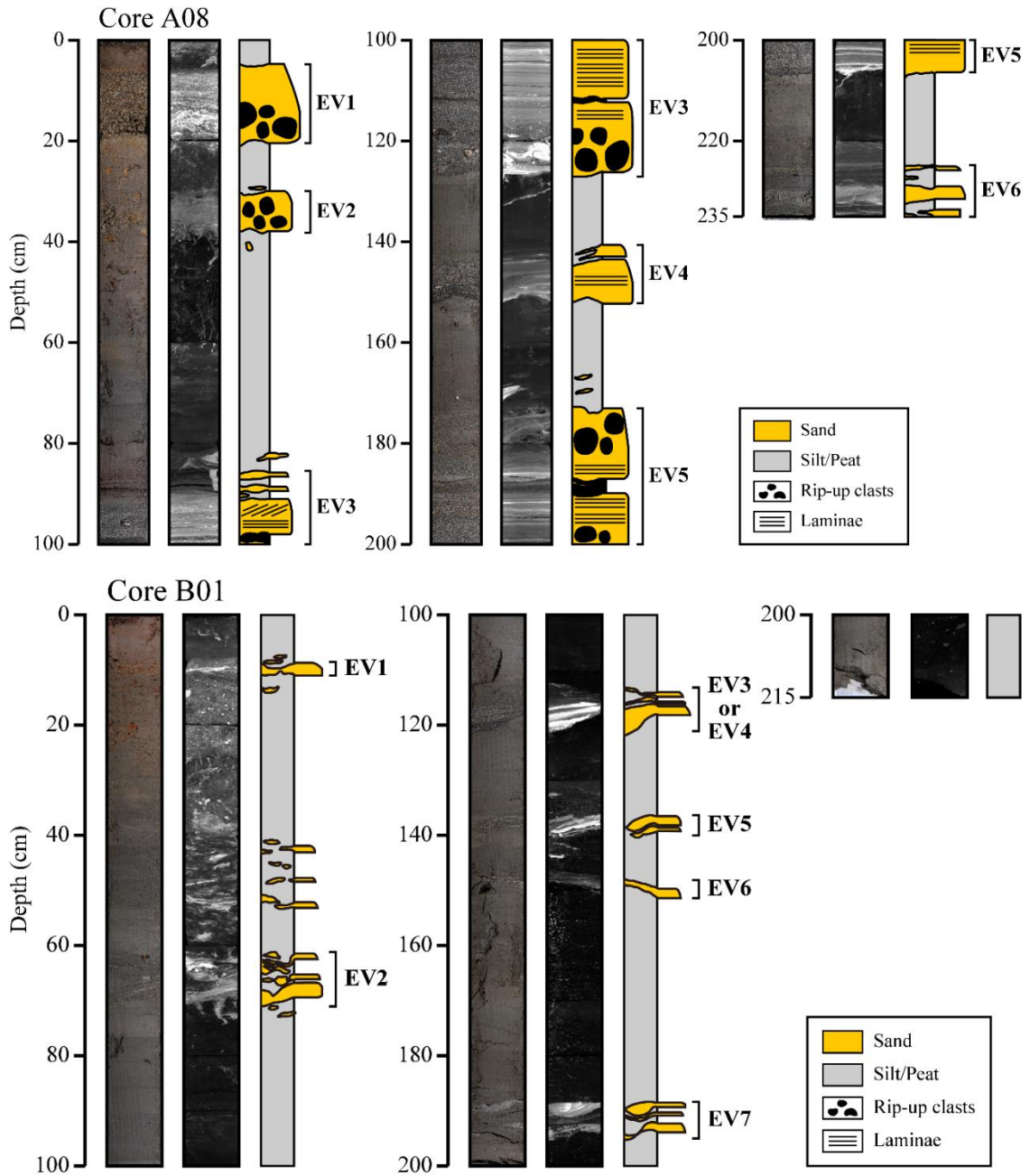


Figure 4-1. (continued)

The first event unit (EV1) mainly consisted of well-sorted and rounded medium to coarse sand (Fig. 4-2 and 4-9; mean: 1.3-2.9 phi, sorting: 0.6-1.3) that contained modern debris and terrestrial plants. The thickness of the EV1 unit was 15 cm in the core A08.

This sand unit had finer upward, parallel laminae, and erosional basal contacts (Table 4-1). Rip-up clasts of 3-4 cm in diameter were also found in the core B06 collected from the south side of the levee of the Miyata River. The EV1 unit was considered to be the 2011 Tohoku tsunami deposit because it covered the agricultural soil and contained modern debris.

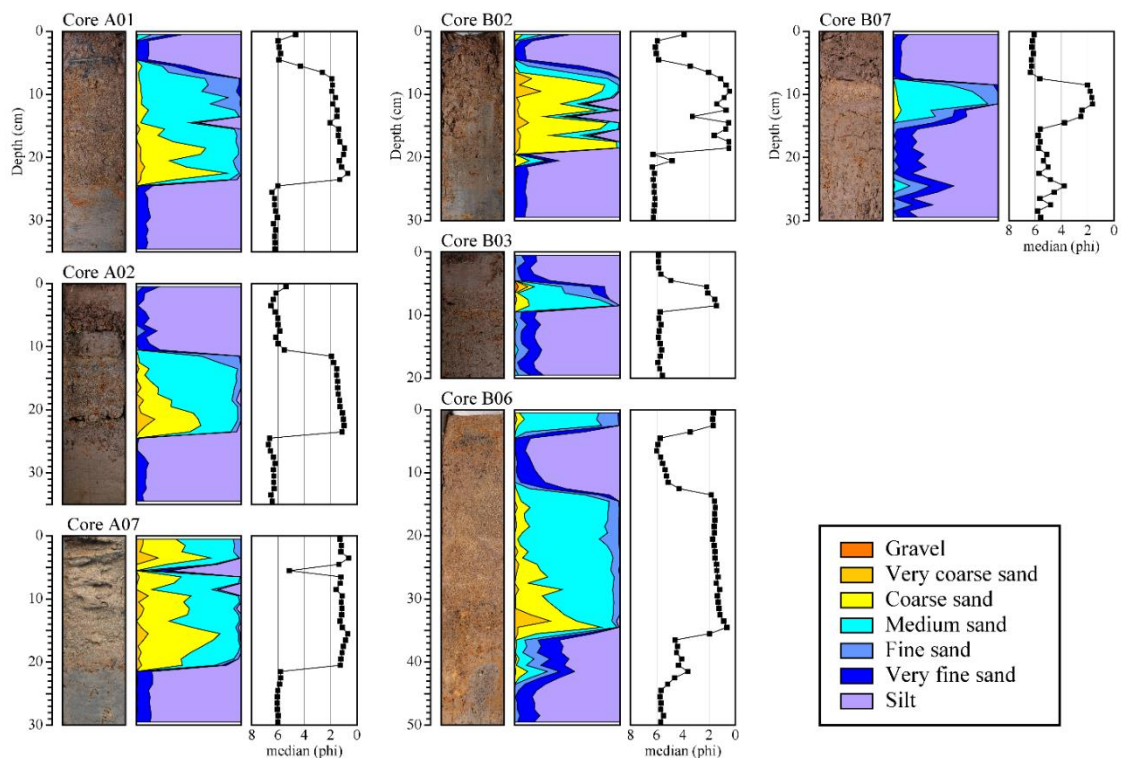


Figure 4-2. Vertical variation in grain size distributions of the EV1 unit.

About 10-15 cm below the EV1 unit was agricultural soil containing the roots of terrestrial plants. The sediment below the agricultural soil consisted mostly of gray to olive-gray silt (Fig. 4-9; mean: 5.1-6.0 phi, sorting: 1.7-2.1). This sediment is an ordinary deposit derived from the lagoon or inner bay. The boundary between the agricultural soil and inner bay silt was ambiguous in all cores.

The second event unit (EV2) consisted of fine to coarse sand (Fig. 4-3 and 4-9; mean:

1.5-5.1 phi, sorting: 0.4-2.2) with shell fragments. The thickness of this unit was 8 cm in the core A08. The EV2 unit had single normal graded bedding, rip-up clasts, erosional basal contact, and weak parallel laminae that were disturbed by bioturbation caused by terrestrial plants (Table 4-1). It was a massive sand layer on transect A-A', whereas it was thin or patches of sand on the north side of the Miyata River in transect B-B'.

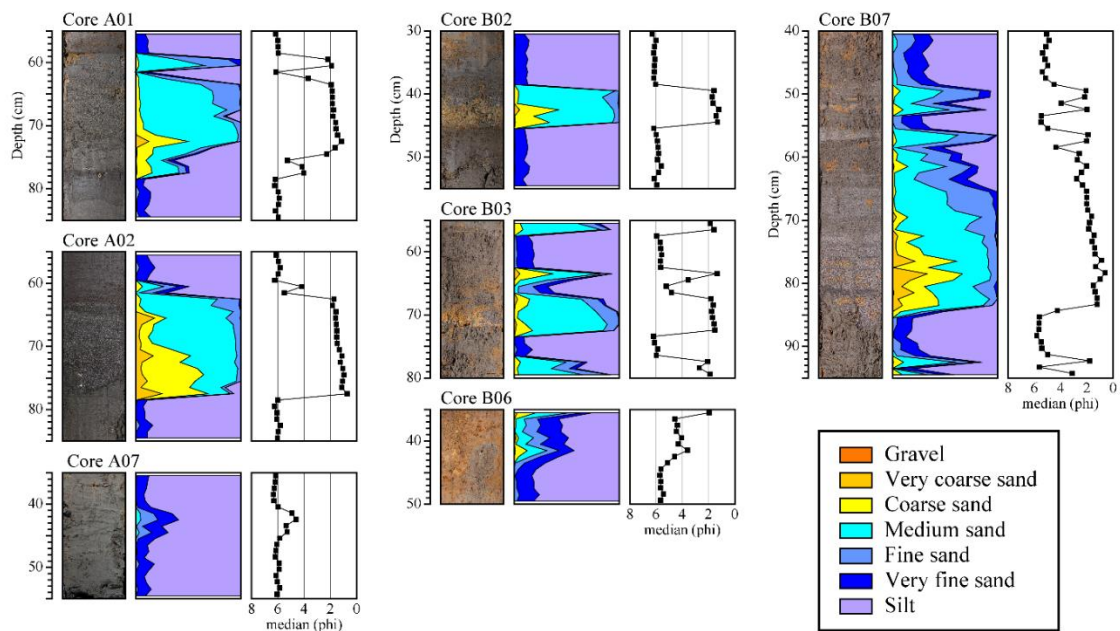


Figure 4-3. Vertical variation in grain size distributions of the EV2 unit.

The third event unit (EV3) consisted of fine to medium sand (Fig. 4-4 and 4-9; mean: 1.5-3.9 phi, sorting: 0.5-1.6) with an erosional contact and multiple normal/reverse grading structures. The EV3 unit was the thickest (41 cm) event deposit in the core A08. It had numerous parallel and trough-cross beddings and mud drapes inside the sand unit, climbing ripples, a humid layer at the top, and many shell fossils (e.g., *Corbicula japonica*, *Cyclina sinensis*, or *Macoma incongrua*) at the base (Table 4-1). The fourth event unit (EV4) was composed mainly of fine to coarse sand (Fig. 4-5 and 4-9; mean: 1.1-4.1 phi, sorting: 0.5-2.2). The EV4 unit was 11 cm thick in the core A08 and exhibited single

normal graded bedding, erosional basal contact, and weak parallel laminae (Table 4-1).

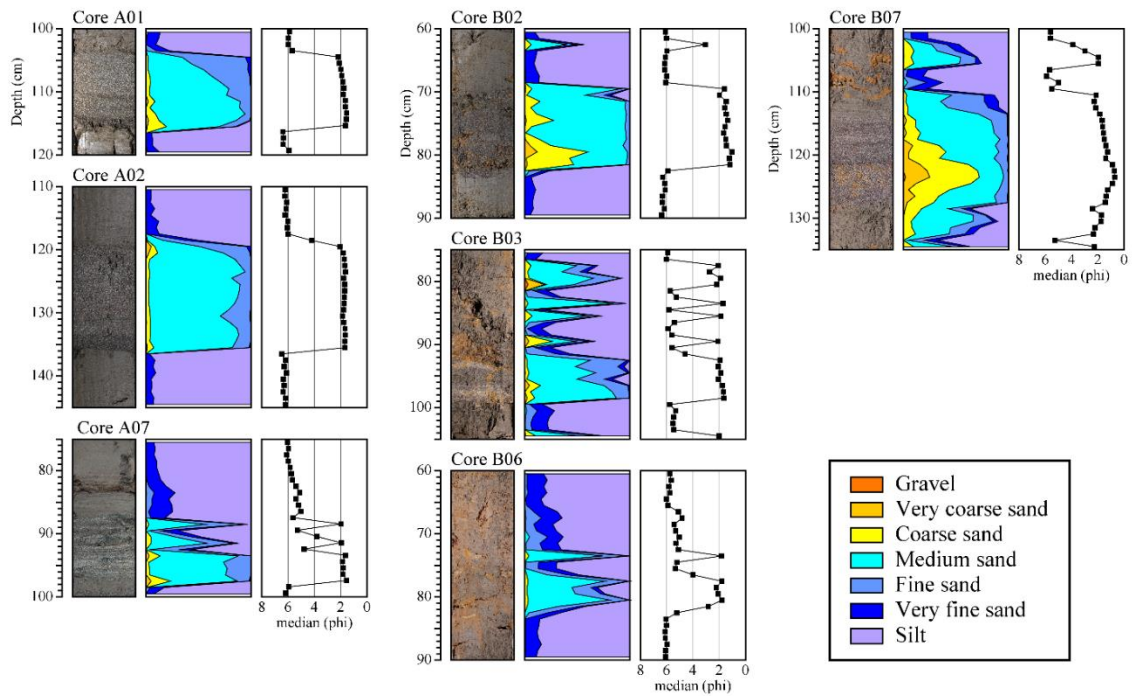


Figure 4-4. Vertical variation in grain size distributions of the EV3 unit.

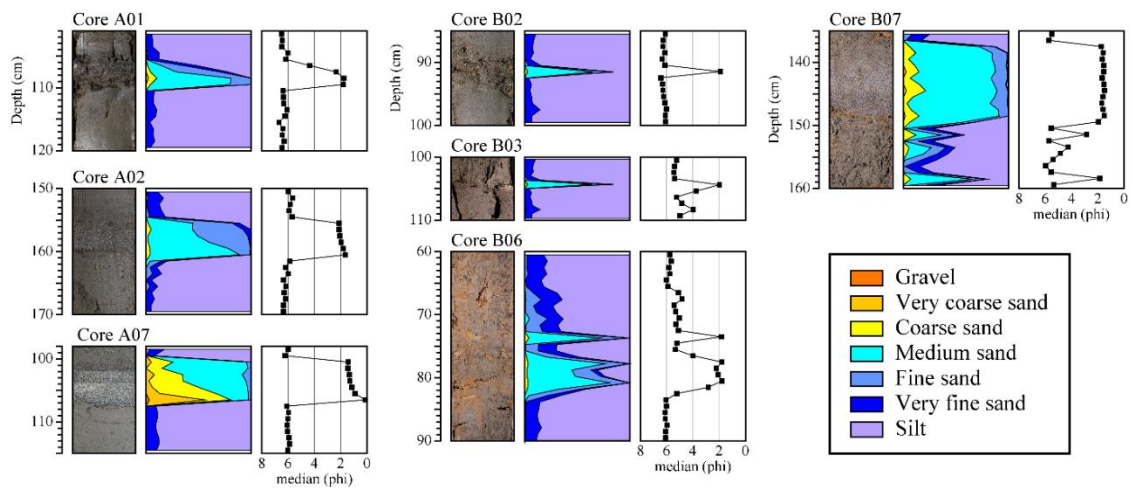


Figure 4-5. Vertical variation in grain size distributions of the EV4 unit.

The fifth event unit (EV5) consisted of fine to medium sand (Fig. 4-6 and 4-9; mean: 2.2-3.7 phi, sorting: 0.8-1.8) with shell fragments. The EV5 unit was 33 cm thick in the core A08 and contained many rip-up clasts at the top, numerous parallel and trough-cross

beddings, and multiple normal/reverse graded beddings (Table 4-1). The sixth event unit (EV6) was also composed of fine to medium sand (Fig. 4-7 and 4-9; mean: 1.5-4.3 phi, sorting: 0.4-1.7). The EV6 unit was more than 10 cm thick in the core A08 and also had parallel laminae and a single normal grading structure at the top (Table 4-1).

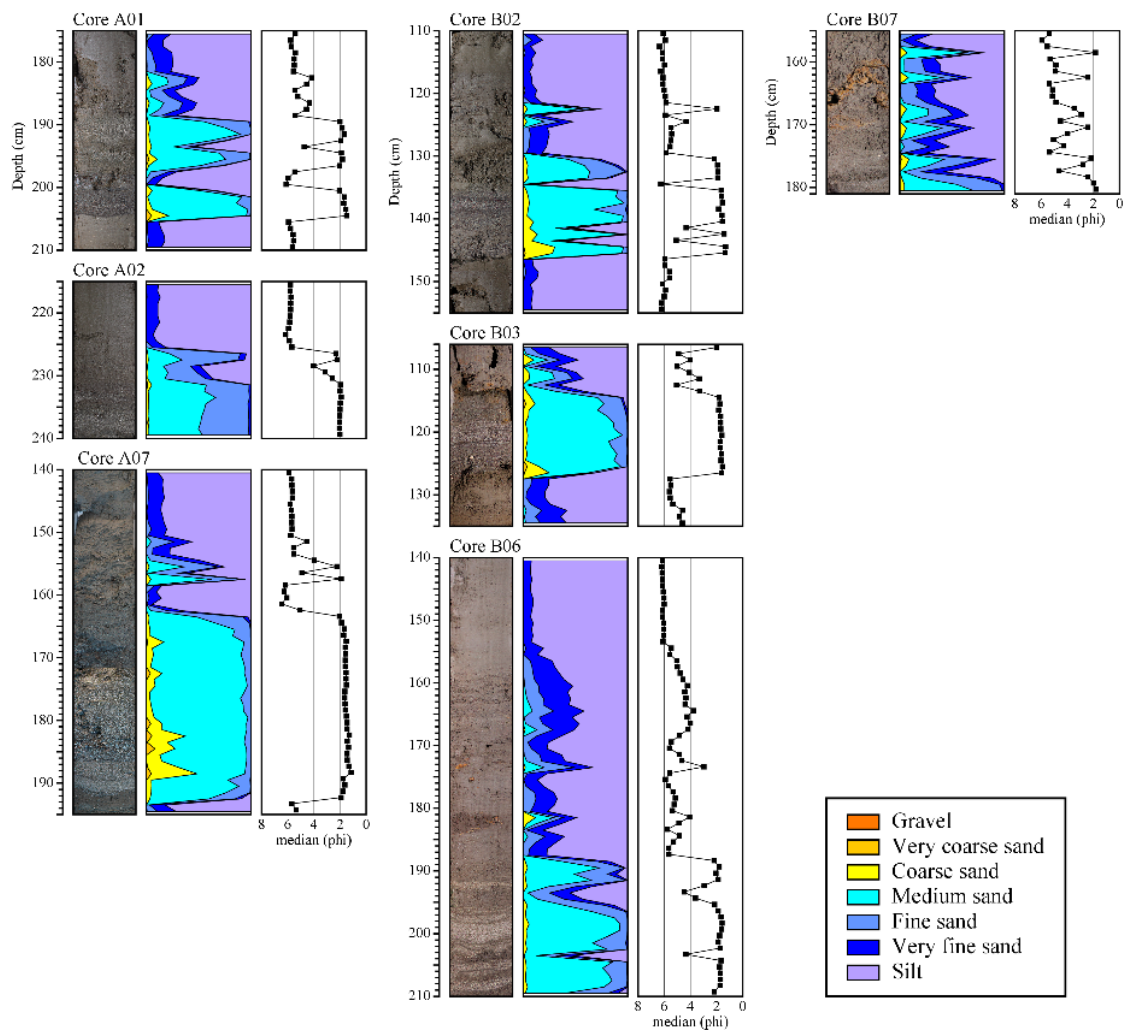


Figure 4-6. Vertical variation in grain size distributions of the EV5 unit.

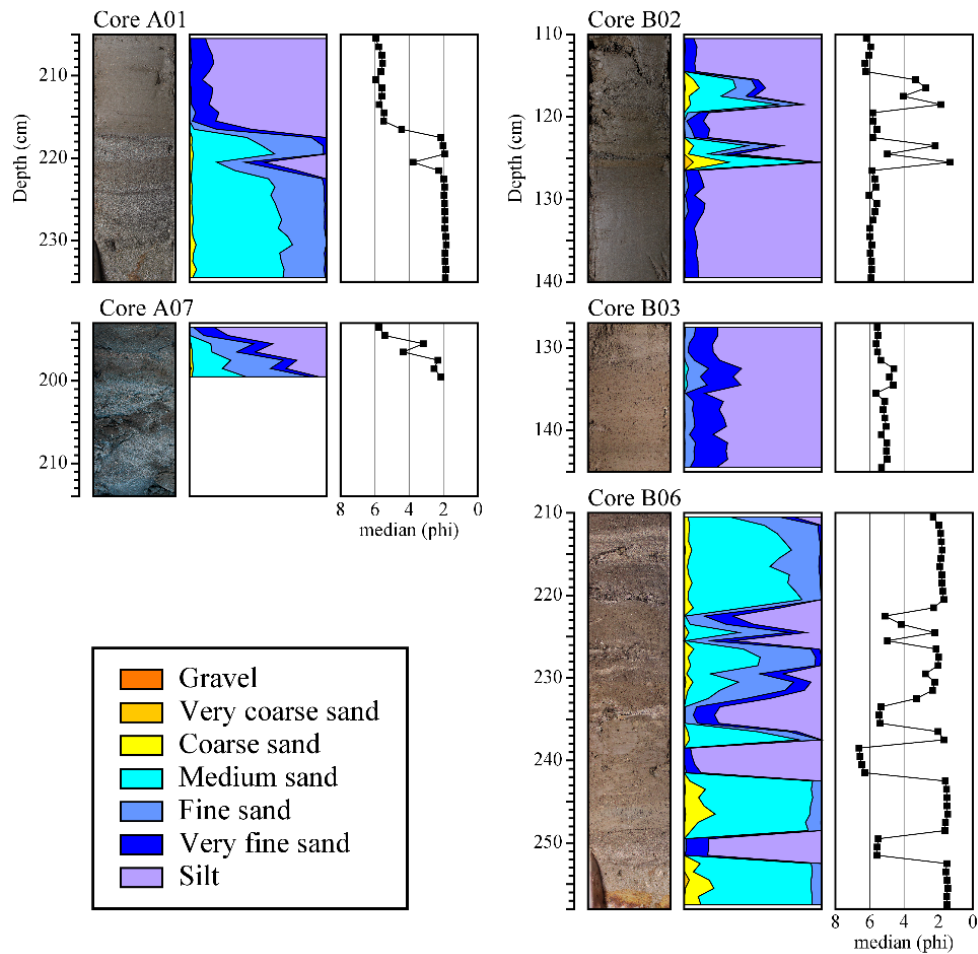


Figure 4-7. Vertical variation in grain size distributions of the EV6 unit.

The seventh event unit (EV7) consisted of fine to coarse sand (Fig. 4-8 and 4-9; mean: 2.6-3.7 phi, sorting: 1.5-1.8) with several rip-up clasts and an erosional basal contact (Table 4-1). The EV7 unit was 2-6 cm thick and the thickness increased to the north. The reason for this may be that the EV7 unit was selectively deposited so as to fill a depression, and that the water depth increased to the north.

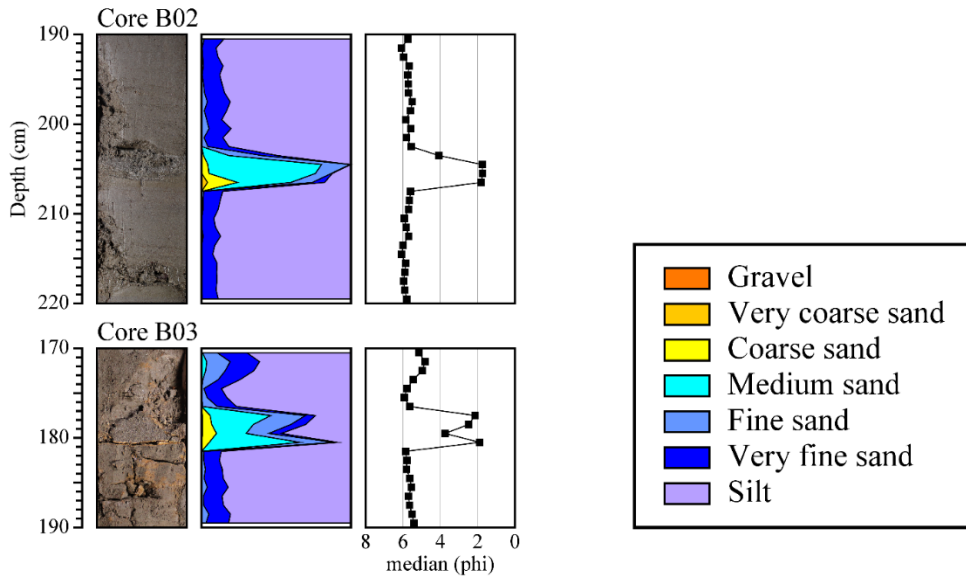


Figure 4-8. Vertical variation in grain size distributions of the EV7 unit.

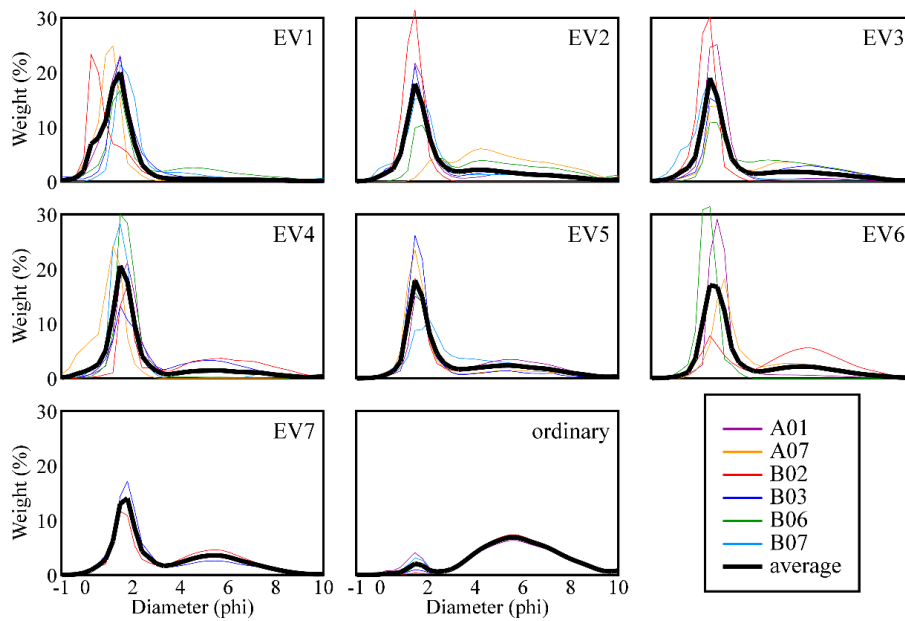


Figure 4-9. Grain size distributions of event and ordinary deposits.

Table 4-1. Sedimentological structures of event deposits

structures	EV1	EV2	EV3	EV4	EV5	EV6	EV7
Thickness	<36 cm	<23 cm	<41 cm	<22 cm	<66 cm	<32 cm	2-6 cm
Number of subunits	at least 3 subunits	at least 3 subunits	>4 subunits	one subunit	>3 subunits	<2 subunits	<2 subunits
grading structure	single	single	single/multiple	single	single/multiple	single	single
the other structures	erosional contact bioturbations modern debris	erosional contact bioturbations	erosional contact dense parallel and cross laminae, and climbing ripple	erosional contact	erosional contact dense parallel and cross laminae, and climbing ripple	erosional contact Hummocky cross-lamination	erosional contact load casts
rip-up clasts	commonly	commonly	commonly	rarely	commonly	commonly	rarely
mud drapes/mud cap	commonly	rarely	commonly	rarely	commonly	rarely	rarely
lateral continuity	thin in the center of lowland thick inland and backshore	thin in the center of lowland thick inland and backshore	thinner landward	thinner landward	thinner landward	thinner landward	thicker northward

4-2. Lateral Continuity of Event Deposits

Since the EV3 and EV5 units were much thicker than the other event deposits and contained numerous parallel and trough-cross beddings, they could be clearly identified in all of the cores. In this study, therefore, the EV1, EV3, and EV5 units were used as stratigraphic marker layers for comparing event deposits.

The EV1 unit covered the ground surface and the sediment thickness varied from 3 to 36 cm (Fig. 4-10 and 4-11). It became thinner in the cores A04, A05, and A06 which were sampled in the center of the lowland. Conversely, it became thicker and clearer inland and backshore.

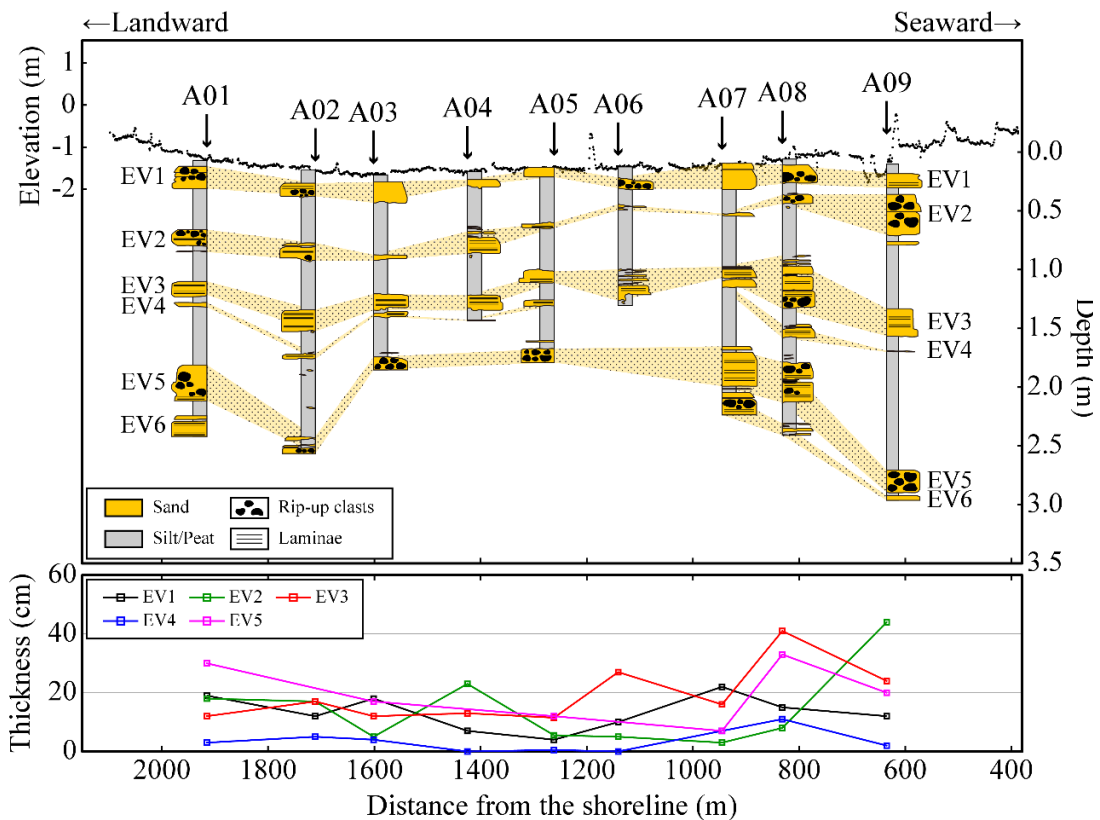


Figure 4-10. Stratigraphic comparison and distribution of sediment thickness for event deposits along transect A-A' based on sedimentary facies, grain size distribution, and radiocarbon dating. The location of transect A-A' is shown in Figure 3-1.

The EV2 unit was laterally identified between the EV1 and EV3 units on transect A-A'. The thickness varied from 3 to 23 cm (Fig. 4-10 and 4-11). The EV2 unit was almost invisible in the cores A06 and A07 sampled in the center of the lowland and the cores collected on transect B-B' without the results of CT image or grain size analysis. Conversely, it became thicker and clearer inland and backshore.

The EV4 unit was identified about 5-19 cm below the EV3 unit. The thickness ranged from 2 to 11 cm (Fig. 4-10 and 4-11), and it became thinner further inland. The EV3 and EV4 units could be distinguished in the cores sampled from the south side of the Miyata River, but they could not be separated on the north side.

The EV6 unit was identified about 2-18 cm below the EV5 unit. It was usually thicker than 10 cm on the south side of the Miyata River (Fig. 4-10) and 2-3 cm thick on the north side (Fig. 4-11). The EV5 and EV6 units could be distinguished in the cores collected on the south side of the Miyata River, but they could not be separated on the north side, similar to the EV3 and EV4 units.

Event deposits (EV1-EV6) extended about 2 km from the coast and typically became thinner landward. Only the EV7 unit could not be identified on the south side of the Miyata River, probably because the sedimentation rate on transect B-B' was slower than that on transect A-A'. It might be possible to identify the EV7 unit on the south side of the Miyata River if longer cores could be obtained along transect A-A'.

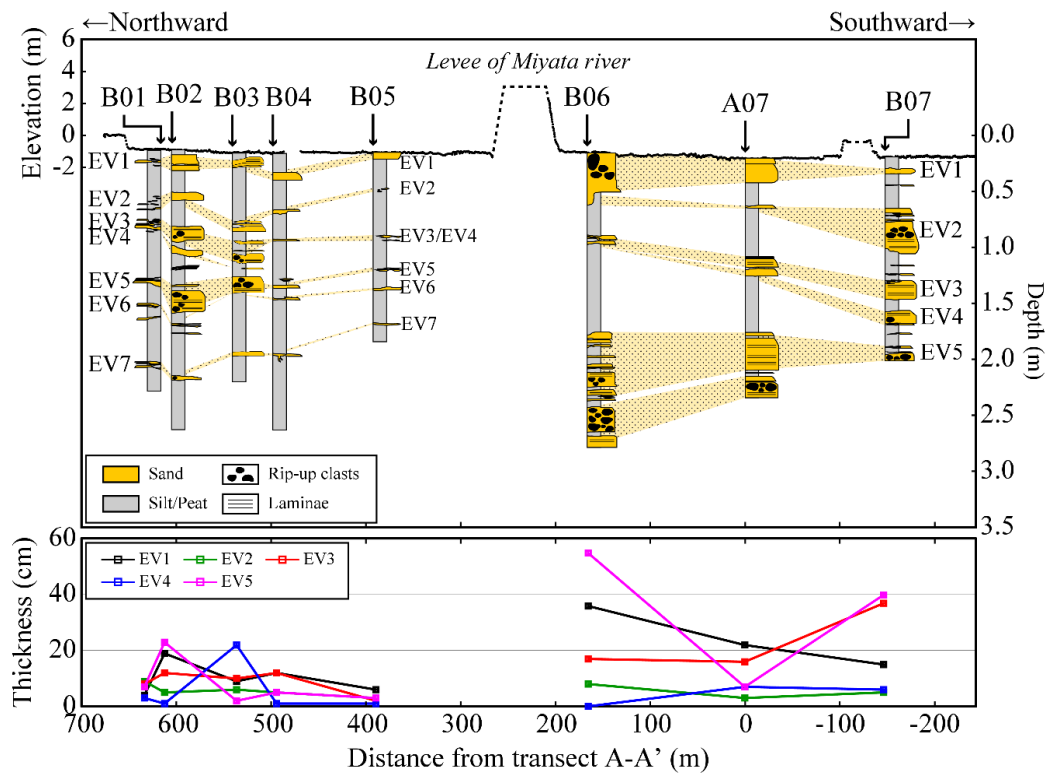


Figure 4-11. Stratigraphic comparison and distribution of sediment thickness for event deposits along transect B-B' based on sedimentary facies, grain size distribution, and radiocarbon dating. The location of transect B-B' is shown in Figure 3-1.

4-3. Diatom and Foraminiferal Assemblages

The sediment in the core A02 can be divided into three main diatom zones (zones I, II, and III) from the change of diatom components and dominate species of counted total diatoms (Fig. 4-12 and Fig. 4-13). Additionally, zone II can be separated into four subunits (zones IIa, IIb, IIc, and IId) for each sediment between event deposits. In diatom zone I (195-220 cm depth), brackish to marine diatoms (e.g., *Cocconeis scutellum*, *Cyclotella striata-stylorum* and *Mastogloia spp.*) occupied 28-32 % of the total, although the limobiontic diatoms in the freshwater (e.g., *Cocconeis placentula*, *Aulacoseira*

alpigena-distans, and *Fragilaria exigua*) also appeared (18-23 %). In diatom zone II (40-190 cm depth), marine, marine to brackish, and brackish diatoms dominantly appeared. In diatom zone IIa (165-190 cm depth), marine diatoms (*Chaetoceros spp.* and *Nitzschia lanceola*) and species inhabiting inner bays (*Paralia sulcata* and *Cyclotella striata-stylorum*) were most dominant at the base, whereas species inhabiting brackish mudflats (*Melosira sp. n.*) increased upward. Between the EV3 and EV4 units (diatom zone IIb; 140-150 cm depth), species inhabiting inner bays (*Paralia sulcata*) and marine seaweed beds (*Cocconeis scutellum*) were dominant at the base, and decreased upward. Rheobiontic diatoms (*Cocconeis placentula*) and species inhabiting brackish mudflats (*Melosira sp. n.*) were also abundant just below the EV4 unit. Between the EV2 and EV3 (diatom zone IIc; 80-115 cm depth), species inhabiting inner bays (*Paralia sulcata* and *Cyclotella striata-stylorum*), marine seaweed beds (*Cocconeis scutellum*), and brackish mudflat (*Melosira sp. n.*) dominantly appeared, and decreased upward. The brackish to marine, brackish to freshwater, and freshwater diatoms increased upward. In diatom zone IIId (40-55 cm depth), species inhabiting inner bays (*Paralia sulcata*) and marine seaweed beds (*Cocconeis scutellum*) were abundant at the base, and decreased upward. Species of brackish mudflats (*Melosira sp. n.*) were also dominant below the EV2 unit. In diatom zone III (0-40 cm depth), freshwater diatoms occupied more than 50 % of the total and the limobiontic diatoms (*Fragilaria exigua*) were dominant. The rheobiontic diatoms also appeared in the sediment, but they were not abundant.

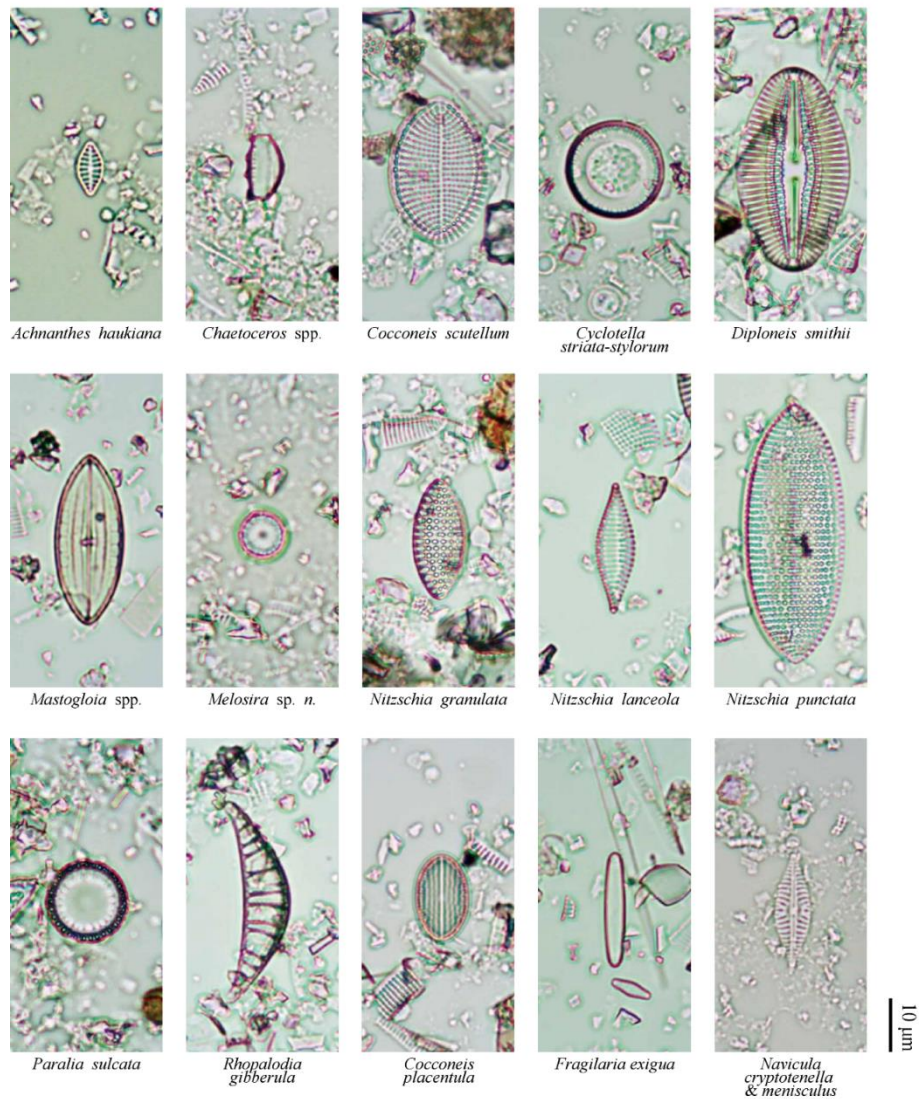


Figure 4-13. Micrographs of typical diatoms in the core A02.

Coccoliths and *Sponge spicules* appeared everywhere in the core A02 except between the EV3 and EV4 units, but few *silicoflagellates* were detected (Fig. 4-14). *Coccoliths* in silt usually had an average of 7-12 counts (level I to II in appearance level) per sample, although there was a gradual peak (level IV to VI in appearance level) at 180-210 cm in depth. The appearance levels of *Coccoliths* in event deposits were much higher than that in silt; 8-26 counts (I to III) in the EV1 unit, 168-830 counts (VII to XIV) in the EV2 unit, 474-702 counts (X to XIII) in the EV3 unit, 81-186 counts (VI to VII) in the EV4 unit,

and 4-224 counts (I to VIII) in the EV5 unit. In contrast, it seems that the peaks of *Sponge spicules* were not correlated with the event deposits.

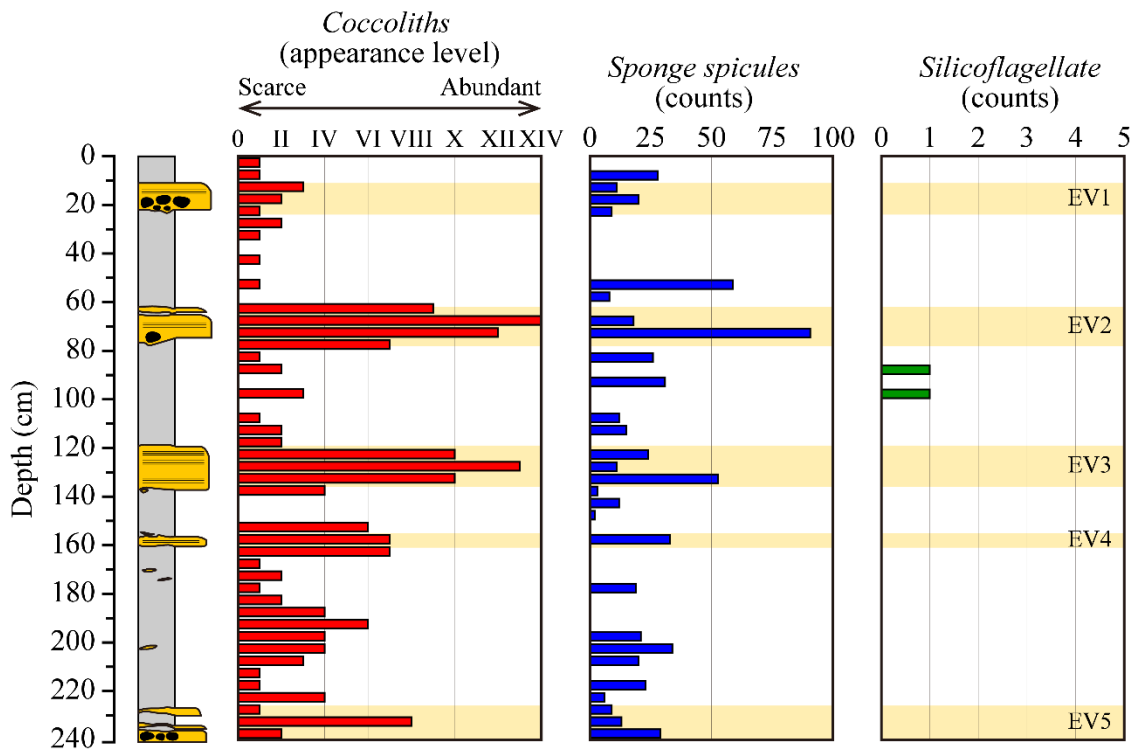


Figure 4-14. Vertical changes in appearance levels and count number for *Coccoliths*, *Sponge spicules*, and *Silicoflagellates* in the core A02.

4-4. Identification of Tsunami Deposits

Event deposits commonly became thinner landward and had normal grading structures and parallel laminae. These characteristics indicate that the direction of the flow which transported sand particles was landward and that the speed of the flow decreased landward. It can also be inferred that the source of the sand was a sand beach or shallow seafloor because the sand units contained brackish or marine shell fossils and fragments. In addition, load marks and erosional contacts suggested that the flow caused significant

scouring. Therefore, the events were transported from the ocean to the land by either storms or tsunamis.

Criteria for distinguishing between storm and tsunami deposits have been reported widely (e.g., Nanayama *et al.*, 2000, Morton *et al.*, 2007; Komatsubara *et al.*, 2008; Peters and Jaffe, 2010; Richmond *et al.*, 2011; Engel and Brückner, 2011). A tsunami deposit is formed by the collapse of sand dunes due to very long waves. It exhibits sedimentological characteristics that include strong erosion, microfossils and marine diatoms that inhabit waters deeper than the level of the wave base and the sedimentary environment changes before and after the events due to coseismic subsidence/uplift. Typical tsunami deposits often have a single normal grading structure, and monotonic parallel laminae because sand particles are transported mostly in suspension (Morton *et al.*, 2007; Bryant, 2014). Tsunamis contain more energy than storm surges and therefore their deposits are typically distributed far from the shore. In contrast, a typical storm deposit is formed by the collapse of sand dunes due to a gradual sea-level rise and many short waves. It has many parallel, cross laminations, and climbing ripples because the sand is transported by traction (Morton *et al.*, 2007; Bryant, 2014). In addition, the depositional distribution and the distance from the shore of storm deposits are generally narrower and shorter than those of tsunami deposits because storm wavelengths are relatively short (e.g., Tuttle *et al.*, 2004; Kortekaas and Dawson, 2007; Morton *et al.*, 2007; Nishimura, 2009; Komatsubara, 2012).

Among the seven event deposits in the study area, the sketches and CT images indicated that only the EV3 and EV5 units contained more than 30 parallel and cross beddings formed by multiple short period waves and they were thicker than the other event deposits (Fig. 4-15 and Table 4-1). Their sedimentary characteristics were significantly different from the other event deposits (EV2, EV4, EV6, and EV7) formed

in the same subaqueous environment and similar to those of storm deposits (Nanayama *et al.*, 2000; Morton *et al.*, 2007; Chaumillon *et al.*, 2017). Thus, it is possible that the EV3 and EV5 units were not caused by a tsunami but some other event (such as storm surges due to typhoons and/or environmental changes by earthquakes and tsunamis). Storm events occur more frequently than tsunami events, but the sand is not transported inland by storm surges because sand dunes act as a barrier. If a sand dune is collapsed by larger tsunami events, there is nothing to prevent a wave before redevelopment of the dune. During this period, storm surges can easily transport sand to the inner part of the bay. Event deposits corresponding to storm deposits (EV3 and EV5) were only identified just above tsunami deposits (EV4 and EV6), suggesting that the above hypothesis is consistent with the observations.

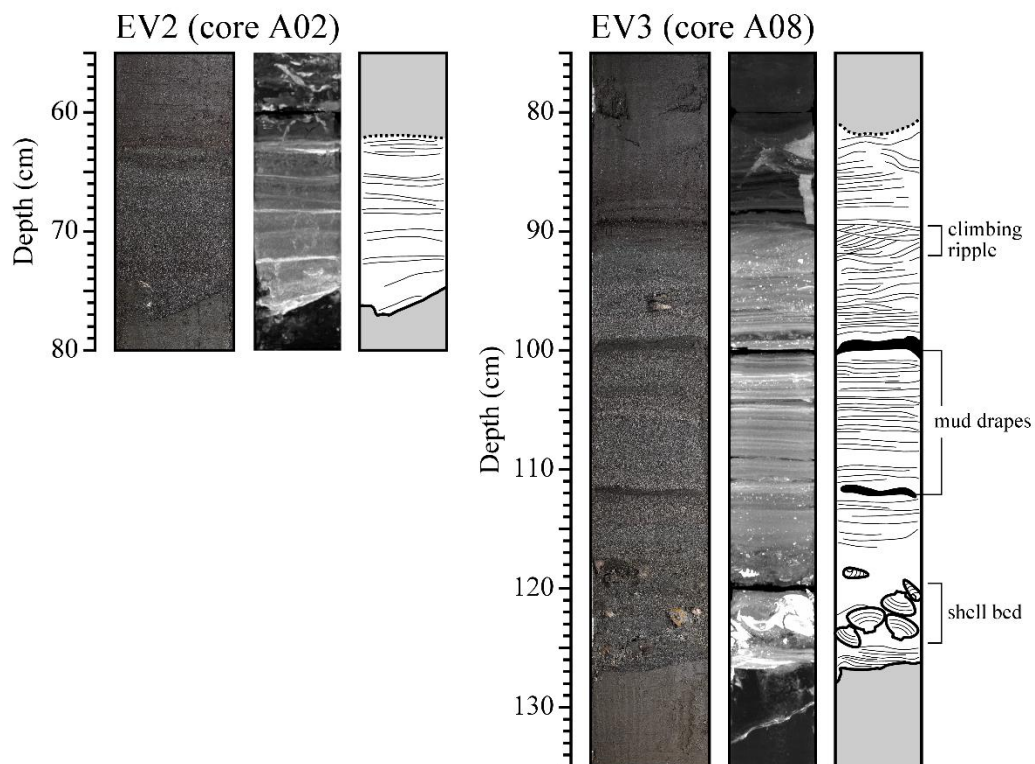


Figure 4-15. Photographs, CT images, and sketches of the EV2 and EV3 units.

The other five event deposits (EV1, EV2, EV4, EV6, and EV7) exhibited a single normal structure, parallel laminae, and rip-up clasts (Fig. 4-15 and Table 4-1). The sedimentary features revealed the following series of depositional processes: (1) the ordinary deposits were eroded by the flow and suspended in the water as rip-up clasts; then, as the speed of the flow decreased, (2) the deposited sand particles decreased in size sequentially from coarse to fine sand. These characteristics are similar to those of typical tsunami deposits (e.g., Fujiwara and Kamataki, 2007; Morton *et al.*, 2007; Komatsubara *et al.*, 2008; Fujiwara *et al.*, 2013). Therefore, it is concluded that the deposits (EV2, EV4, EV6, and EV7) were derived from paleo-tsunamis.

4-5. Depositional Ages and Recurrence Intervals

Radiocarbon ages measured from wood and plant fragments at the base of cores A01, A07, and B02 were 2180-2360, 2370-2710 and 3580-3820 cal. yrBP (Table 4-2). These results show that the cores sampled from the south and north sides of the Miyata River recorded geological events during the past 2700 and 3800 years, respectively. The ¹⁴C ages of three samples just below the EV1 unit in core A01 ranged from 1060-2690 cal. yrBP, unusually old ages at shallow depths (Fig. 4-16). These data were not used for subsequent analysis because the ground surface may have been covered with agricultural soil that included old organic matter after land reclamation. The data were also removed if the agreement indices between the models and measurements were less than 60% (Fig. 4-16).

Table 4-2. Detailed results of radiocarbon dating^a.

Serial No.	Site	Depth (cm)	Materials	$\delta^{13}\text{C}$ (‰)	^{14}C age (yr BP)	2 σ Calendar age (BC/AD)	Lab Number
1	A09	45	shell	1.81±0.8	1157±25	1180 cal AD-1300 cal AD	IAAA-143674
2	A09	130	shell	1.82±0.5	2606±25	400 cal BC-230 cal BC	IAAA-143675
3	A09	165	shell	3.07±0.3	2686±26	520 cal BC-350 cal BC	IAAA-143676
4	A09	252	shell	1.15±0.53	2659±25	490 cal BC-340 cal BC	IAAA-143677
5	A07	128	shells	1.34±0.41	2368±26	150 cal BC-50 cal AD	IAAA-143678
6	A07	131	plant fragments	-26.54±0.23	1948±24	1 cal AD-130 cal AD	IAAA-143679
7	A07	198	wood	-22.79±0.53	2461±26	760 cal BC-430 cal BC	IAAA-143680
8	A05	77	shells	-5.93±0.31	843±25	1430 cal AD-1530 cal AD	IAAA-143682
9	B02	22.5	seeds	-31.52±0.28	-924±30	modern	TKA-16943
10	B02	52.5	plant fragments	-19.86±0.29	886±31	1030 cal AD-1220 cal AD	TKA-16944
11	B02	92.5	seeds	-18.08±0.3	1718±31	240 cal AD-400 cal AD	TKA-16945
12	B02	102.5	charcoals	-20.07±0.3	2166±32	360 cal BC-110 cal BC	TKA-16946
13	B02	147.5	seeds	-14.2±0.29	2281±32	410 cal BC-210 cal BC	TKA-16947
14	B02	152.5	charcoals	-11.12±0.35	2313±31	420 cal BC-230 cal BC	TKA-16948
15	B02	177.5	charcoals	-23.31±0.28	2751±32	980 cal BC-820 cal BC	TKA-16949
16	B02	187.5	charcoals	-26.5±0.28	2563±32	810 cal BC-550 cal BC	TKA-16950
17	B02	197.5	charcoals	-22.32±0.28	2686±32	910 cal BC-800 cal BC	TKA-16951
18	B02	218	plant fragments	-29.56±0.43	2603±26	820 cal BC-770 cal BC	IAAA-143681
19	B02	240	wood	-26.75±0.51	3415±26	1870 cal BC-1630 cal BC	IAAA-142311
20	A01	27.5	charcoal	-23.57±0.31	1217±30	690 cal AD-890 cal AD	TKA-16933
21	A01	29	charcoal	-27.58±0.31	2402±32	740 cal BC-390 cal BC	TKA-16934
22	A01	32.5	charcoal	-28.15±0.3	1529±31	420 cal AD-600 cal AD	TKA-16935
23	A01	78	shell	-3.14±0.57	1003±24	1310 cal AD-1420 cal AD	IAAA-142312
24	A01	82.5	charcoals	-22.5±0.3	1176±31	760 cal AD-970 cal AD	TKA-16936
25	A01	87.5	seeds	-19.22±0.32	1273±31	660 cal AD-860 cal AD	TKA-16937
26	A01	92.5	plant fragments	-29.79±0.29	1314±31	650 cal AD-770 cal AD	TKA-16938
27	A01	100	charcoals	-25.77±0.56	1658±25	260 cal AD-530 cal AD	IAAA-142313
28	A01	117.5	seeds	-21.79±0.36	1618±32	350 cal AD-540 cal AD	TKA-16939
29	A01	137.5	seeds	-29.88±0.31	1754±32	170 cal AD-390 cal AD	TKA-16940
30	A01	152.5	plant fragments	-30±0.34	1857±32	70 cal AD-240 cal AD	TKA-16941
31	A01	167.5	plant fragments	-25.07±0.3	2480±32	780 cal BC-430 cal BC	TKA-16942
32	A01	183	charcoals	-30.54±0.55	1961±24	30 cal BC-90 cal AD	IAAA-142314
33	A01	230	wood	-25.07±0.62	2312±27	420 cal BC-230 cal BC	IAAA-142315

^a Radiocarbon ages are corrected for isotope fractionation effect by $\delta^{13}\text{C}$ values.

Laboratory numbers (TKA and IAAA) show the Laboratory of Radiocarbon Dating at the University Museum, the University of Tokyo and Institute of Accelerator Analysis Institute, respectively.

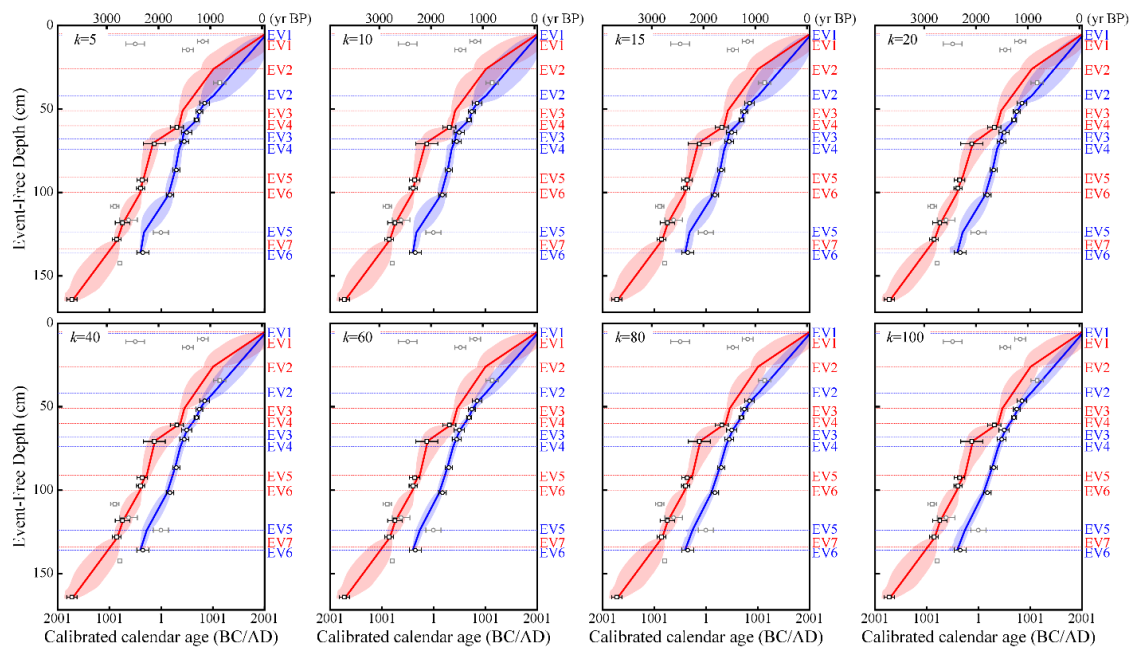


Figure 4-16. Age-depth models with different k values. Circles and bars indicate individual mean and 2σ error, respectively. The black symbols indicate data used to constrain the models; data indicated by gray symbols were not used. The solid line and shading show the modeled mean value and the 2σ range, respectively.

The depositional ages and recurrence intervals of events estimated from the age-depth models were slightly different with a Poisson parameter k (Fig. 4-16, Tables 4-3 and 4-4). For example, the depositional age of the EV2 unit was AD 770 to AD 1340 ($k=5$), AD 770 to AD 1340 ($k=10$), AD 780 to AD 1290 ($k=15$), AD 800 to AD 1290 ($k=20$), AD 830 to AD 1200 ($k=40$), AD 850 to AD 1170 ($k=60$), AD 860 to AD 1160 ($k=80$), and AD 880 to AD 1150 ($k=100$). In this study, the optimum k value was 18 cm^{-1} , which is the average for all cores (Table 3-3).

The models showed a continuous deposition of ordinary deposits because the age-gaps above and below the event deposits and a rapid change in the sedimentary rate were not identified. The average sedimentation rate was slightly higher in the core A01 than in the

core B02. The average sedimentation rate for both cores between the EV3 and EV5 units was about 1.4-2.0 mm/year, but it decreased to about 0.3-0.6 mm/year after the deposition of the EV3 unit. The depositional ages of event deposits constrained in the models of both cores are: EV2, AD 800 to AD 1310; EV3, AD 360 to AD 530; EV4, AD 270 to AD 440; EV5, 400 BC to 180 BC; EV6, 460 BC to 370 BC; and EV7, 1210 BC to 810 BC (Fig. 4-16 and Table 4-3). The time intervals between the event deposits can be grouped into longer and shorter intervals (Fig. 4-16 and Table 4-4). The shorter intervals are less than 230 years (EV3-EV4 and EV5-EV6), and the longer intervals are about 510-900 years (EV1-EV2, EV2-EV3, EV4-EV5, and EV6-EV7).

The model certainty was also examined by comparing the above results with those from another Bayesian age-depth model (e.g., Bacon, CLAM, Bchron). For the Bacon software (Blaauw and Christen, 2011), the depositional ages of event deposits were constrained as follows; EV2, AD 790 to AD 1650; EV3, AD 340 to AD 880; EV4, AD 180 to AD 450; EV5, 410 BC to AD 20; EV6, 560 BC to 130 BC; EV7, 1050 BC to 830 BC. The results were in good agreement with the results constrained from the OxCal program, therefore the age-depth models for the cores A01 and B02 were compared with general models.

Table 4-3. Depositional ages for different *k* values

<i>k</i>	EV2	EV3	EV4	EV5	EV6	EV7
5	AD 770 – AD 1340	AD 340 – AD 520	AD 250 – AD 420	400 BC – 230 BC	440 BC – 370 BC	1260 BC – 800 BC
10	AD 770 – AD 1340	AD 340 – AD 510	AD 250 – AD 420	400 BC – 230 BC	450 BC – 370 BC	1260 BC – 800 BC
15	AD 780 – AD 1290	AD 350 – AD 520	AD 250 – AD 420	400 BC – 220 BC	610 BC – 370 BC	1260 BC – 800 BC
20	AD 800 – AD 1290	AD 360 – AD 530	AD 270 – AD 430	390 BC – 210 BC	560 BC – 370 BC	1210 BC – 810 BC
40	AD 830 – AD 1200	AD 370 – AD 530	AD 290 – AD 450	380 BC – 200 BC	460 BC – 370 BC	1250 BC – 800 BC
60	AD 850 – AD 1170	AD 390 – AD 520	AD 310 – AD 450	360 BC – 190 BC	460 BC – 370 BC	1250 BC – 800 BC
80	AD 860 – AD 1160	AD 400 – AD 530	AD 320 – AD 460	390 BC – 180 BC	480 BC – 370 BC	1250 BC – 800 BC
100	AD 880 – AD 1150	AD 400 – AD 530	AD 320 – AD 460	400 BC – 190 BC	580 BC – 360 BC	1250 BC – 800 BC

Table 4-4. Recurrence intervals of event deposits for different k values

k	EV1-EV2	EV2-EV3	EV2-EV4	EV3-EV4	EV4-EV5	EV4-EV6	EV5-EV6	EV6-EV7
5	780-1230	290-800	400-900	<230	490-780	640-820	<230	400-880
10	780-1230	290-800	400-900	<230	490-780	640-830	<230	400-880
15	780-1230	290-800	400-900	<220	490-780	650-860	<250	390-900
20	780-1230	290-800	400-890	<210	510-780	670-890	<270	380-830
40	780-1230	290-800	380-880	<190	520-800	690-870	<240	400-870
60	780-1230	290-800	380-870	<180	530-800	710-870	<240	390-910
80	780-1230	290-800	380-870	<180	540-800	710-880	<260	380-910
100	780-1230	290-800	370-860	<170	540-810	710-940	<310	330-910

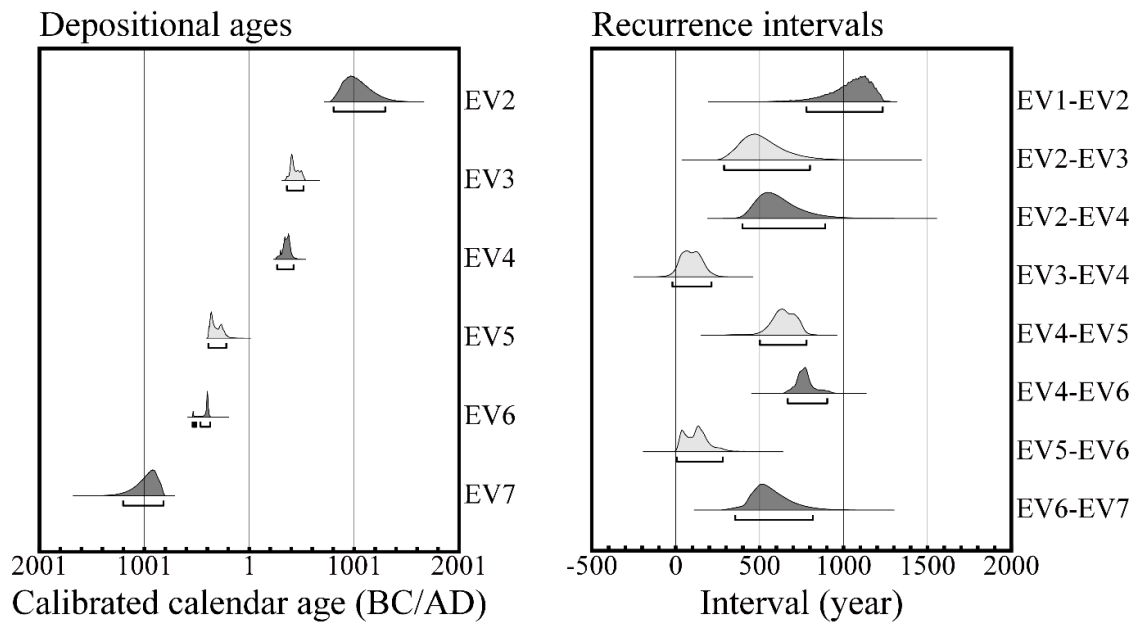


Figure 4-17. Depositional ages of event deposits and time intervals between event deposits estimated from the cores A01 and B02. The dark and light gray shading show probability densities and time intervals between tsunamis, and those between tsunamis and storms, respectively.

4-6. Sedimentary Environment Changes Inferred from Nannofossil Assemblages

The high appearances of *Coccoliths* in event deposits support the hypothesis that the sand deposits originated from the ocean. *Coccoliths* and diatoms inhabiting the inner bay, seaweed beds, and river were also detected in silt, indicating that the ordinary sedimentary environment is usually a mudflat mixed with seawater and freshwater by each tide.

The sedimentary environment inferred from diatoms and *Coccolith* assemblages at a depth of 200-220 cm (diatom zone I) in the core A02 is an inner bay connected to the ocean with a narrow channel. At 190-200 cm depth (between diatom zones I and IIa), the appearances of *Coccoliths*, marine, and brackish diatoms are abundant without event deposits, suggesting that inflow of the seawater temporarily increased between the EV4 and EV5 units. Since a relative sea-level change around the beginning of the first century is not globally recognized, it is considered that the relative sea-level rise is a local event. The sedimentary environment gradually changed from marine-brackish to brackish at 165-190 cm depth (diatom zone IIa) in the core A02, because the species inhabiting mudflats in brackish water (*Melosira* sp. n) are more abundant towards the top while the *Coccoliths* decrease upwards. The finding is also consistent with the conclusion that the change in the number of appearances is gradual due to relative sea-level fall.

After the deposition of the EV4 unit (diatom zones IIb), marine and marine to brackish diatoms are abundant again, showing that the environment returns back to an inner bay due to coseismic subsidence or the collapse of a sand dune. Besides, marine diatoms decrease toward the top between EV3 and EV4 units, whereas the diatoms inhabiting brackish mudflats and rivers are dominant again in the top of zone IIb (140-150 cm depth). The results may be associated with sedimentary environment changes due to a post-seismic uplift or the redevelopment of a sand dune. The sedimentary environment is

marine to brackish inner bay before and after the EV3 units (between diatom zones IIb and IIc) and diatom assemblage change is also insignificant above and below the EV3 units, supporting the theory that the EV3 unit was caused by a storm surge without coseismic subsidence. Between the EV2 and EV3 units (diatom zone IIc), the freshwater diatoms increase upwards, showing that the influx of seawater decreases with the further growth of sand dunes. After the deposition of the EV2 unit (diatom zone IIc), marine and marine-brackish diatoms are also abundant again, while the freshwater diatoms are scarce. Since the diatoms inhabiting inner bay and seaweed beds decrease upwards and the species inhabiting brackish mudflats increase toward the top of diatom zone IIc, the results can also be explained by the collapse and growth of a sand dune caused by a tsunami or coseismic/postseismic crustal deformation with an earthquake.

In diatom zone III (30-35 cm depth in the core A02), marine and marine-brackish diatoms are rare, whereas the freshwater diatoms are abundant. This suggests that the sedimentary environment changes from brackish mudflats to a lagoon by artificially closing the mouth of the bay for the purpose of land reclamation. This result is also consistent with old topographic maps drawn from the 1800s.

4-7. Comparison with Historical Earthquakes

The age of the EV2 unit (AD 800-1310) may correspond to the AD 869 Jogan Tohoku tsunami. However, no tsunami deposits corresponding to the 1454 Kyotoku or 1611 Keicho Tohoku tsunami were identified (Fig. 4-10, 4-11, and 4-16; Sawai *et al.*, 2012; Namegaya and Yata, 2014; Sawai *et al.*, 2015). Because of the indefinable boundary between inner bay silt and agricultural soils, the implication of this is that these tsunamis did not reach the coast of Fukushima Prefecture or that they were not strong enough to transport sand to the study site.

The EV4, EV6, and EV7 units correspond to paleo-tsunami events between the second and fourth centuries AD, between the sixth and fourth centuries BC, and between the twelfth and ninth centuries BC, respectively (Fig. 4-17). These time intervals are consistent with the results of previous studies along the Pacific coast of the southern Miyagi and Fukushima Prefectures (e.g., Oikawa *et al.*, 2011; Sawai *et al.*, 2012; Takada *et al.*, 2016), although those studies did not identify event deposits corresponding to the EV3 and EV5 units. The possible paleo-storm deposits (EV3 and EV5 unit) were identified only just above the tsunami events (EV4 and EV6 units) in the study area used for this thesis. Large tsunamis might have collapsed a sand dune and as a result the lagoon or mudflat was more susceptible to storm impacts before redevelopment of the dune.

Whereas the time intervals between all event deposits have both, long (510-900 years) and short (<230 years) periods, the time intervals between paleo-tsunami deposits were all long (Fig. 4-17). The recurrence intervals for EV1-EV2, EV2-EV4, EV4-EV6, and EV6-EV7 were 780-1230, 390-890, 670-850, and 410-820 years, respectively. The average time interval ranged from 560 to 950 years. These intervals are also consistent with the findings of previous studies in southern Miyagi and Fukushima Prefectures (Fig. 4-18; Minoura and Nakaya, 1991; Sawai *et al.*, 2007, 2008, 2012, 2015; Shishikura *et al.*, 2007; The Headquarters for Earthquake Research Promotion, 2010; Oikawa *et al.*, 2011).

Tsunami deposits in the study area were distributed over an area 2 km inland from the current shoreline, revealing that the inundation area of the paleo-tsunamis is equivalent to that of the 2011 Tohoku tsunami. Prehistorical tsunami data were not considered in the tsunami risk assessment of Fukushima Daiichi NPS prior to the 2011 Tohoku-Oki earthquake (Tokyo Electric Power Company, 2012), but if this research had been carried out before the earthquake occurs, the design tsunami heights could have been sufficiently updated. Furthermore, the 2011 Fukushima accident could also have been prevented if

the emergency diesel generator was moved to a higher location according to the updated tsunami assessment.

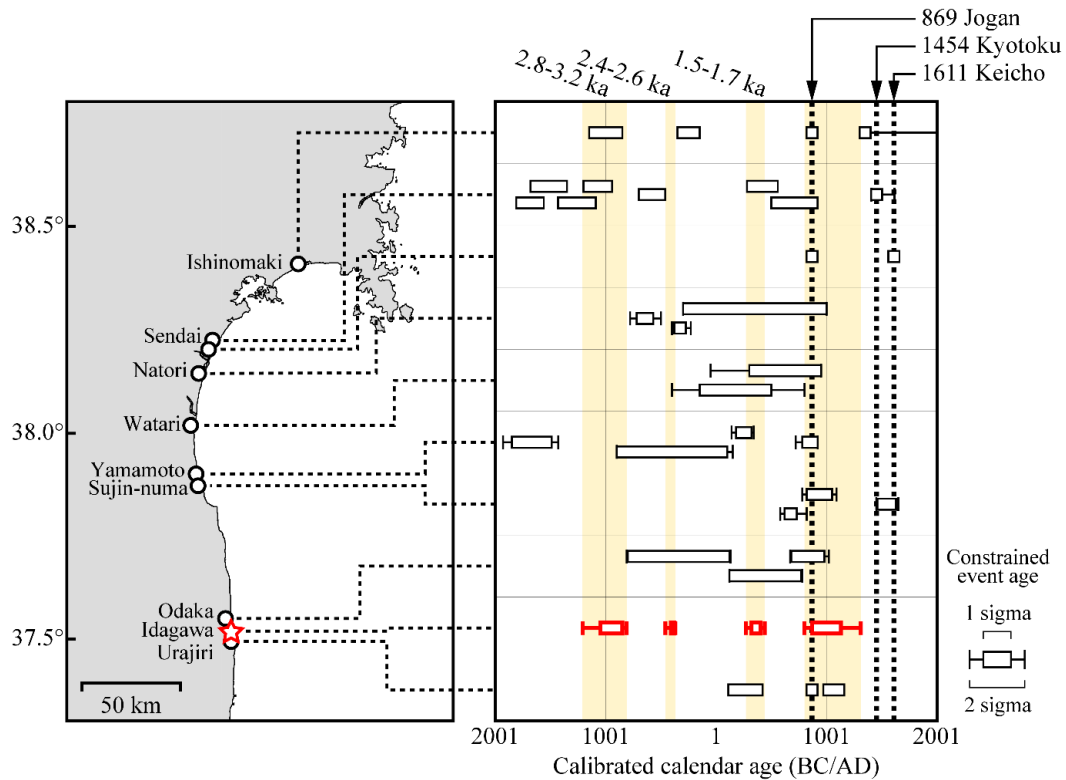


Figure 4-18. Summary of reported tsunami deposits and historical earthquakes in northern Fukushima and southern Miyagi Prefectures (Minoura and Nakaya, 1991; Sawai *et al.*, 2007, 2008, 2012, 2015; Shishikura *et al.*, 2007; The Headquarters for Earthquake Research Promotion, 2010; Oikawa *et al.*, 2011). The circles and star indicate previous sites and the current study site, respectively.

CHAPTER 5. Numerical Modeling of Tsunami Inundation and Sediment Transport for the 2011 Tohoku Tsunami

5-1. Tsunami Inundation

The distributions of the maximum height of the 2011 Tohoku tsunami were calculated from each source model (Fig. 5-1). A high tsunami (>8 m) calculated from Model 1 reached a wide area of the coast between Fukushima and Iwate Prefectures. The tsunami height of Model 2 was nearly 3 m lower than that for Model 1 and the difference was remarkable in the northern part of Iwate Prefecture. The maximum tsunami height of Model 3 was much lower than those of Models 1 and 2, whereas higher tsunamis were generated from Models 4 and 5. Large tsunamis concentrated on the coast of the southern Miyagi and Fukushima Prefectures from Model 6 and 7 because these models had a very large slip in the offshore Fukushima Prefecture. High tsunamis generated by Models 8 and 9 were limited to Sendai Bay and gradually decreased to the north and south. The tsunami waveforms simulated from Model 9 were characterized by shorter period waves compared to other models. A high tsunami of Model 9 was also limited to the southern Iwate Prefecture, whereas a high tsunami generated by Model 10 reached Miyagi and the northern Fukushima Prefectures. There was no significant difference in the tsunami heights simulated from Models 10 and 11 reaching in the nearshore Fukushima Prefecture. The tsunamis computed from previously estimated models of the 869 Jogan earthquake (Models 12 and 13) were the highest in the southern part of Miyagi Prefecture and the northern part of Fukushima Prefecture, but small tsunamis (<1 m) reached Iwate Prefecture.

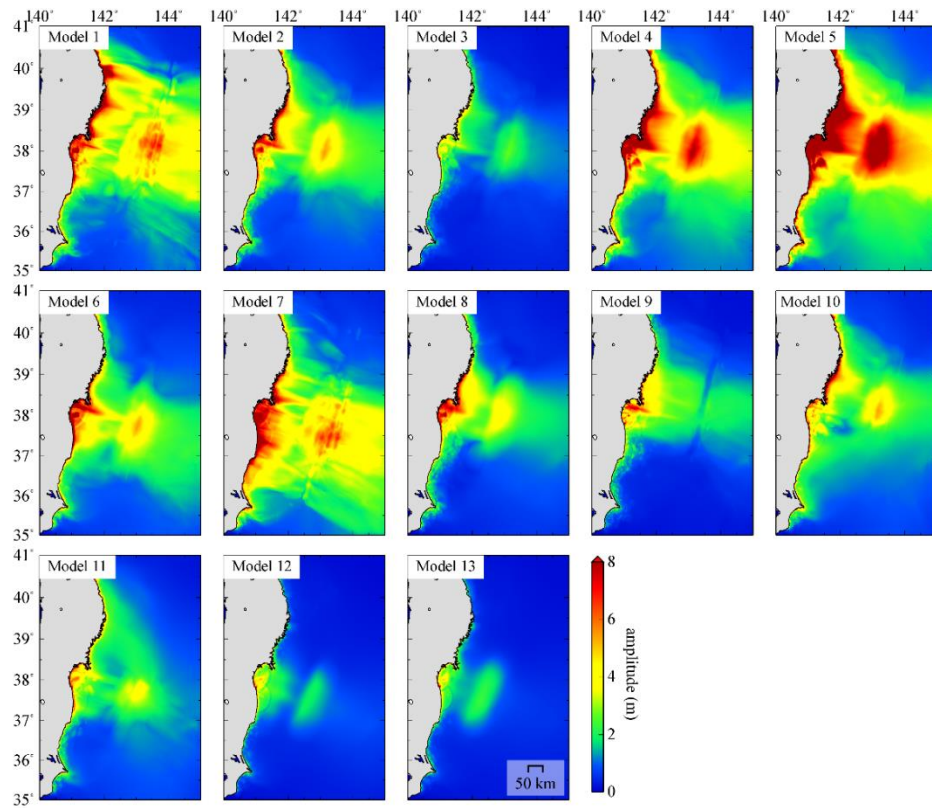


Figure 5-1. Maximum sea surface displacements for each model.

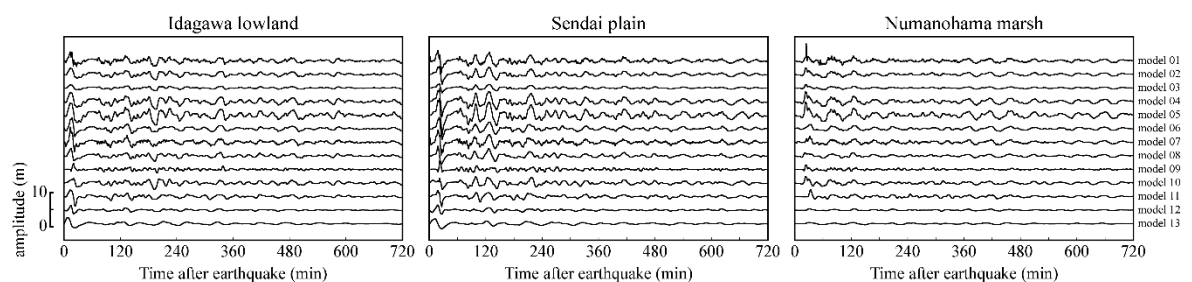


Figure 5-2. The calculated tsunami waveforms of each model incident from the offshore boundary of the computational domain in the Idagawa lowland, Sendai plain, and Numanohama marsh.

Figure 5-2 shows the incident tsunami waveforms calculated from each model at the offshore boundary of the computational domain in the sediment transport modeling. The simulated maximum tsunamis were nearly ~6.0 m high at a depth of 500 m offshore of

the Idagawa lowland. The heights increased to ~13.3 m across the shore, and suddenly decreased at the rear of the existing coastal dike and forest (Fig. 5-3). The tsunami height was nearly constant over the range 0.2 to 2.5 km from the beach. Between 2.5 and 4.5 km from the coast, it slightly increased with tsunami run-up. The tsunamis from Models 3, 9, and 11 inundated up to about 2.1-2.2 km and 3.2 km from the coast and were much shorter than the observed inundation limit. The tsunami inundations calculated from the other models roughly matched the observations, but the tsunamis calculated from Models 4 and 5 inundated much farther than the observations. Thus, Models 3, 4, 5, 9, and 11 are not appropriate for the comparison of inundation distance. The same comparison was also made for the areas of tsunami inundation (Fig. 5-4). The computed inundation areas of Models 1, 2, 4, 6, 7, 8, 9, 10, and 11 were about 100-120 % of the observations, but those of Models 3 and 5 were 66 % and 127 %, respectively (Table 5-1).

Table 5-1. The 2011 tsunami inundation heights and inundation areas computed from each model in the Idagawa lowland.

Models	K	κ	Inundation area (m ²)	Ratio to the observation
1	0.90	1.96	12,500,000	111%
2	1.13	1.96	11,850,800	105%
3	5.98	1.62	7,447,700	66%
4	0.70	2.02	13,486,000	119%
5	0.53	1.98	14,364,700	127%
6	0.83	1.84	12,782,900	113%
7	0.63	1.83	13,623,900	120%
8	1.31	1.93	11,364,000	100%
9	2.60	1.65	9,139,300	81%
10	1.17	1.78	11,489,500	102%
11	1.63	1.81	10,745,100	95%
obs.			11,311,700	

Footnote: The K and κ values are a statistical comparison of the computed and observed tsunami inundation heights.

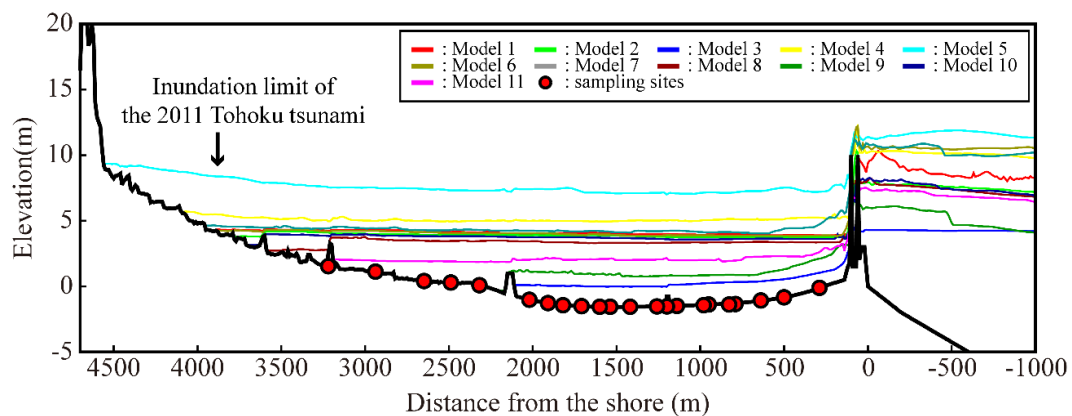


Figure 5-3. Topographic profile and maximum water surface for each model along transect in the Idagawa lowland. The sampling sites of the 2011 Tohoku tsunami deposits are also represented by the red circles (Oota *et al.*, 2017; Kusumoto *et al.*, 2018).

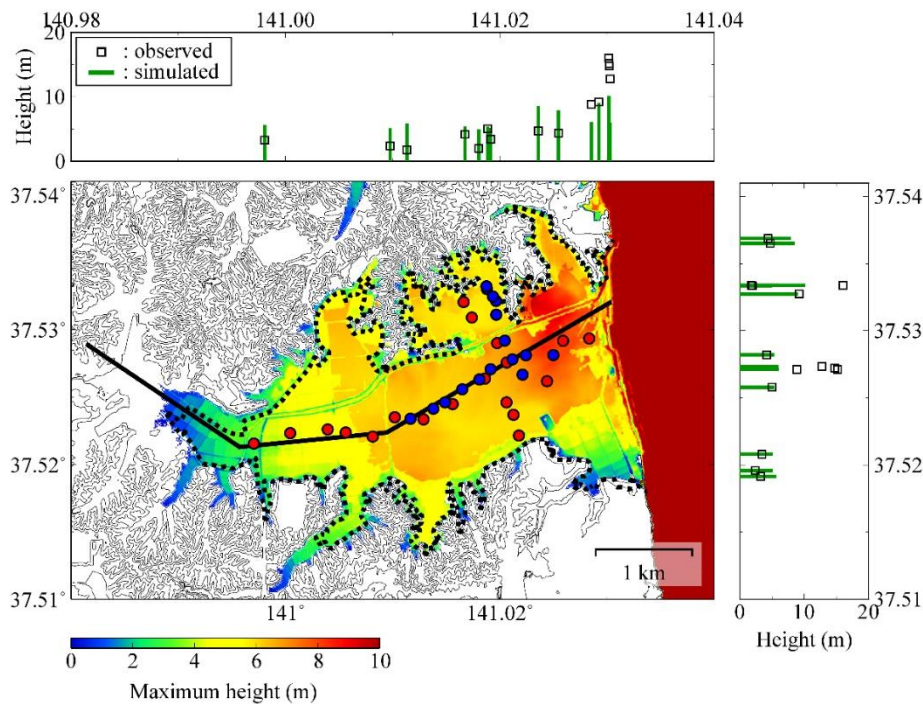


Figure 5-4. Maximum flow depth computed from Model 1 and distributions of tsunami deposits in the Idagawa lowland. The red and blue circles are the sampling locations where only the 2011 Tohoku deposits were detected, and sampling locations where both the 2011 Tohoku and 869 Jogan tsunami deposits were detected, respectively. The green bars and black squares show the simulated and observed 2011 tsunami inundation heights.

The computed maximum tsunami heights at a depth of 500 m offshore of the Sendai plain were ~7.6 m and gradually increased to ~15.6 m near the coastline. They decreased abruptly in the coastal pine forest extending between about 100 and 400 m from the shore and further decreased in the second narrow coastal forest at 810-850 m from the coast (Fig. 5-5). It was nearly constant or slightly decreased between 0.9 and 4.7 km from the beach. The tsunamis simulated from Models 3, 9, and 11 inundated up to about 2.3 to 2.4 km and 4.5 km, and the inundation distances were significantly shorter than the observations. Conversely, the inundation distance calculated from the other models were similar to the observations. Excepting Models 3, 4, 5, and 7, the areas of inundation also

ranged from 89 to 113% of the observations (Fig. 5-6 and Table 5-2). For calculations using the topographic data without the coastal pine forest, the tsunamis reached farther inland than the results of the topographic data with a coastal forest.

Table 5-2. The 2011 tsunami inundation heights and inundation areas computed from each model in the Sendai plain.

Models	<i>K</i>	<i>kappa</i>	Inundation area (m ²)	Ratio to the observation
1	0.56	2.36	48,799,600	113%
2	0.64	2.33	46,227,900	107%
3	1.65	2.07	22,855,100	53%
4	0.42	2.38	54,401,400	126%
5	0.30	2.36	57,213,000	133%
6	0.56	2.40	48,836,600	113%
7	0.50	2.41	51,952,800	121%
8	0.66	2.30	45,566,400	106%
9	1.17	2.04	36,485,000	85%
10	0.98	2.43	38,159,300	89%
11	0.87	2.51	40,469,400	94%
obs.			43,068,600	

Footnote: The *K* and κ values are a statistical comparison of the computed and observed tsunami inundation heights.

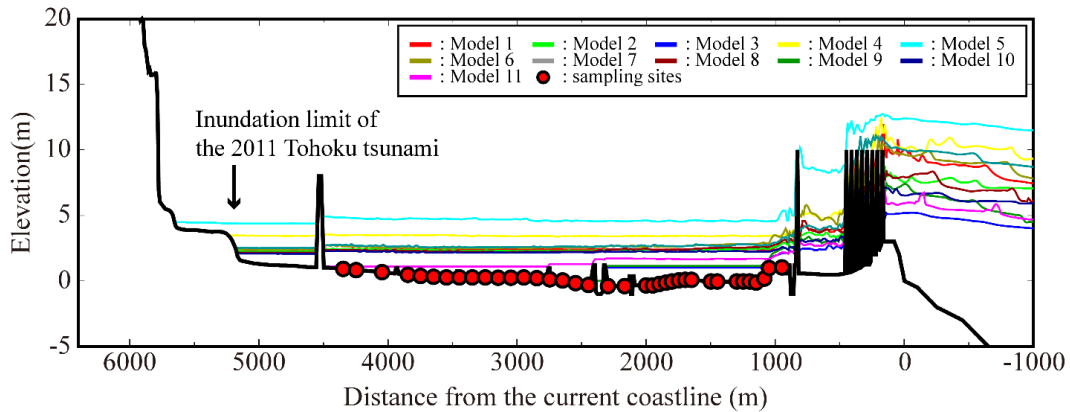


Figure 5-5. Topographic profile and maximum water surface for each model along transect in the Sendai plain. The sampling sites of the 2011 Tohoku tsunami deposits are also shown by red circles (e.g., Richmond *et al.*, 2012; Szczuciński *et al.*, 2012).

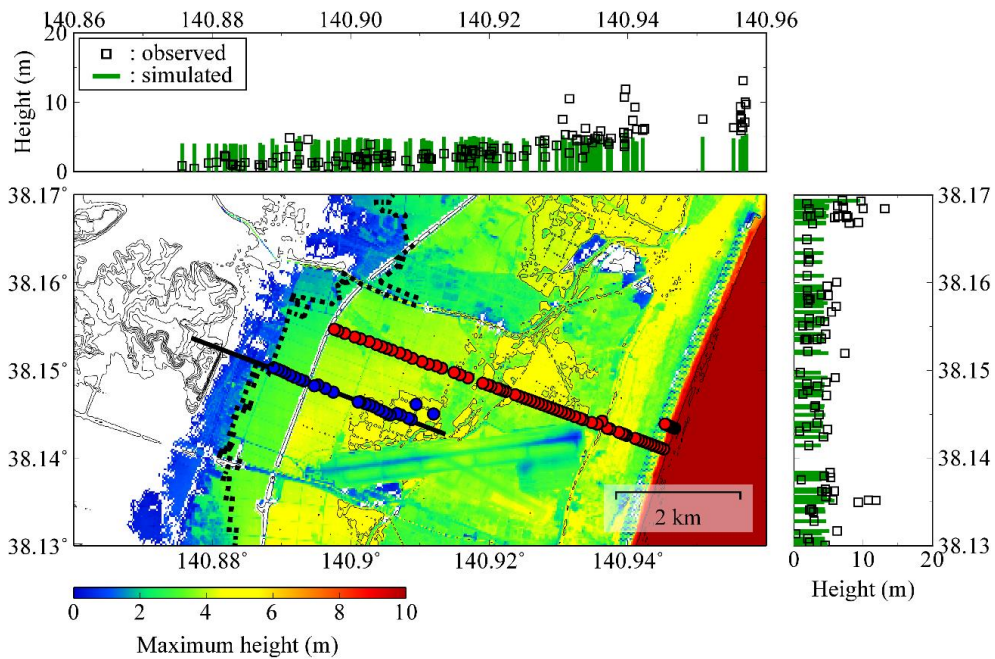


Figure 5-6. Maximum flow depth computed from Model 1 and distributions of tsunami deposits in the Sendai plain. The red and blue circles are the sampling locations where only the 2011 Tohoku deposits were detected, and sampling locations where both the 2011 Tohoku and 869 Jogan tsunami deposits were detected, respectively. The green bars and black squares show the simulated and observed 2011 tsunami inundation heights.

The maximum tsunami heights at a depth of 500 m offshore of the Numanohama marsh were ~7.8 m and rapidly increased to ~14.9 m across the coastline. The tsunami heights suddenly ran up to an altitude of about 20 to 25 m (Fig. 5-7). By comparing with the calculation results, Models 1, 2, 4, 5, and 10 could reproduce both the observed tsunami inundation distance and inundation area (81-98 % of the observations). Conversely, the agreements of Models 3, 6, 7, 8, 9, and 11 were less than 80% (Fig. 5-8 and Table 5-3).

Summarizing the above results, it appears that Models 3, 9, and 11 are not appropriate as an initial source of the 2011 Tohoku tsunami from the comparison of the maximum extent of tsunami deposit with tsunami inundation distance (Table 5-4). Additionally, Models 1, 2, and 10 are suitable as initial source models from the tsunami heights, inundation distance, and the ratio of the observed and calculated inundation area.

Table 5-3. The 2011 tsunami inundation heights and inundation areas computed from each model in the Numanohama marsh.

Models	K	κ	Inundation area (m ²)	Ratio to the observation
1	1.27	1.17	4,601,500	99%
2	-	-	3,763,400	81%
3	-	-	3,216,300	69%
4	1.65	1.29	4,206,700	90%
5	1.29	1.19	4,568,200	98%
6	-	-	3,139,800	67%
7	-	-	3,653,500	78%
8	-	-	3,144,100	68%
9	-	-	3,532,900	76%
10	-	-	3,770,300	81%
11	-	-	3,637,100	78%
obs.			4,657,300	

Footnote: The K and κ values are a statistical comparison of the computed and observed tsunami inundation heights.

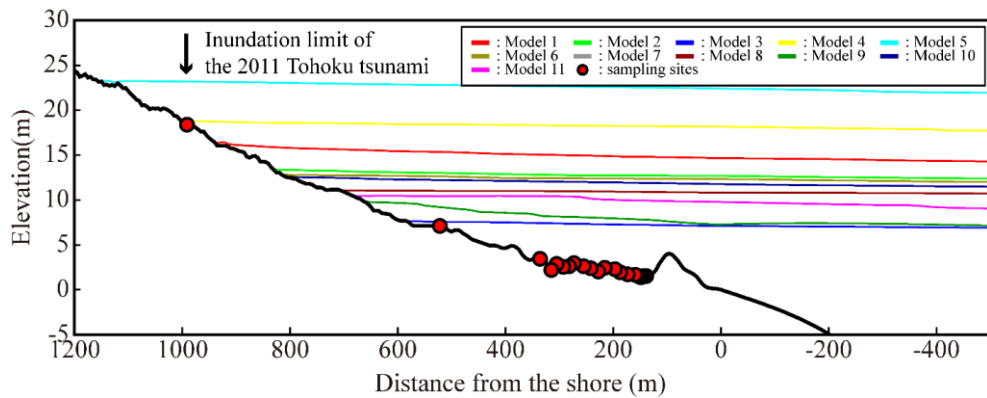


Figure 5-7. Topographic profile and maximum water surface for each model along transect in the Numanohama marsh. The distributions of the 2011 Tohoku tsunami deposits are also shown by red circles (Goto *et al.*, 2015; 2017; 2019).

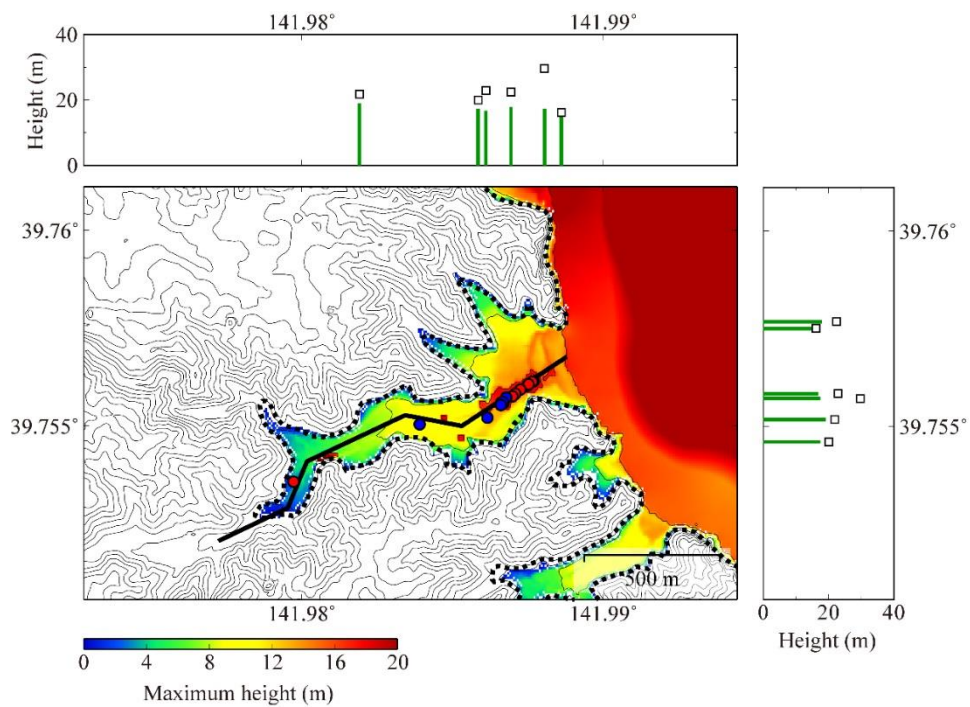


Figure 5-8. Maximum flow depth computed from Model 1 and distributions of tsunami deposits in the Numanohama marsh. The red and blue circles are the sampling locations where only the 2011 Tohoku deposits were detected, and sampling locations where both the 2011 Tohoku and 869 Jogan tsunami deposits were detected, respectively. The green bars and black squares show the simulated and observed 2011 tsunami heights.

Table. 5-4. Comparison of the simulated tsunami heights, inundation distance, and inundation area with the observations of the 2011 Tohoku tsunami deposits in the Idagawa lowland, Sendai plain, and Numanohama marsh.

Models	Idagawa			Sendai			Numanohama		
	height	distance	area	height	distance	area	height	distance	area
1	⊙	○	○	×	○	○	○	○	○
2	⊙	○	○	○	○	○	—	○	○
3	×	×	×	×	×	×	—	○	×
4	○	×	○	×	○	×	×	⊙	○
5	×	×	×	×	○	×	○	⊙	○
6	⊙	○	○	×	○	○	—	○	×
7	○	○	○	×	○	×	—	○	×
8	○	○	○	○	○	○	—	○	×
9	×	×	○	⊙	×	○	—	○	×
10	⊙	○	○	⊙	○	○	—	○	○
11	×	×	○	⊙	×	○	—	○	×

Footnote: The double circles, circles, and crosses indicate good agreement, rough agreement, and no agreement with the observations, respectively.

5-2. Erosion and Deposition

The topographic changes of the Idagawa lowland 12 hours after the earthquake were characterized by weak erosion of the lowland and thick deposition of the shallow seafloor. The total amounts of net erosion and net deposition were 4,090 m³ and 3,220 m³ for Model 1, respectively. The total net deposition on land was about 840 m³, which was equivalent to about 26 % of the total volume (Table 5-5). Significant erosion was caused by the scouring of tsunami behind non-erosional structures (e.g., coastal levees, ridges, and transverse roads). Weak erosion of up to 5 cm was calculated in the lowland between

300 and 2100 m from the shore, but the total net erosion on land was only 3 % (120 m³) of the total volume. The finding showed that the 2011 Tohoku tsunami deposit of the Idagawa lowland mostly originated from seafloor sand.

In the Sendai plain, the total net deposition was 4,550 m³ for Model 1 and among them, the amount of the deposition on land was about 30 % (1,370 m³) of the total volume (Table 5-5). Particularly, a thick sand deposit was confirmed within and behind a coastal forest (between 60-700 m from the beach). This is because the speed of the tsunami significantly decreased when passing through the pine forest, hence the sand contained in the seawater was deposited in the forest. For calculation using the topographic data without a coastal forest, the total amount of sand deposition on land was lower than that with the forest. More sand was carried throughout the plain instead of having thick sediments around the forest.

In the Numanohama marsh, the total net deposition was about 2,680 m³ calculated from Model 1 (Table 5-5). The total net deposition on land was about 1,390 m³, which was equivalent to 52 % of the total volume. Additionally, the amount of net erosion on land (54 % of the total volume) was almost equivalent to the amount of that on the seafloor. The results showed that the 2011 Tohoku tsunami deposit of the Numanohama marsh consisted of terrestrial and seafloor sand. The 2011 tsunami deposit contains the many sand and gravels originated from the beach, riverbed, and slope (Goto *et al.*, 2017), which is consistent with the observations.

Table 5-5. Total net deposition and erosion for Model 1.

Study sites	Erosion (m ³)			Deposition (m ³)			D_T/E_T
	E_S	E_L	E_T	D_S	D_L	D_T	
Idagawa	3970	120	4090	2380	840	3220	0.79
Sendai	4270	80	4350	3180	1370	4550	1.05
Numanohama	550	640	1190	1290	1390	2680	2.25

Footnote: E_S , E_L , and E_T are total volumes of net erosion on seafloor, land and entire computational domain, respectively. D_S , D_L , and D_T are total volumes of net deposition on seafloor, land and entire computation domain, respectively.

5-3. Sediment Thickness

The model validity, sensitivity, and accuracy of the sediment transport simulation was evaluated by comparing the simulated sediment thickness with the observations of the 2011 Tohoku tsunami deposits at the Idagawa lowland, Sendai plain, and Numanohama marsh. The K and κ values for eleven scenarios are shown in Tables 5-6, 5-7, and 5-8.

In the Idagawa lowland, the observed sediment thicknesses at a total of 22 sampling locations between 285 and 3230 m from the shore obtained from the geological survey by Oota *et al.* (2017) and Kusumoto *et al.* (2018) were compared with the simulation results. The thickness of sediment with a single grain size were much thinner than the observations (Fig. 5-9 and Table 5-6). However, the K values for the simulated tsunami deposit for Models 1 and 2 were 1.00 and 1.01 by considering multiple grain sizes proposed in this study. Hence it is evident that these models are very suitable as an initial tsunami source. The computed sediment thickness of Model 8 was also in good agreement with the observations ($K = 1.19$), meanwhile the other models underpredicted or overpredicted (Fig. 5-10 and Table 5-6).

Table 5-6. Statistical comparison of the observed and computed sediment thickness in the Idagawa lowland.

Models	single grain size with coastal forest		multiple grain sizes with coastal forest		multiple grain sizes without coastal forest	
	K	κ	K	κ	K	κ
1	4.13	4.26	1.00	2.15	0.53	2.41
2	3.98	3.91	1.01	2.23	0.64	2.45
3	9.59	2.09	5.08	2.25	5.79	1.99
4	2.81	3.42	0.66	2.37	0.39	1.95
5	1.08	2.32	0.39	2.20	0.28	1.94
6	2.69	3.24	0.76	2.14	0.32	1.98
7	1.89	3.40	0.67	2.27	0.30	2.01
8	3.56	3.39	1.19	2.06	0.65	2.53
9	6.99	2.37	2.84	2.71	2.54	2.54
10	4.54	3.82	1.14	1.99	0.81	2.50
11	5.02	2.92	1.95	2.86	1.05	2.08

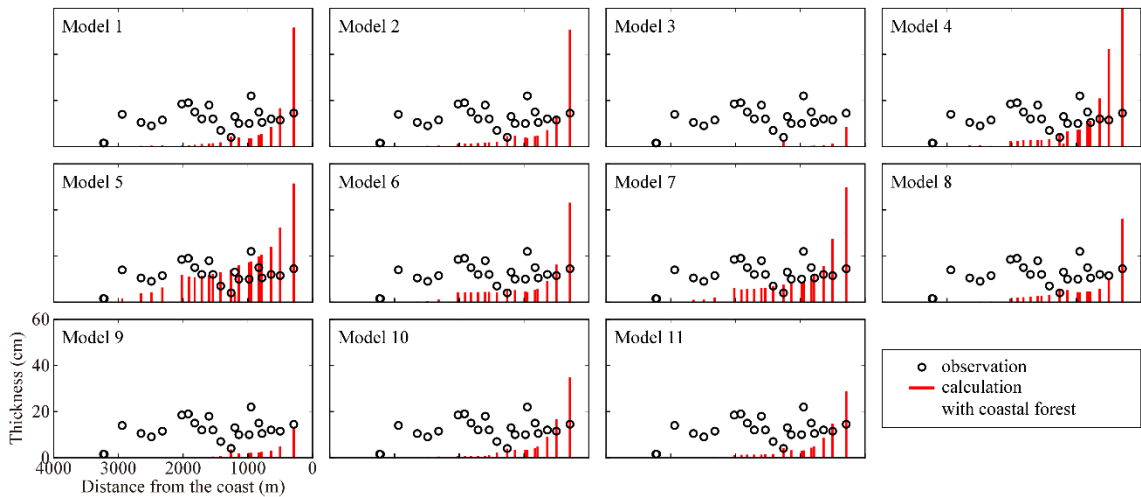


Figure 5-9. Comparison of the observed (black circles) and simulated (red bars) sediment thickness with a single grain size of the 2011 Tohoku tsunami deposits in the Idagawa lowland. The values of K and κ are shown in Table 5-6.

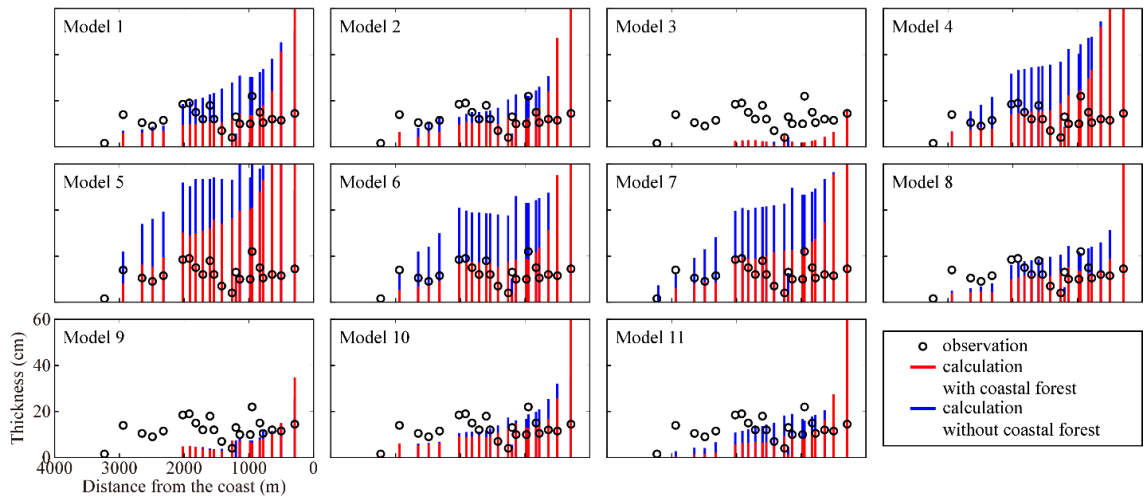


Figure 5-10. Comparison of the observed (black circles) and simulated (red and blue bars) sediment thickness with multiple grain sizes of the 2011 Tohoku tsunami deposits in the Idagawa lowland. The distance between the red and blue bars show the effects of the coastal forest. The values of K and κ are shown in Table 5-6.

In the Sendai plain, the observed sediment thickness was compared with the simulation at 37 sampling locations between 550 and 4350 m from the beach reported by Goto *et al.* (2011), Richmond *et al.* (2012), and Szczuciński *et al.* (2012). The sediment thicknesses with a single grain size were much thinner than the observations, similar to the Idagawa lowland (Fig. 5-11 and Table 5-7). By considering multiple grain sizes, the simulated thicknesses of Models 1, 2, 6, 7, and 8 for calculations using the topographic data with a coastal forest were in good agreement with the observations ($K = 0.98, 1.24, 0.98, 0.94,$ and 0.89). Models 3 and 9 underestimated the thickness because the wave height of Model 3 (<2 m) is smaller than the beach ridge, and because the inundation distance is also short due to the short wavelength of the tsunami computed from Model 9. When the topographic data without the forest were used, the simulated thicknesses of other models except Models 3, 9, and 11 were much thicker than the observations (Fig. 5-12 and Table

5-7). The findings suggest that a coastal forest greatly contributed to preventing the transport of sand inland.

Table 5-7. Statistical comparison of the observed and computed sediment thickness in the Sendai plain.

Models	single grain size with coastal forest		multiple grain sizes with coastal forest		multiple grain sizes without coastal forest	
	K	κ	K	κ	K	κ
1	1.78	4.45	0.98	3.08	0.25	3.00
2	1.79	4.44	1.24	2.90	0.34	3.00
3	3.38	3.82	2.88	3.32	1.93	2.80
4	1.57	4.95	0.77	3.08	0.18	3.16
5	0.84	3.23	0.24	3.11	0.11	3.37
6	1.69	4.39	0.98	2.79	0.26	2.90
7	1.75	4.30	0.94	2.81	0.23	2.94
8	1.74	4.12	0.89	3.41	0.38	2.84
9	2.69	3.47	2.51	3.12	1.58	2.67
10	2.01	4.42	1.41	2.58	0.41	3.25
11	2.55	4.02	1.86	2.71	1.12	2.59

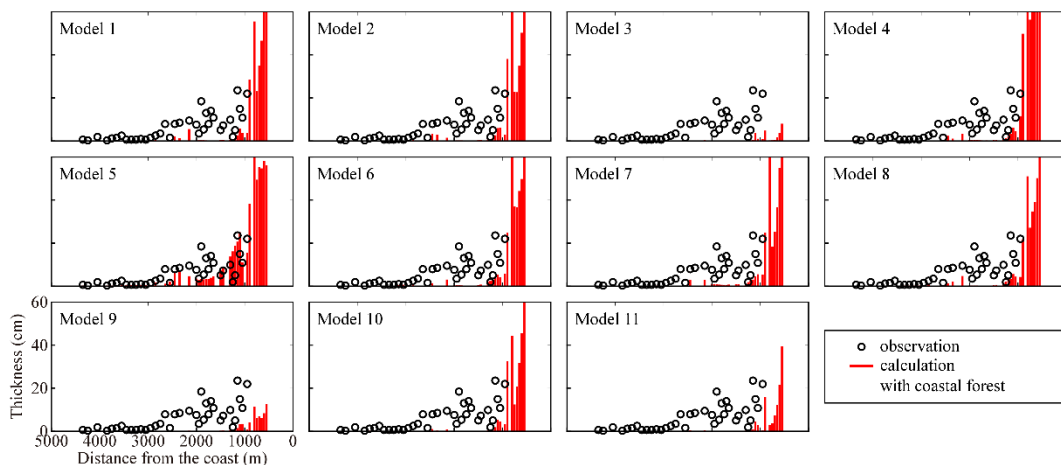


Figure 5-11. Comparison of the observed (black circles) and simulated (red and blue bars) sediment thickness with a single grain size of the 2011 Tohoku tsunami deposits in the Sendai plain. The values of K and κ are shown in Table 5-7.

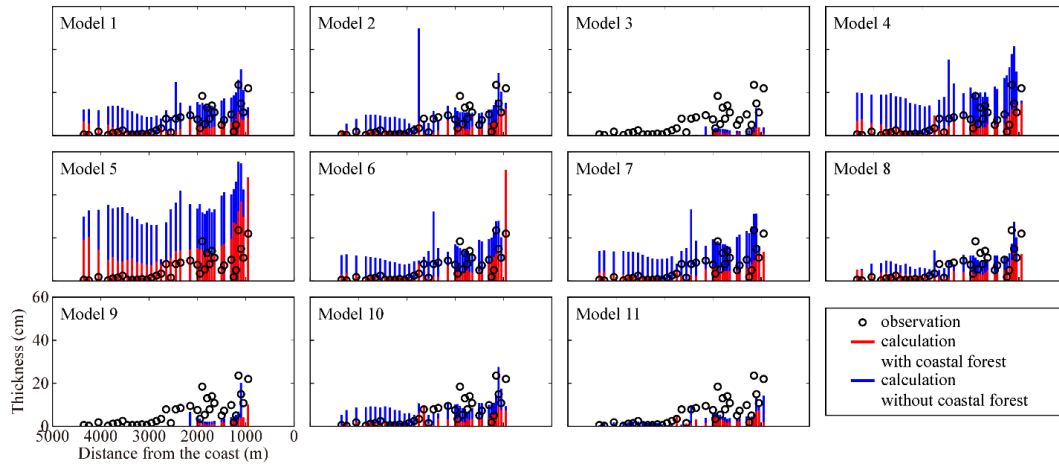


Figure 5-12. Comparison of the observed (black circles) and simulated (red and blue bars) sediment thickness with multiple grain sizes of the 2011 Tohoku tsunami deposits in the Sendai plain. The distance between the red and blue bars show the effects of coastal forest. The values of K and κ are shown in Table 5-7.

In the Numanohama marsh, the sediment thickness was observed at 20 sampling locations between 140 and 990 m from the coast collected by Goto *et al.* (2015; 2017; 2019). The sediment thickness of Models 1, 4, and 5 when calculated with a single grain size was roughly in agreement with the observations (Fig. 5-13 and Table 5-8). However, when calculated with multiple grain sizes, a much thicker sand layer (>1 m thick) than the observations was deposited in the back marsh, and hence the result was an overprediction ($K = 0.21$). The other models except Model 3 also overestimated the result (Fig. 5-14 and Table 5-8). The following two possible hypotheses are conceivable as the cause of all models producing thicker sediments than the observations; (1) The Numanohama marsh is located in a steep V-shaped valley, therefore tsunami amplification due to the two-dimensional topography and bathymetry is greater than on the lowland and alluvial plain. However, this is not reflected in the one-dimensional sediment transport modeling. (2) The 2011 Tohoku tsunami deposit of the Numanohama marsh consists

mostly of gravel-rich sand. The main target of the sediment transport modeling by Takahashi *et al.* (1999) is sand, hence it may not be suitable for this gravel-rich study area. To test the first hypothesis, the amplification of tsunami heights due to the topography and bathymetry was assessed by the two-dimensional sediment transport modeling (Fig. 5-15 and Table 5-8). Comparing the one-dimensional and two-dimensional modeling has no significant influence on the simulated thickness, suggesting that another hypothesis is required. Finally, except for the calculation with a single grain-size, the simulated results do not reproduce the observations in the Numanohama marsh. Thus, the comparison of the maximum extent of the tsunami deposit with the inundation distance is used for reexamining the tsunami source of the 869 Jogan earthquake, but the comparison between the observed and computed sediment thickness is not used.

Table 5-8. Statistical comparison of the observed and computed sediment thickness in the Numanohama marsh.

Models	single grain size with 1D modeling		multiple grain sizes with 1D modeling		multiple grain sizes with 2D modeling	
	K	κ	K	κ	K	κ
1	1.30	3.46	0.21	3.88	0.08	3.83
2	2.07	3.06	0.32	4.18	0.25	7.66
3	5.74	2.40	1.23	4.69	0.99	3.65
4	1.33	3.14	0.16	3.69	0.11	5.28
5	1.00	3.01	0.10	2.42	0.07	3.95
6	2.88	2.86	0.38	3.66	1.10	4.31
7	2.54	3.01	0.31	3.80	0.41	5.85
8	2.37	2.99	0.41	4.98	1.27	4.11
9	3.48	2.77	0.56	5.11	0.28	7.67
10	2.05	3.07	0.36	4.89	0.18	7.52
11	2.13	3.16	0.29	3.98	0.39	4.69

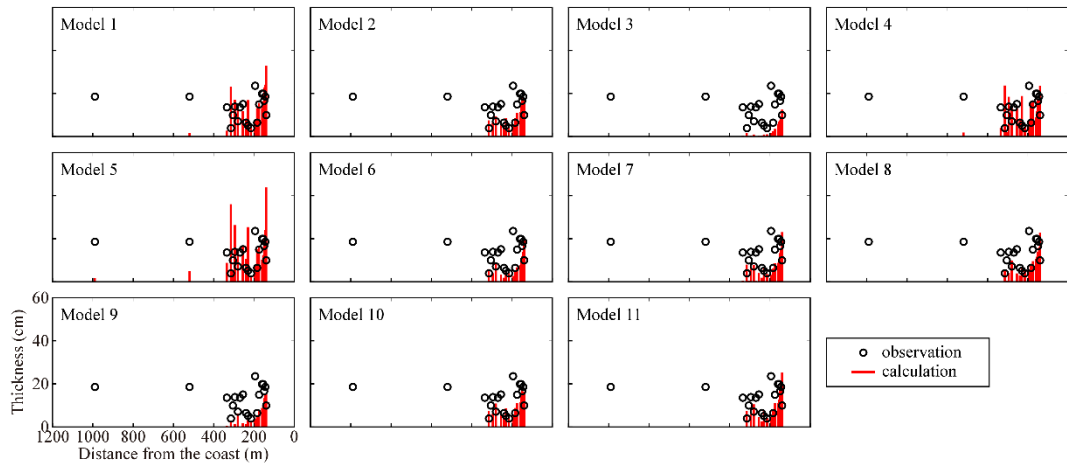


Figure 5-13. Comparison of the observed (black circles) and simulated (red bars) sediment thickness with a single grain size of the 2011 Tohoku tsunami deposits in the Numanohama marsh. The values of K and κ are shown in Table 5-8.

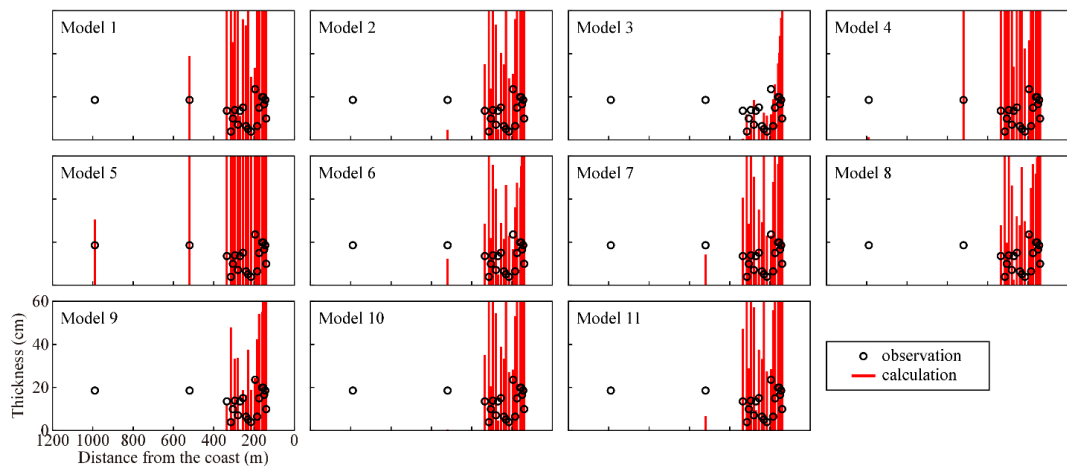


Figure 5-14. Comparison of the observed (black circles) and simulated (red bars) sediment thickness with multiple grain sizes of the 2011 Tohoku tsunami deposits in the Numanohama marsh. The values of K and κ are shown in Table 5-8.

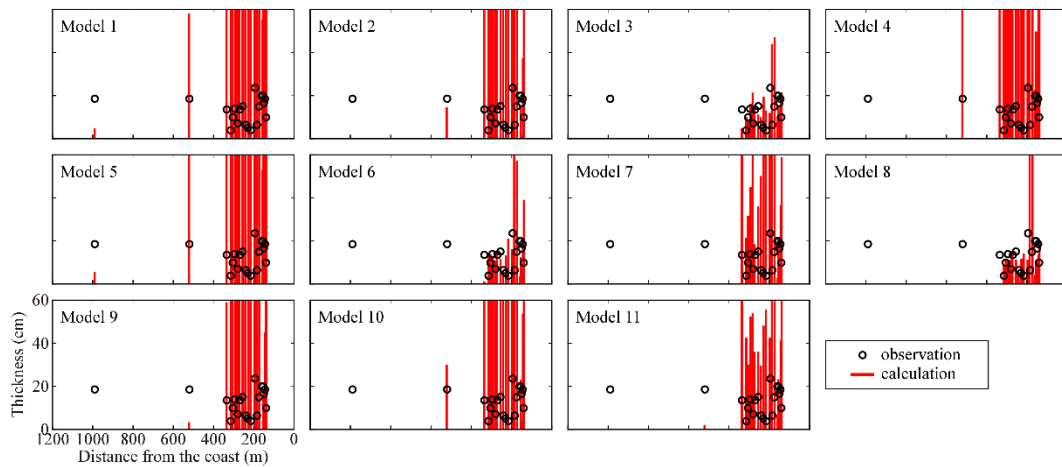


Figure 5-15. Comparison of the observed (black circles) and simulated (red bars) sediment thickness with the two-dimensional modeling of the 2011 Tohoku tsunami deposits in the Numanohama marsh. The values of K and κ are shown in Table 5-8.

5-4. Time Duration

Here, the effects of computational time duration on the sediment thickness and the K value are evaluated for each study site. For the Idagawa lowland, at least three massive sand depositions are shown in Figure 5-16. The first one is at about 1 hour after the earthquake, which corresponds to the sand deposition caused by the first and second waves of tsunami. The second one is at about 3 hours from the origin time. Hence it is considered that these are the reflected waves from the coast of Iwate and Miyagi Prefectures. The third one is at about 4 hours after the earthquake, and the amount of the deposition is about 20-30% of the final sediment thickness. At 6 hours after earthquake occurrence, 90% or more of the final results are deposited, and the K value approaches 1.0. Considering these results, it seems that a computation time of 6 hours for the sediment transport modeling is sufficient at the Idagawa lowland.

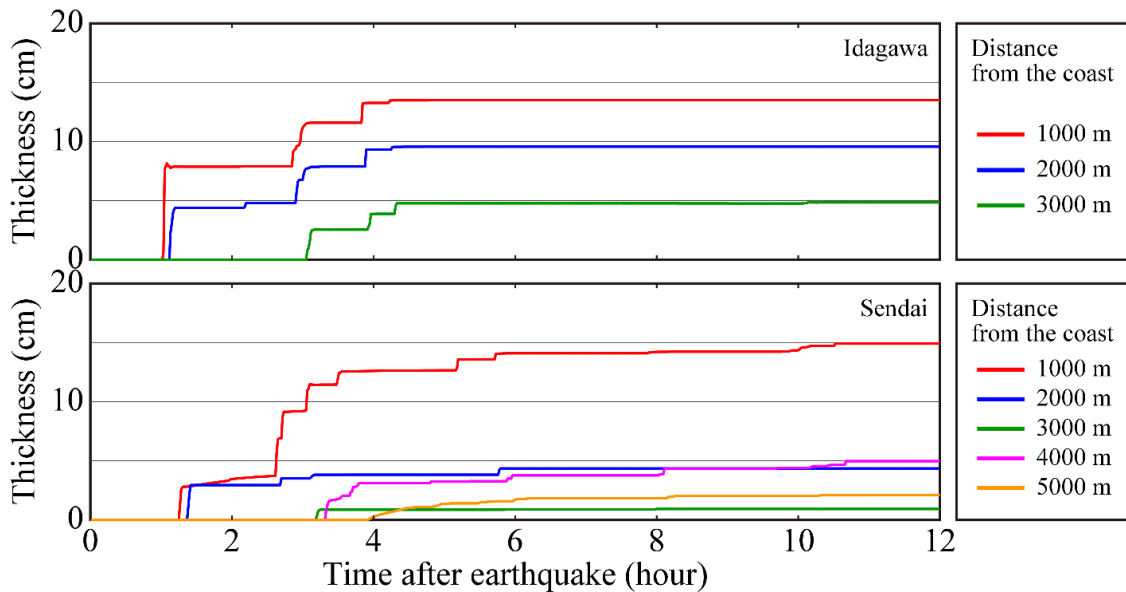


Figure 5-16. Time series of the simulated sediment thickness with distances from the coast in the Idagawa lowland and Sendai plain.

The depositional process of the 2011 Tohoku tsunami deposit in the Sendai plain can be divided into three sub-regions; the seaward side of the Hachikenbori River at about 2500 m from the beach, between Hachikenbori River and the Sendai Tobu Highway at about 4500 m from the coast, and the landward side of the Sendai Tobu Highway (Fig. 5-16). On the ocean side of the Hachikenbori River, there was a sand deposition due to the first and second waves of tsunami at about 1-2 hours after the earthquake occurred. In this region, >80% of the final results were deposited in the 4 hours after the earthquake and it is almost constant after that. Between the Hachikenbori River and Sendai Tobu Highway, the sand deposition is characterized by at least four peaks of sand deposition at about 3.5 hours, 6 hours, 8 hours, and 10.5 hours after the earthquake. Particularly, the first sand deposition accounts for roughly 20-30% of the total. On the inland side of the Sendai Tobu Highway, gradual sand deposition continued until about 10 hours from the origin time. The value of K gradually decreases with time, and converges to $K=0.98$ at

about 10 hours from when the earthquake started. From the above results, it is necessary to perform the calculations using a 10 hours periods in order to reproduce the sediment thickness of the Sendai plain. The reason for requiring a longer calculation time than the Idagawa lowland is considered to be that the tsunami inundation was blocked by roads, coastal protection, and coastal pine forests.

5-5. Water Depths at the Offshore Boundary

The maximum water depth at the boundary of the computational domain has a significant influence on the tsunami sediment transport modeling process. This is because the sediment flux transported from outside the computational domain could not be reproduced. In this section, the change in sediment thickness and the K values with varying maximum water depth (D_{max}) at the offshore boundary of the computational domain for each study site is examined. Figure 5-17 shows the change in the value of K when the maximum water depth was changed using Model 1 as the initial tsunami source. For the Idagawa lowland and Sendai plain, the computed sediment thicknesses were overpredicted ($K < 0.8$) when the maximum water depth was set at 25, 50, and 75 m. The value of K was closest to 1 when the maximum water depth was set at 500 m and it gradually increased with the water depth in the Idagawa lowland and Sendai plain. Regarding the Numanohama marsh, the results were always overestimated ($K < 0.4$) even if a waveform entered from any depth.

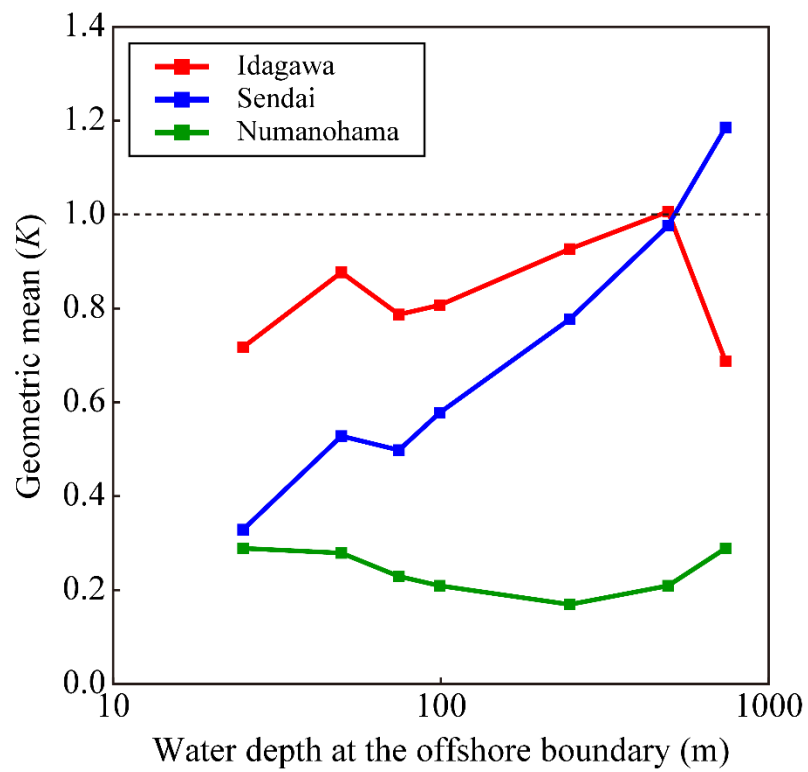


Figure 5-17. Relationship between the values of geometric mean and water depth at the offshore boundary.

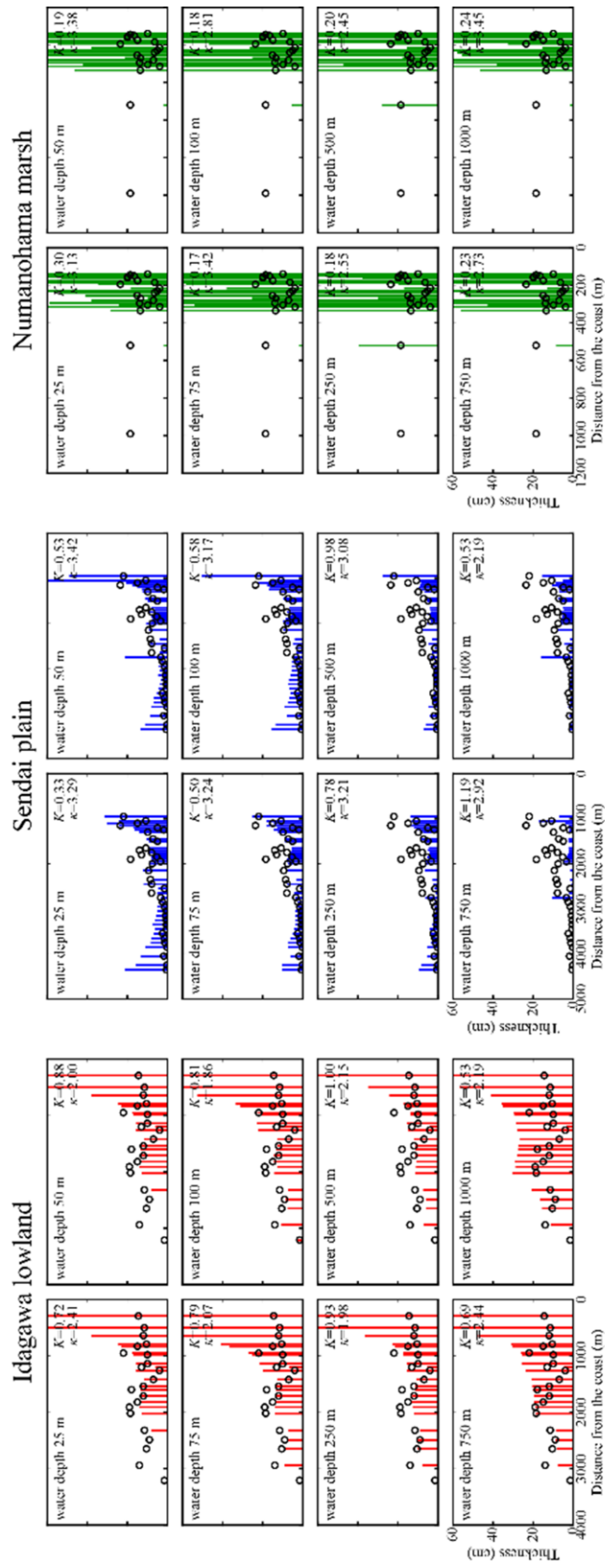


Figure 5-18. The calculated sediment thickness for different water depths (25, 50, 100, 250, 500, 750, and 1000 m) in the Idagawa lowland, Sendai plain, and Numanohama marsh.

5-6. Model Parameters –Bedload and Pick-up Rates–

The coefficients of bedload and pick-up rates of 0.167, 0.267, and 0.394 mm in diameter have been determined from tsunami hydraulic experiments by Takahashi *et al.* (2011), but the coefficients of the silt diameter have not been studied. The regression relationships of these coefficients proposed by Gusman *et al.* (2018) may not be accurate. In this section, the relationship between the total sediment thickness and the coefficients of bedload and pick-up rates in silt diameter are investigated for the Idagawa lowland (Fig. 5-19). The reference model used the values ($w_{\alpha} = 1.58 \times 10^{-4}$ and $w_{\beta} = 8.84$) estimated from Gusman *et al.* (2018) when sand particles are 0.032 mm in diameter. Figures 5-20 and 5-21 show the comparison of the calculated results with varying coefficients. The value of K ranged from 0.92 to 1.02, indicating that neither model was significantly different to the reference model ($K=1.00$). This suggests that the effect on sediment thickness by varying these coefficients is negligible. This is because most of silt was transported by the suspension and the mean concentration reached the upper limit (1%) immediately. Therefore, the estimated values by Gusman *et al.* (2018) were used as the coefficients in this study.

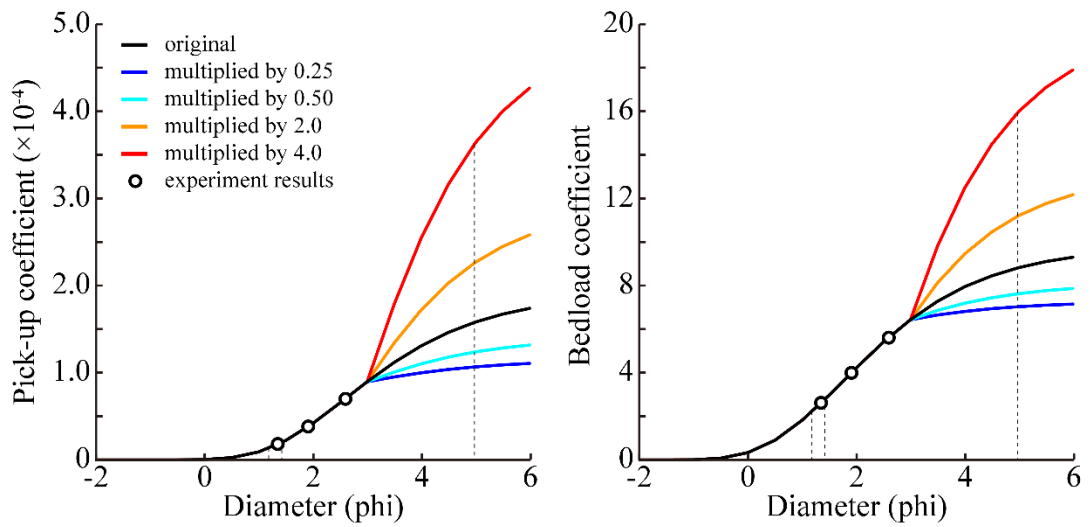


Figure 5-19. Different coefficients of bedload and pick-up rates. The circles show the experiment results (Takahashi *et al.*, 2011). The coefficients that are used in the sediment transport model are marked by the black dotted lines.

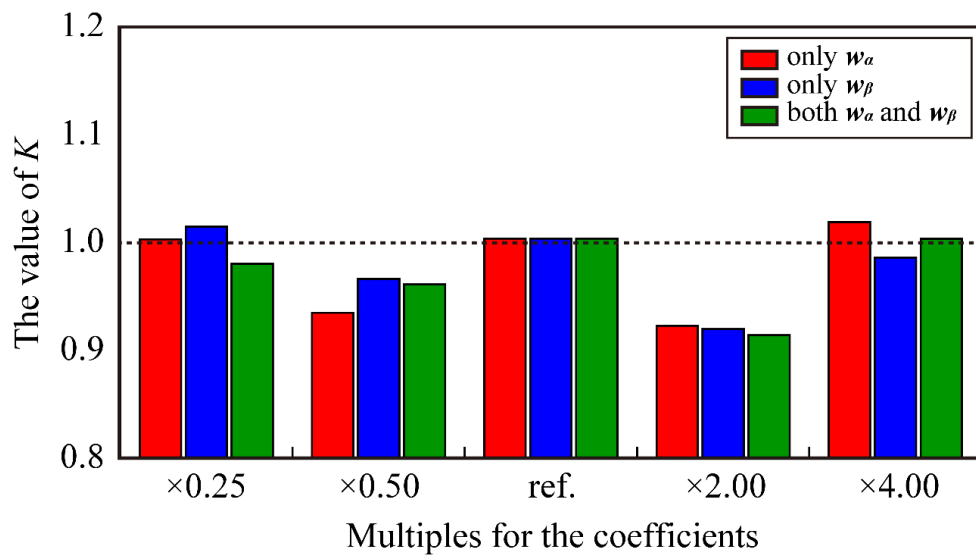


Figure 5-20. Comparison between the observed and calculated values with different coefficient of bedload and pick-up rates.

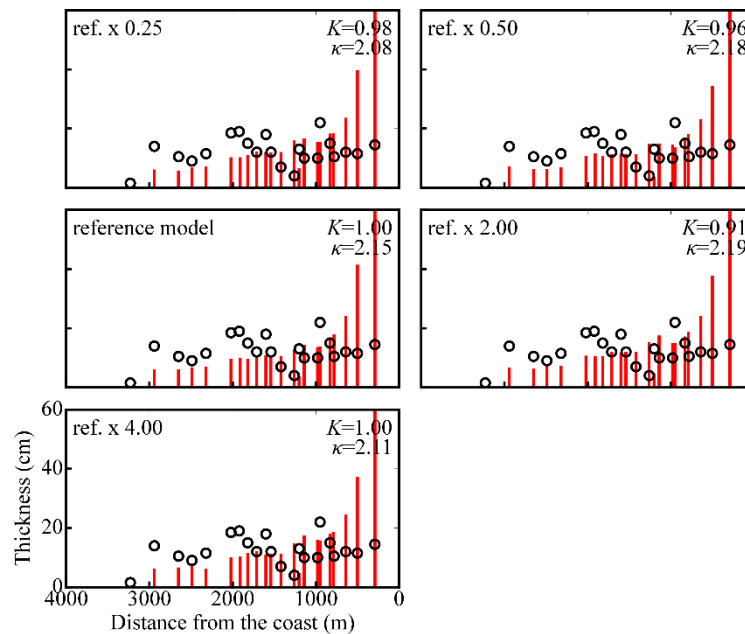


Figure 5-21. The simulated sediment thickness for different coefficients of bedload and pick-up rates. The reference model used model parameters proposed by Gusman *et al.* (2018)

5-7. Model Validity, Sensitivity, and Accuracy

Here, model validity, sensitivity, and accuracy are defined as whether the observations can be well reproduced from Model 1, whether Model 1 and the others can be distinguished by comparing the calculated and observed sediment thickness, and whether the computations and observations match, respectively.

For comparison with the observed sediment thickness, the simulation results for multiple grain sizes with a coastal forest are used (Fig. 5-22). Comparing the computed and observed sediment thicknesses, the results of Models 1 and 2 agree with the observations, suggesting that the sediment transport modeling has validity.

Next, tsunamis generated from Models 1, 2, and 8 are necessary to explain the observed

2011 Tohoku tsunami deposits in the Idagawa lowland and Sendai plain (Table 5-6 and 5-7). As noted in section 5-1, Models 1, 2, and 10 are suitable as an initial source model from the comparison between the maximum extent of tsunami deposit and inundation area in the Idagawa lowland, Sendai plain, and Numanohama marsh. Accordingly, it can be concluded that tsunamis associated with an M9-class earthquake (Models 1 and 2) are appropriate as an initial tsunami source of the 2011 Tohoku earthquake. Conversely, comparison of the observed maximum extent of the tsunami deposits with the computed inundation distance suggest that Models 3, 9, and 11 are invalid. Thus, the findings suggest that the sediment transport modeling is more effective and exhibits a higher sensitivity than the conventional method. Additionally, the results of Models 1 and 2 matched the observations, whereas the observed sediment thickness could not be reproduced by Models 6 and 7, indicating that they may also be sensitive to the location of large slip areas.

Regarding model accuracy, a detailed sand deposition cannot be reproduced. For example, excessive sand deposition occurs behind a coastal forest in the computations, but the phenomenon was not observed in the Sendai plain (e.g., Goto *et al.*, 2011; Richmond *et al.*, 2012; Szczuciński *et al.*, 2012). The reason for this is probably the microtopography and the reproducibility of the behavior of both the sand particles and a coastal forest. The former has a significant influence on sediment thickness because the sediment is selectively deposited so as to fill depressions. In this study, a mesh size of 5 or 10 m was used, but it may be necessary to reduce these values. The latter can be confirmed by comparing the results of hydraulic experiments with the calculated results (e.g., Kansai University, 2016). According to this study, the behavior of sand particles is difficult to reproduce because the deposition and erosion of the sediment due to turbulent flow is complicated. Regarding a coastal forest, the deposition and erosion should be also

calculated using the equivalent roughness coefficient model (e.g., Imai *et al.* 2013).

Additionally, this study assumed that the interaction between different grain sizes is negligible, but this may not be appropriate. Therefore, the effects of such an interaction will be investigated in future studies by comparing the results of this study with tsunami hydraulic experiments with multiple grain sizes and a non-uniform particle moveable bed model.

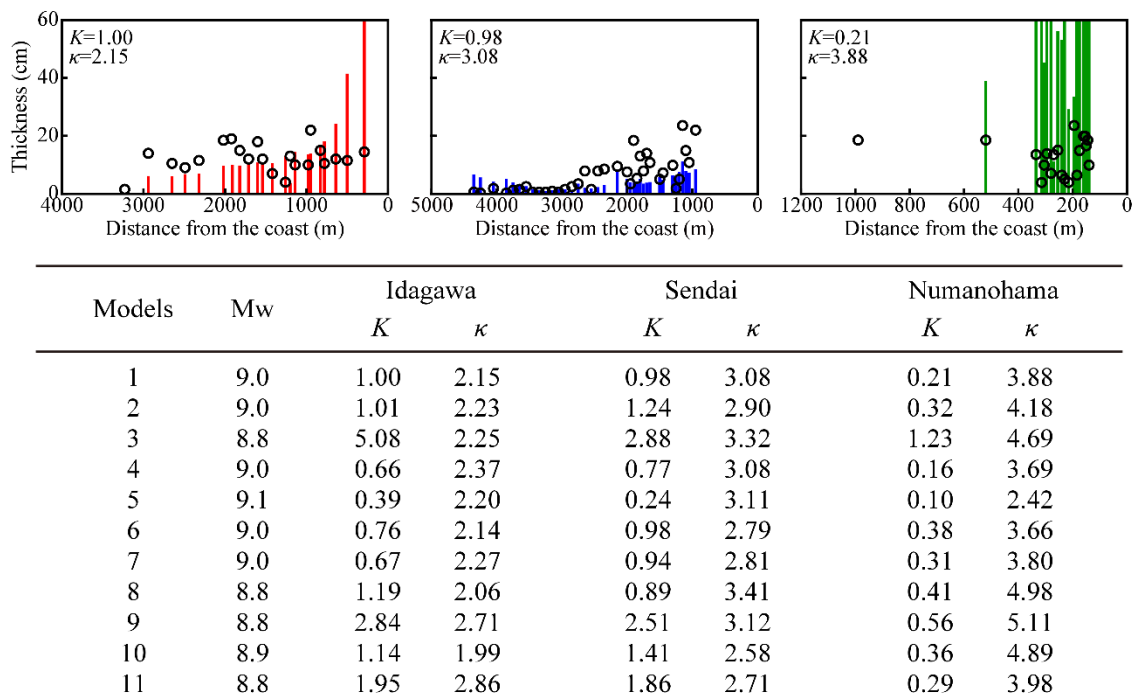


Figure 5-22. Summary of results for model validity, sensitivity, and accuracy of sediment transport modeling using the 2011 Tohoku tsunami deposits. The upper panels show the observed and simulated sediment thickness of Model 1. The lower table shows a comparison of K and κ for sediment thickness.

CHAPTER 6. Application to the 869 Jogan Tsunami Deposit

6-1. Model Uncertainties

Finally, the tsunami source model of the 869 Jogan earthquake is reexamined using paleo-tsunami deposits in the Idagawa lowland, Sendai plain, and Numanohama marsh. However, it is necessary to consider several uncertainties to apply the sediment transport modeling to historical tsunami deposits, unlike the case of the 2011 Tohoku tsunami deposit. Model parameters were adjusted to the corresponding values for grain size distribution estimated from the 869 Jogan tsunami deposit at each study site (Fig. 4-9 and Table 3-7).

The first uncertainty is the source models. Therefore, 13 source scenarios were prepared based on previous source models (Fig. 3-6 and Table 3-8). The second uncertainty is the fact that the inundation distance and area are unknown. Here, it was confirmed that the computed tsunamis for each model inundate farther inland than the most inland sampling location, as with Satake *et al.* (2008), Namegaya *et al.* (2010), and Namegaya and Satake (2014). The third uncertainty is topography. The terrain conditions in AD 869 (e.g., ground surface, land utilization, the presence/absence of coastal forest, and the altitude of beach ridge) were significantly different to the current conditions. Therefore, the ground surface is firstly determined from the base depth of the 869 tsunami deposit and the sedimentary environments inferred from diatom and nannofossil analysis, assuming that crustal deformation (uplift or subsidence) between AD 2011 and AD 869 is negligible (Fig. 6-1, 6-2, and 6-3). The sedimentary environment inferred from the sedimentary facies and historical documents was also a wetland without a coastal forest for the Sendai plain, a mudflat with/without a coastal forest for the Idagawa lowland, and a V-shaped valley for the Numanohama marsh. Regarding the beach ridge elevation, the

effects were examined by preparing multiple scenarios (T.P. -1 m, +0 m, +1 m, +2 m for the Idagawa lowland, T.P. +0 m, +0.5 m, +1 m, +2 m for the Sendai plain, and T.P. +0 m, +1 m, +2 m, +3 m for the Numanohama marsh) on the basis of current altitude.

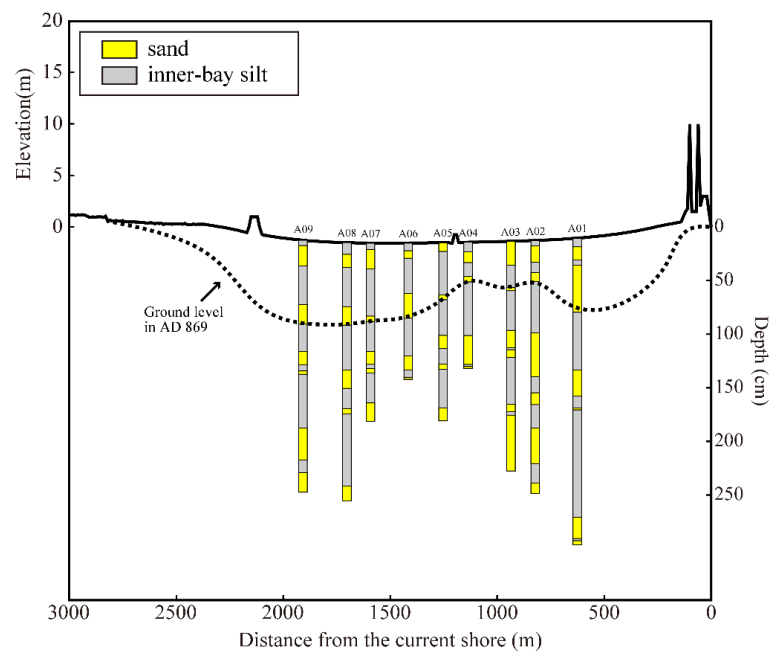


Figure 6-1. Ground surface in the Idagawa lowland in AD 869 estimated from the distribution of base depth of paleo-tsunami deposits and the sedimentary environment inferred from diatom and nannofossil analysis (Kusumoto *et al.*, 2018).

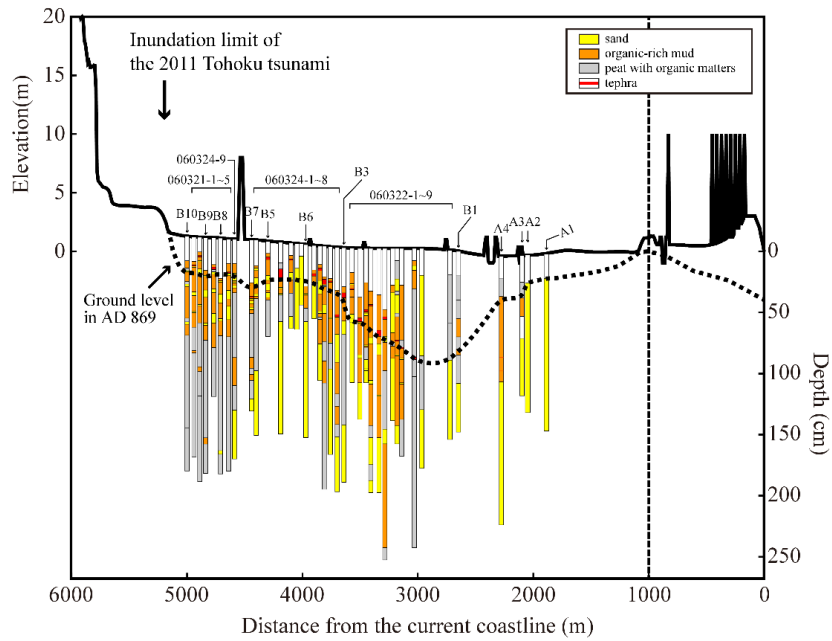


Figure 6-2. Ground surface in the Sendai plain in AD 869 inferred from the distribution of base depth of paleo-tsunami deposits and To-a tephra (Sawai *et al.*, 2007; 2008).

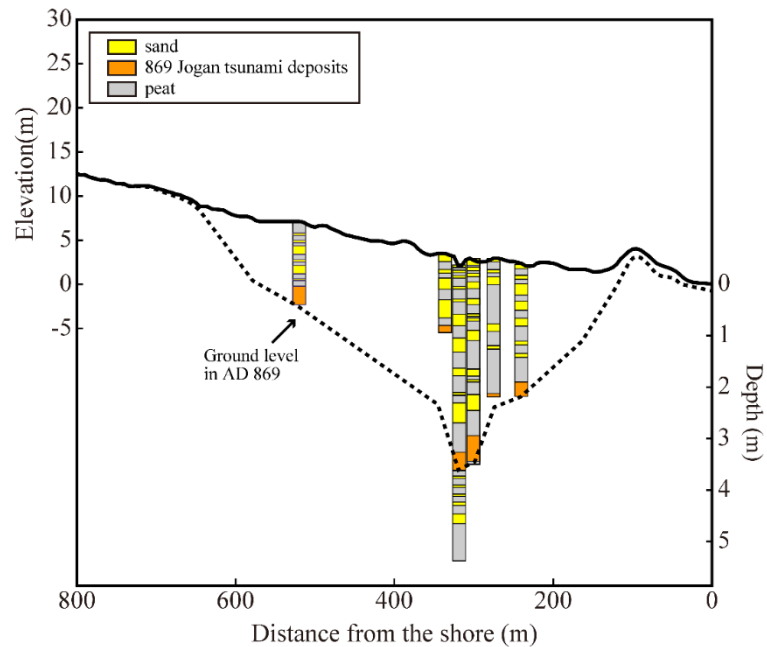


Figure 6-3. Ground surface in the Numanohama marsh in AD 869 inferred from the distribution of base depth of paleo-tsunami deposits (Goto *et al.*, 2015; 2017; 2019).

6-2. Comparison Between Tsunami Inundation Distances and the Maximum Extents of the 869 Jogan Tsunami Deposits

Figure 6-4 shows the maximum tsunami flow depths of the 869 Jogan tsunami calculated from 13 scenarios along topographic profiles in the Idagawa lowland, Sendai plain, and Numanohama marsh. For the Idagawa lowland and Sendai plain, the maximum tsunami heights were about 5-13 m at 1 km offshore, and they suddenly decreased at the back of a coastal forest or beach ridge. However, even if the ridge was the highest, the simulated tsunamis of all models inundated beyond the maximum extents of the 869 tsunami deposits. For the Numanohama marsh, the maximum inundation distances of Models 12 and 13 were shorter than the most inland sampling location. Therefore, it could be concluded that these models are not appropriate as the source of the 869 Jogan tsunami.

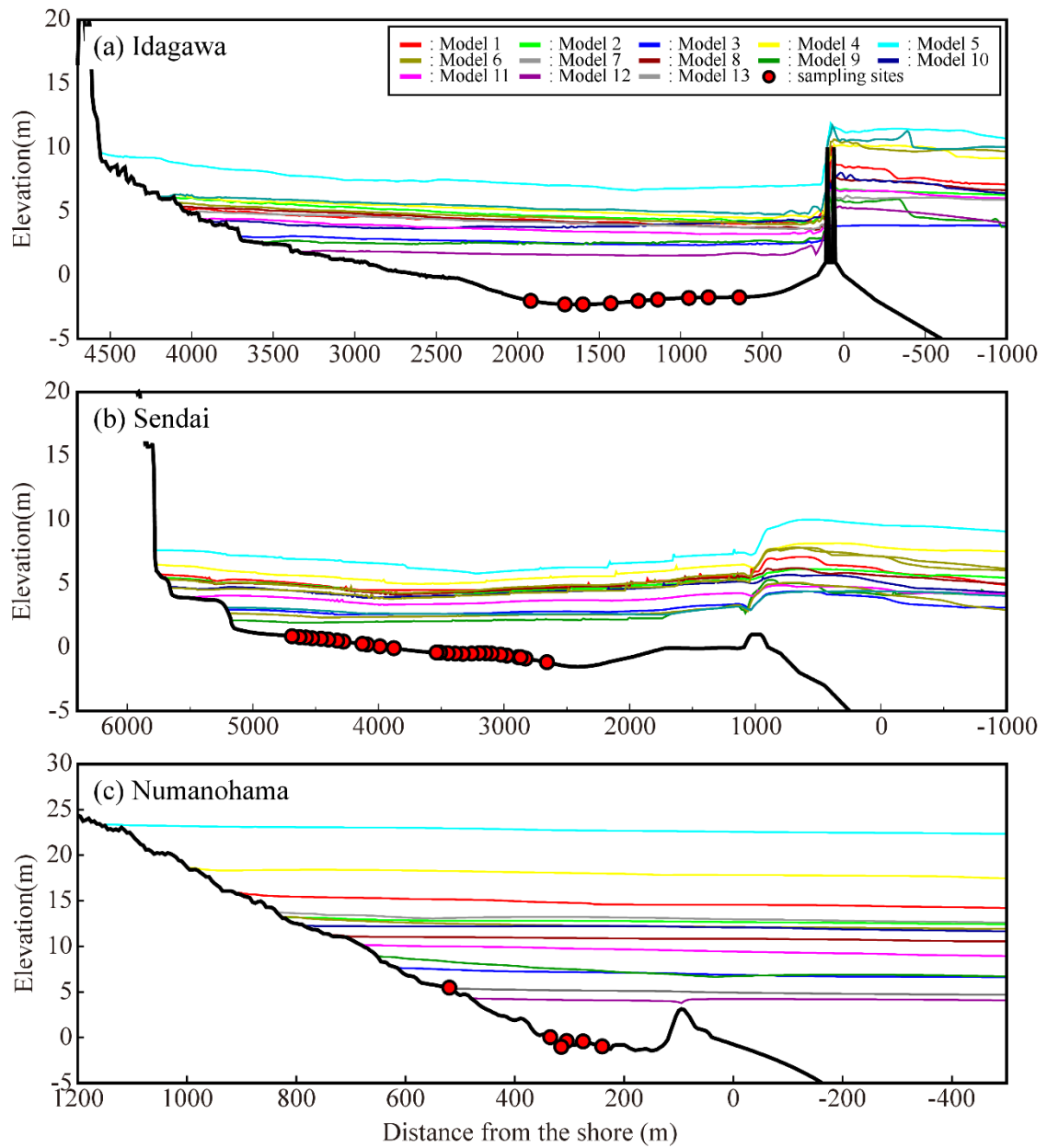


Figure 6-4. Maximum water surfaces for each model along transects in (a) the Idagawa lowland, (b) Sendai plain, and (c) Numanohama marsh. The red dots are sampling locations where the 869 Jogan tsunami deposits were detected in the sediment.

6-3. Uncertainty for Beach Ridge Elevations

The results of multiple scenarios with varying beach ridge elevations but without a coastal forest were compared with the observations (Fig. 6-5). For the Idagawa lowland, the sediment thickness closest to the shoreline could not be reproduced only when the topographic data without a beach ridge was used (Fig. 6-6 and Table 6-1). This is because sand particles carried by the backwash flow deposited behind sand dunes if there was a beach ridge, but they were transported back out to the ocean if there was no beach ridge. As the elevation of the beach ridge became higher, the sediment thickness became thinner. For the Sendai plain, the sediment thickness was thicker landward (Fig. 6-7 and Table 6-2). As the elevation of the beach ridge also became higher, the sediment thickness became thinner.

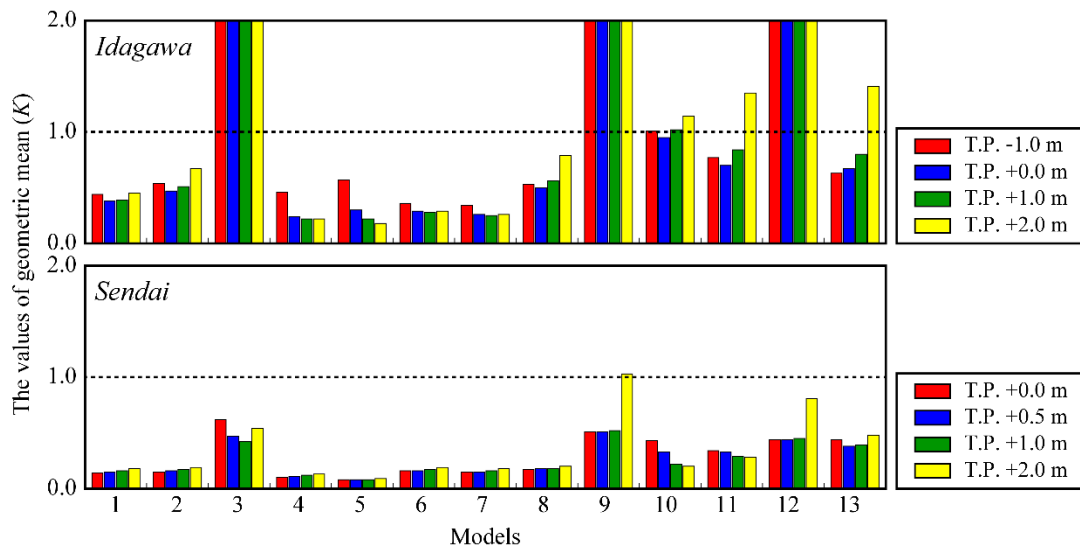


Figure 6-5. The K values for different beach ridge elevations at the Idagawa lowland and Sendai plain.

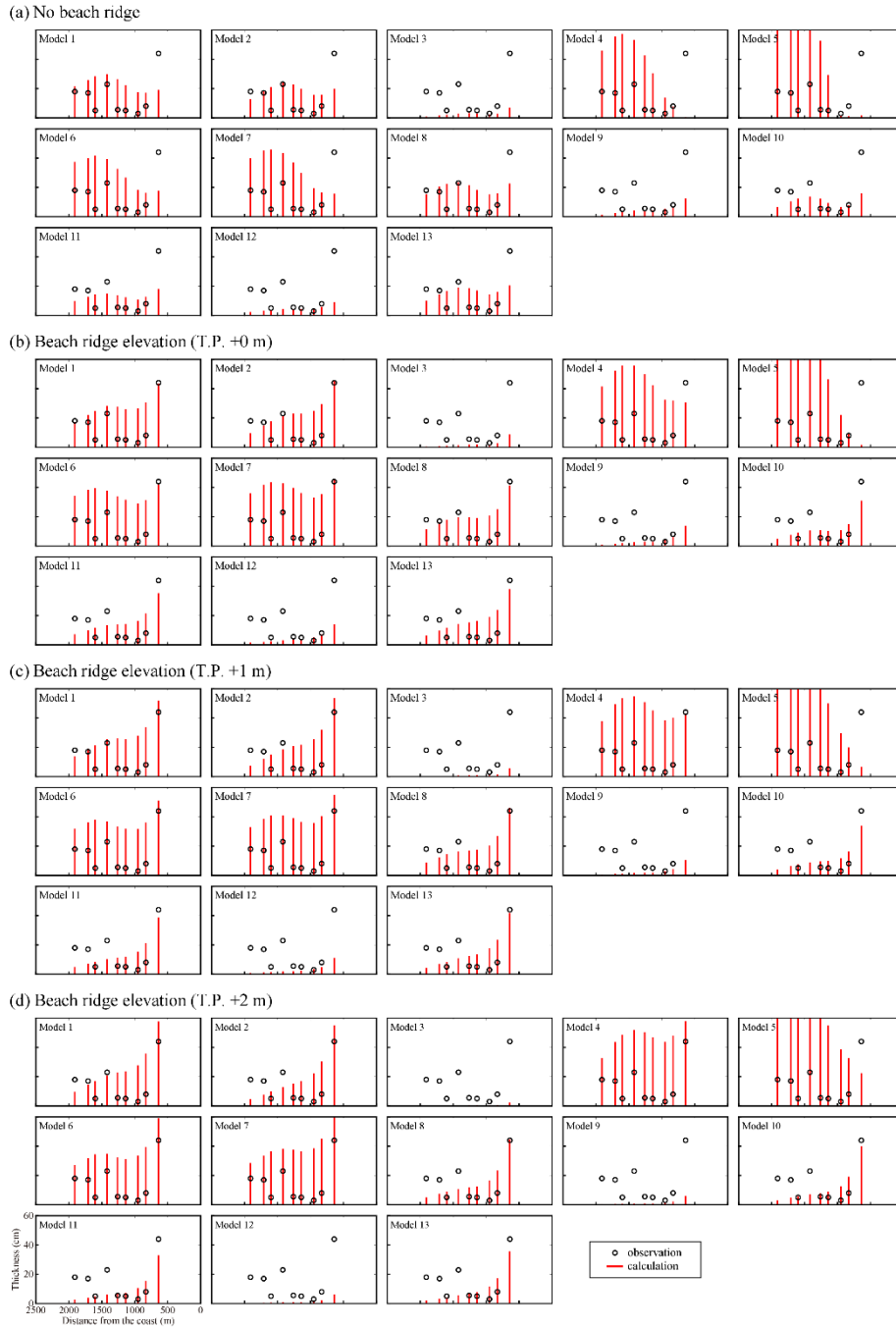


Figure 6-6. The observed (black circles) and simulated (red bars) sediment thickness for different beach ridge elevations in the Idagawa lowland. The K and κ values are shown in Table 6-1.



Figure 6-7. The observed (black circles) and simulated (blue bars) sediment thickness for different beach ridge elevations in the Sendai plain. The K and κ values are shown in Table 6-2.

Figure 6-1. Statistical comparison of the observed and simulated sediment thickness for different beach ridge elevations in the Idagawa lowland.

Models	No beach ridge		Beach ridge (T.P. + 0 m)		Beach ridge (T.P. + 1 m)		Beach ridge (T.P. + 2 m)	
	<i>K</i>	κ	<i>K</i>	κ	<i>K</i>	κ	<i>K</i>	κ
1	0.44	2.33	0.38	2.26	0.39	2.34	0.45	2.52
2	0.54	2.35	0.47	2.47	0.51	2.63	0.67	2.91
3	4.27	2.39	5.71	2.31	7.97	1.95	9.24	2.05
4	0.46	5.77	0.24	2.40	0.22	2.32	0.22	2.30
5	0.57	7.58	0.30	6.05	0.22	3.85	0.18	2.76
6	0.36	2.42	0.29	2.14	0.28	2.12	0.29	2.15
7	0.34	2.56	0.26	2.18	0.25	2.17	0.26	2.20
8	0.53	2.19	0.50	2.26	0.56	2.38	0.79	2.60
9	2.53	2.73	3.36	2.76	4.85	2.60	7.40	2.10
10	1.01	2.09	0.95	2.32	1.02	2.52	1.14	2.84
11	0.77	2.17	0.70	2.38	0.84	2.57	1.35	2.78
12	2.36	2.37	2.77	2.74	4.32	2.67	7.28	2.12
13	0.63	2.33	0.67	2.54	0.80	2.74	1.41	3.10

Table. 6-2. Statistical comparison of the observed and simulated sediment thickness for different beach ridge elevations in the Sendai plain.

Models	Beach ridge (T.P. + 0.0 m)		Beach ridge (T.P. + 0.5 m)		Beach ridge (T.P. + 1.0 m)		Beach ridge (T.P. + 2.0 m)	
	<i>K</i>	κ	<i>K</i>	κ	<i>K</i>	κ	<i>K</i>	κ
1	0.14	4.00	0.15	3.88	0.16	3.71	0.18	3.42
2	0.15	4.06	0.16	3.98	0.17	3.89	0.19	3.57
3	0.62	4.92	0.47	4.42	0.42	3.48	0.54	3.27
4	0.10	3.99	0.11	3.92	0.12	3.84	0.13	3.64
5	0.08	4.07	0.08	4.02	0.08	3.94	0.09	3.87
6	0.16	3.91	0.16	3.85	0.17	3.68	0.19	3.37
7	0.15	3.77	0.15	3.66	0.16	3.52	0.18	3.35
8	0.17	3.97	0.18	3.97	0.18	3.81	0.20	3.62
9	0.51	3.30	0.51	3.32	0.52	3.26	1.03	2.98
10	0.43	5.34	0.33	4.88	0.22	4.31	0.20	3.58
11	0.34	4.66	0.33	4.33	0.29	3.99	0.28	3.34
12	0.44	3.29	0.44	3.35	0.45	3.28	0.81	2.91
13	0.44	3.86	0.38	3.57	0.39	3.39	0.48	3.08

6-4. Comparison with the Observations

Figure 6-8 and Table 6-3 show a comparison of the observed and computed results when the topographic data of a 1 m high beach ridge with/without a coastal forest were used in the Idagawa lowland. The result from Model 1 using topography with a coastal forest was in good agreement with the observations, and the results from Models 2 and 7 roughly match. When the topographic data without a coastal forest was used, the results from Models 10, 11, and 13 were well matched with the observations, and the result from Models 2 and 8 with a 2 m high beach ridge roughly matched (Fig. 6-6 and 6-8, Tables 6-1 and 6-3). This suggests that the presence/absence of a coastal forest has a greater influence on the sediment thickness than the uncertainty of beach ridge elevation. For the Sendai plain, the sediment thickness calculated from Models 1 and 2 were too thick compared with the observations. The results from Models 9 and 12 with a 2 m high beach ridge well reproduced the observations and the result of Model 3 with a 0 m high beach ridge roughly matched (Fig. 6-7 and Table 6-2). However, Models 12 and 13 are judged not to be appropriate based on the comparison between the maximum extent of tsunami deposits and inundation distance in the Numanohama marsh

Summarizing the above results, it can be concluded that no model that satisfies the observations of two study sites is suitable as the 869 Jogan tsunami model, whereas the results of Models 9, 10, and 11 well matched the observations at each study site. In these models, there is a large slip area in the shallow part of the plate interface off Miyagi Prefecture. Thus, the 869 Jogan earthquake may be an earthquake with a major tsunami source off Miyagi Prefecture (Fig. 6-9).

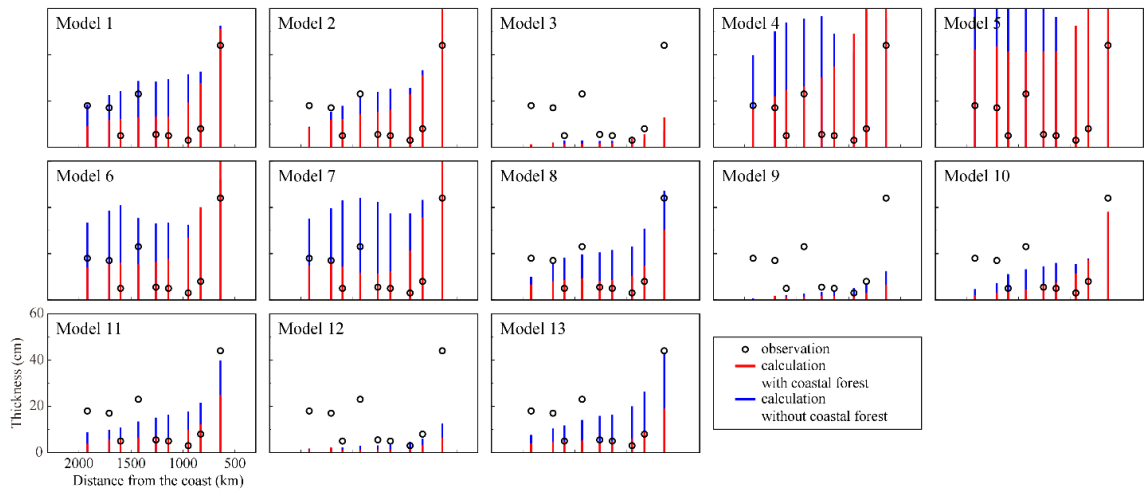


Figure 6-8. Comparison of the observed (black circles) and simulated (red and blue bars) sediment thickness of the 869 Jogan tsunami deposits when the topographic data of a 1 m high beach ridge with/without a coastal forest are used in the Idagawa lowland. The values of K and κ are shown in Table 6-3.

Table 6-3. Statistical comparison of the observed and simulated sediment thickness with/without a coastal forest in the Idagawa lowland

Models	with coastal forest		without coastal forest	
	K	κ	K	κ
1	0.86	2.46	0.39	2.34
2	0.77	2.80	0.51	2.63
3	10.05	2.97	7.97	1.95
4	0.34	2.66	0.22	2.32
5	0.23	2.18	0.22	3.85
6	0.54	2.45	0.28	2.12
7	0.64	2.41	0.25	2.17
8	1.42	2.17	0.56	2.38
9	13.31	2.24	4.85	2.60
10	2.31	3.26	1.02	2.52
11	1.73	2.32	0.84	2.57
12	9.27	2.82	4.32	2.67
13	2.29	2.30	0.80	2.74

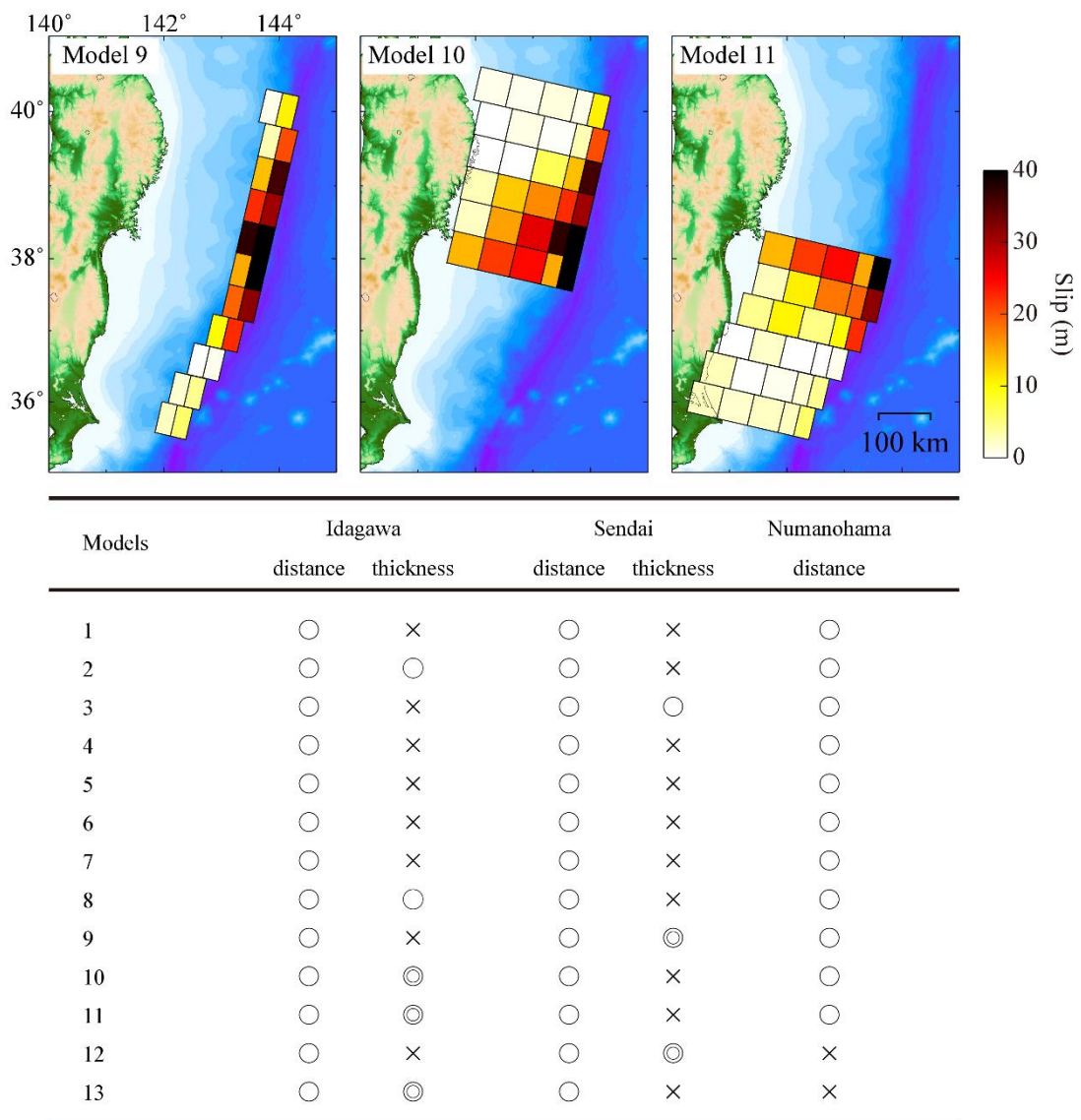


Fig. 6-9 Summary of the comparison between the simulated tsunami inundation distance and sediment thickness and the observation of the 869 Jogan tsunami deposits. The lower table shows the agreement with the observations for each model. The double circles, circles, and crosses indicate good agreement, rough agreement, and no agreement with the observations, respectively.

CHAPTER 7. Conclusions

In this study, I developed a new approach to estimate the magnitude of earthquakes and tsunamis using a combination of modern and historical tsunami deposits and sediment transport simulation to reexamine the great earthquakes along the Japan Trench.

Five tsunami deposits and two storm deposits from the past 3800 years were identified from the tsunami deposit survey of the Idagawa lowland in Fukushima Prefecture. The results of a diatom and nannofossil analysis provide the sedimentary environment at the depositional time of event deposits as well as an indicator to distinguish between tsunami and storm deposits.

The sediment transport modeling with multiple grain sizes adopted in this study provides a more effective and higher sensitivity to constrain initial tsunami source models, compared with the sediment transport modeling with a single grain size and the comparison the maximum extent of tsunami deposit with the computed tsunami inundation distance. The results will also help in the understanding of earthquakes when tsunami deposits have been identified but the magnitude and source location are unknown. However, it should be noted that there is a possibility that this method cannot be applied to tsunami deposits composed of coarse sand particles, like the 2011 Tohoku tsunami deposit of the Numanohama marsh.

The results of analysis of the Idagawa lowland and Sendai plain revealed that sediment transport modeling strongly depends on the presence of a coastal forest. Changes in the sediment thickness due to the presence/absence of a coastal forest were much larger than those due to the uncertainties of beach ridge elevation. Therefore it is necessary to fully consider land use conditions and the vegetation environment at the time of the deposition in order to estimate the magnitude of the earthquake from tsunami deposits.

It is concluded that the 869 Jogan earthquake was an M9-class giant earthquake from

the combination of paleo-tsunami deposits and sediment transport modeling, although the magnitude and fault length were slightly smaller and shorter than those of the 2011 Tohoku earthquake. As a predecessor of the 2011 Tohoku earthquake based on geological evidence in the Idagawa lowland, the 869 Jogan earthquake suggests that the recurrence interval of giant earthquakes is about 1000 years. This finding is not consistent with the evaluation (600 years) previously estimated by the Headquarters for Earthquake Research Promotion. Further studies will be required in order to understand the supercycle of great earthquakes along the Japan Trench.

Acknowledgments

I am greatly indebted to Professor Kenji Satake, Professor Takashi Furumura, Professor Yusuke Yokoyama, Associated professor Ryosuke Ando (University of Tokyo), and Dr. Masanobu Shishikura (Geological Survey of Japan, AIST) for providing valuable and constructive comments. I would like to thank Dr. Takeo Ishibe (Association for the development of earthquake prediction), Dr. Tomoko Goto, Dr. Masaki Yamada, Dr. Yifei Wu, Osamu Sandanbata, and Yuchen Wang (University of Tokyo) for assistant and support during the field surveys. I would also like to thank Professor Toshihiko Sugai (University of Tokyo) for providing variable comments and supporting to grain size analysis. I would also like to thank Professor Minoru Yoneda, Dr. Takayuki Omori, and Dr. Hiromasa Ozaki (The University of Museum, University of Tokyo) for conducting radiocarbon measurements. I would also like to thank Yoshiaki Matsushima for his classification of shells. I would also like to thank Dr. Aditya Riadi Gusman (GNS science) for providing variable comments and supporting to the sediment transport modeling. I would also like to thank Dr. Tomoko Goto for conducting diatom analysis. The CT image scanning (Aquilion PRIME/Focus Edition, Toshiba Medical Systems Corporation, Tochigi, Japan) was performed by Dr. Masaki Yamada under the cooperative research program of the Center for Advanced Marine Core Research, Kochi University (Acceptance No. 17A005). This work was supported by JSPS KAKENHI Grant Numbers JP 24241060 and JP 16H01838. Figures were generated with Generic Mapping Tools (Wessel and Smith, 1998) and a 5 or 10 m Digital Elevation Model was provided by the Geospatial Information Authority of Japan.

References

- Abe, H., Sugeno, Y., Chigama, A. (1990) Estimation of the Height of the Sanriku Jogan 11 Earthquake-Tsunami (A. D. 869) in the Sendai Plain, *Zisin*, **43**, 513-525 (in Japanese, with English Abstract).
- Abe, K. (1979) Size of great earthquakes of 1873–1974 inferred from tsunami data, *Journal of Geophysical Research: Solid Earth*, **84**, 1561–1568.
- Abe, K. (1981) Physical size of tsunamigenic earthquakes of the northwestern Pacific, *Physics of the Earth and Planetary Interiors*, **27**, 194–205.
- Abe, K. (1994) Instrumental magnitudes of historical earthquakes, 1892 to 1898, *Bulletin of the Seismological Society of America*, **84** (2), 415–425.
- Aida, I. (1978) Reliability of a tsunami source model derived from fault parameters, *Journal of Physics of the Earth*, **26** (1), 57–73.
- Ando, K. (1990) Environmental Indicators Based on Freshwater Diatom Assemblages and Its Application to Reconstruction of Paleo-environments, *Annals of The Tohoku Geographical Association*, **42**, 73-88 (in Japanese with English abstract).
- Apotsos, A., Buckley, M., Gelfenbaum, G., Jaffe B., Vatvani, D. (2011a) Nearshore tsunami inundation model validation: toward sediment transport applications, *Pure and Applied Geophysics*, **168**, 2097–2119.
- Apotsos, A., Gelfenbaum, G., Jaffe, B. (2011b) Process-based modeling of tsunami inundation and sediment transport, *Journal of Geophysical Research*, **116**, F01006, <http://dx.doi.org/10.1029/2010JF001797>.
- Apotsos, A., Gelfenbaum G., Jaffe, B., Watt, S., Peck, B., Buckley, M., Stevens, A. (2011c) Tsunami inundation and sediment transport in a sediment-limited embayment on American Samoa, *Earth Science Reviews*, **107**, 1-11.
- Association of Japanese Geographers (2011) Maps of the area hit by the tsunami of 11

March 2011, Northeast Japan. http://danso.env.nagoya-u.ac.jp/20110311/map/index_e.html.

Atwater, B. F. (1987) Evidence for Great Holocene Earthquakes Along the Outer Coast of Washington State, *Science*, **236**, 942-944.

Baba, T., Takahashi, N., Kaneda, Y., Ando, K., Matsuoka, D., Kato, T. (2015) Parallel implementation of dispersive tsunami wave modeling with a nesting algorithm for the 2011 Tohoku tsunami. *Pure and Applied Geophysics*, **172** (12), 3455–3472. <https://doi.org/10.1007/s00024-015-1049-2>.

Benson, B. E., Grimm, K. A., Clague, L. L. (1997) Tsunami Deposits beneath Tidal Marshes on Northwestern Vancouver Island, British Columbia, *Quaternary Research*, **48** (2), 192-204.

Blaauw, M., Christen, J. A. (2011) Flexible paleoclimate age-depth models using an autoregressive gamma process, *Bayesian Analysis*, **6**(4): 457-474.

Bronk Ramsey, C. (2008) Deposition models for chronological records, *Quaternary Science Reviews*, **27** (1–2), 42-60.

Bronk Ramsey, C. (2009) Bayesian analysis of radiocarbon dates, *Radiocarbon*, **51** (1), 337-360.

Bronk Ramsey, C., Staff, R. A., Bryant, C. L., Brock, F., Kitagawa, H., van der Plicht, J., Scholaut, G., Marshall, M. H., Brauer, A., Lamb, H. F., Payne, R. L., Tarasov, P. E., Haraguchi, T., Gotanda, K., Yonenobu, H., Yokoyama, Y., Tada, R., Nakagawa, T. (2012) A complete terrestrial radiocarbon record for 11.2 to 52.8 kyr B.P., *Science*, **338** (6105), 370-374.

Bryant, E. (2014) *Tsunami: The Underrated Hazard*, 3rd ed. Springer (256 pp.).

Central Meteorological Observatory (1933) Sanriku oki Kyoushin oyobi Tsunami Gaihou (Summary Report on the Off the Sanriku Coast Massive Earthquake and Tsunami).

- Chague, J. J., Bobrowsky, P. T. (1994) Evidence for a Large Earthquake and Tsunami 100-400 Years Ago on Western Vancouver Island, British Columbia, *Quaternary Research*, **41**, 176-184.
- Chaumillon, E., Bertin, X., Fortunato, Andre B., Bajo, M., Schneider, Jean-Luc, Dezileau, L., Walsh, J. P., Michelot, A., Chauveau, E., Creach, A., Henaff, A., Sauzeau, T., Waeles, B., Gervais, B., Baumann, J., Jean-Francois, Breilh, Predreros, R. (2017) Storm-induced marine flooding: lessons from a multidisciplinary approach, *Earth Science Review*, **165**, 151–184.
- Committee for field investigation of the Chilean tsunami (1960-1961) Report on the Chilean tsunami of May 24, 1960, as observed along the coast of Japan, Tokyo, Maruzen Co., 397 pp.
- Earthquake Research Institute (1934) Field survey report of damage caused by the 1933 Sanriku earthquake, Bulletin of the Earthquake Research Institute, University Tokyo (supplementary volume), -Papers and Reports on the Tsunami of 1933 on the Sanriku Coast, Japan, **1**, 9–139 (in Japanese).
- Ebina, Y., Takahashi, H. (2014) Description of the 1611 Keicho Oshu earthquake and tsunami in the report by Vizcaino, *Historical Earthquakes*, **29**, 195-207.
- Ebina, Y., Imai, K. (2014) Tsunami traces survey of the 1611 Keicho Ohsyu earthquake tsunami based on historical documents and traditions, *Research Report of Tsunami Engineering*, **31**, 139-148.
- Ebina, Y. (2017) Possibility of the interdisciplinary historical tsunami research based on various historical records - Example of 1611 Keicho Oshu Earthquake and Tsunami -, *Abstract of Japan Geoscience Union Meeting 2017*, MIS09-15.
- Engel, M., Brückner, H. (2011) The identification of palaeo-tsunami deposits – a major challenge in coastal sedimentary research, *Coastline Reports*, **17**, 65–80.

- Folk, R. L., Ward, W. C. (1957) Brazos river bar: a study in the significance of grain size parameters. *Journal of Sedimentary Petrology*, **27**, 3-26.
- Foytong, P., Ruangrassamee, A., Shoji, G., Hiraki, Y., Ezurad, Y. (2013) Analysis of Tsunami Flow Velocities during the March 2011 Tohoku, Japan, Tsunami, *Earthquake Spectra*, **29**, S161-S181.
- Fritz, H. M., Phillips, D. A., Okayasu, A., Shimozono, T., Liu, H., Mohammed, F., Skanavis, V., Synolakis, C. E., Takahashi, T. (2012) The 2011 Japan tsunami current velocity measurements from survivor videos at Kesenuma Bay using LiDAR, *Geophysical Research Letters*, **39**, L00G23, doi:10.1029/2011GL050686.
- Fujiwara, O., Masuda, F., Sakai, T., Fuse, K., Saito, A. (1997) Tsunami Deposits in Holocene Bay-floor Muds and the Uplift History of the Boso and Miura Peninsulas, *The Quaternary Research*, **36** (2), 73-86 (in Japanese, with English Abstract).
- Fujiwara, O., Masuda, F., Sakai, T., Irizuki, T., Fuse, K. (1999) Bay-floor Deposits Formed by Great Earthquakes during the Past 10,000yrs, near the Sagami Trough, Japan, *The Quaternary Research*, **38** (6), 489-501 (in Japanese, with English Abstract).
- Fujiwara, O., Masuda, F., Sakai, T., Irizuki, T., Fuse, K. (2000) Tsunami deposits in Holocene bay mud in southern Kanto region, Pacific coast of central Japan, *Sedimentary Geology*, **135**, 219-230.
- Fujiwara, O. (2004) Sedimentological and paleontological characteristics of tsunami deposits, *The Memoir of the Geological Society of Japan*, **58**, 35-44 (in Japanese, with English Abstract).
- Fujiwara, O., Kamataki, T. (2007) Identification of tsunami deposits considering the tsunami waveform: an example of subaqueous tsunami deposits in Holocene shallow bay on southern Boso Peninsula, central Japan, *Sedimentary Geology*, **200**,

295–313.

Fujiwara, O., Sawai, Y., Shishikura, M., Namegaya, Y. (2012) Sedimentary features of the 2011 Tohoku earthquake tsunami deposits on the central Kujukuri coast, east Japan, *the Quaternary Research*, **51** (2), 117-126 (in Japanese with English abstract).

Fujiwara, O., Ono, E., Yata, T., Umitsu, M., Sato, Y., Heyvaert, Vanessa M. A. (2013) Assessing the impact of 1498 Meio earthquake and tsunami along the Enshu-nada coast, central Japan using coastal geology, *Quaternary International*, **308–309**, 4–12.

Fukuhara, G., Tanioka, Y. (2017) Fault model of the 1611 Keicho Tsunami earthquake (Mw9.0) estimated from historical documents using tsunami inundation simulation, *Abstract of Japan Geoscience Union Meeting 2017*, HDS16-10.

Fukushima Prefecture River Council (2004) Basic Policy of River Improvement in the Miyata River System. (7 pp., in Japanese).

Gelfenbaum, G., Jaffe, B. (2003) Erosion and Sedimentation from the 17 July, 1998 Papua New Guinea Tsunami, *Pure and Applied Geophysics*, **160**, 1969-1999.

Gelfenbaum, G., Vatvani, D., Jaffe, B., Dekker, F. (2007) Tsunami inundation and sediment transport in vicinity of coastal mangrove forest, *Coastal Sediments '07*, **2**, 1117-1128.

Goto, H., and S., Aoyama (2005a) Tsunami Sand Deposits in Lagoon Clay Layers at Iwaki Coast along Japan Trench. Proceedings of the 2005 General Meeting of the Association of Japanese Geographers, **67**, 260 pp. (in Japanese).

Goto, H., and S., Aoyama (2005b) Tsunami Sand Deposits in Lagoon Clay Layers at the northern part of Iwaki Coast along Japan Trench. Abstract of Japan Geoscience Union Meeting 2005. Japan Geoscience Union, Tokyo, J027-P022 (in Japanese, with English abstract).

- Goto, K., Goff, C. C., Fujino, S., Goff, J., Jaffe, B., Nishimura, Y., Richmond, B., Sugawara, D., Szczuciński, W., Tappin, D. R., Witter, R. C., Yulianto, E. (2011) New insights of tsunami hazard from the 2011 Tohoku-oki event, *Marine Geology*, **290**, 46-50.
- Goto, K., Sugawara, D., Abe, T., Haraguchi, T., Fujino, S. (2012) Liquefaction as an important source of the A.D. 2011 Tohoku-oki tsunami deposits at Sendai Plain, Japan, *Geology*, **40** (10), 887-890.
- Gotoh, H., Sobue, K., Arima, H., Ishino, K., Tamai, N., Takezawa, M. (2013) Bulletin of the Faculty of Education, Kagoshima University. Natural science, *Journal of JSCE*, *B2 (Coastal engineering)*, 69 (2), I_1386-I_1390 (in Japanese with English abstract).
- Goto, T., Satake, K., Sugai, K., Ishibe, T., Harada, T., Murotani, S. (2015) Historical tsunami and storm deposits during the last five centuries on the Sanriku coast, Japan, *Marine Geology*, **367**, 105-117.
- Goto, T., Satake, K., Sugai, T., Ishibe, T., Harada, T., Gusman, A. R. (2017) Effects of topography on particle composition of 2011 tsunami deposits on the ria-type Sanriku coast, Japan, *Quaternary International*, **456**, 17-27.
- Goto, T., Satake, K., Sugai, T., Ishibe, T., Harada, T. (2019) Tsunami history over the past 2000 years on the Sanriku coast, Japan, determined using gravel deposits to estimate tsunami inundation behavior, in press.
- Gusman A. R., Tanioka, Y., Takahashi, T. (2012) Numerical experiment and a case study of sediment transport simulation of the 2004 Indian Ocean tsunami in Lhok Nga, Banda Aceh, Indonesia, *Earth Planet Space*, **64**, 817-827.
- Gusman, A. R., Goto, T., Satake, K., Takahashi, T., Ishibe, T. (2018) Sediment transport modeling of multiple grain sizes for the 2011 Tohoku tsunami on a steep coastal

valley of Numanohama, northeast Japan, *Marine Geology*, **405**, 77-91.

Harada K., Aburaya T., Hamzah L., Imamura F. (2000) Discussion about the effect of tide protecting forests to reduce tsunami, *Proceeding of Coastal Engineering, JSCE*, **47**, 366–370 (in Japanese).

Harada, K., Imamura, F. (2003a) Possibility of use for evaluation and disaster mitigation of tsunami damping effect of the tide forests, *Proceeding of Coastal Engineering, JSCE*, **50**, 341-345 (in Japanese).

Harada, K., Imamura, F. (2003b) Evaluation of tsunami reduction by control forest and possibility of its use for mitigation, *Proceeding of coastal engineering, JSCE*, 341-345 (in Japanese).

Harada, K., Kawata, Y. (2004) Study on the effect of Coastal Forest to Tsunami Reduction, *Annual of Disaster Prevention Research Institute, Kyoto University*, No. 47 C.

Harada, K., Kawata, Y. (2005) Study on Tsunami Reduction Effect of Coastal Forest due to Forest Growth, *Annals of Disaster Prevention Research Institute, Kyoto University*, No. 48 C.

Hatori, T. (1975) Tsunami Magnitude and Wave Source Regions of Historical Sanriku Tsunamis in Northeast Japan, *Bulletin of the Earthquake Research Institute, University of Tokyo*, **50** (4), 397-414.

Hatori, T. (1987) Distributions of seismic intensity and tsunami of the 1793 Miyagi-Okai earthquake, Northeastern Japan. *Bulletin of the Earthquake Research Institute, University of Tokyo*, **62**, 297–309 (in Japanese with English abstract).

Hayashi, S., Koshimura, S. (2013) The 2011 Tohoku Tsunami Flow Velocity Estimation by the Aerial Video Analysis and Numerical Modeling, *Journal of Disaster Research*, **8** (4), 561-572.

Hayashi, S., Adriano, B., Mas, E., Koshimura, S. (2014) Improving Tsunami Numerical

Simulation with the Time-Dependent Building Destruction Model, *Journal of Japan Society of Civil Engineers, Ser. B2 (Coastal Engineering)*, **70** (2), I_346-I_350 (in Japanese with English abstract).

Hirakawa, K., Nakamura, Y., Echigo, T. (2000) Large-scale paleo-tsunami along the Pacific Coast of Tokachi Region, *Chikyuu monthly*, **31**, 92-98 (in Japanese).

Imai, K., Imamura, F., Iwama, S. (2013) Advanced Tsunami computation for Urban Regions, *Journal of Japan Society of Civil Engineers, Ser. B2 (Coastal Engineering)*, **69** (2), I_311-I_315 (in Japanese with English abstract).

Inoue, T., Goto, K., Nishimura, Y., Watanabe, M., Iijima, Y., Sugawara, D. (2017) Paleo-tsunami history along the northern Japan Trench: evidence from Noda Village, northern Sanriku coast, Japan, *Progress in Earth and Planetary Science*, 4:42, <https://doi.org/10.1186/s40645-017-0158-1>.

Ishimura, D., Miyauchi, T. (2015) Historical and paleo-tsunami deposits during the last 4000 years and their correlations with historical tsunami events in Koyadori on the Sanriku Coast, northeastern Japan, *Progress in Earth and Planetary Science*, 2:16, <https://doi.org/10.1186/s40645-015-0047-4>.

Ishimura, D. (2017) Re-examination of the age of historical and paleo-tsunami deposits at Koyadori on the Sanriku Coast, Northeast Japan, *Progress in Earth and Planetary Science*, 4:11, <https://doi.org/10.1186/s40562-017-0077-4>.

Ito, A. (2005) Marine Regression During the Historical Time in Sendai Coastal Plain, Northeastern Japan, *Bulletin of the Faculty of Education, Kagoshima University. Natural science*, **57**, 1-8 (in Japanese).

Iwai, J., Takayanagi, Y., Nakagawa, H. (1961) Coastal Region between, Hachinohe and Kuji (Geological Observations of the Sanriku Coastal Region damaged by the Tsunami due to the Chile Earthquake in 1960), *Contributions from the Institute of*

Geology and Paleontology Tohoku University, **52**, 3-15 (in Japanese, with English Abstract).

Jaffe, B. E., Goto, K., Sugawara, D., Richmond, B. M., Fujino, S., Nishimura, Y. (2012) Flow speed estimated by inverse modeling of sandy tsunami deposits: results from the 11 March 2011 tsunami on the coastal plain near the Sendai Airport, Honshu, Japan, *Sedimentary Geology*, **282**, 90-109.

Japan Meteorological Agency (2017) List of the highest tidal levels in history. <https://www.jma.go.jp/jp/choi/list2.html>.

Kakubari, Y., Ota, K., Hoyanagi, K. (2017) Tsunami deposits in the estuary-fill: Holocene drill core in Minamisoma City, Fukushima Prefecture, Northeast Japan, *Journal of Sedimentological Society of Japan*, **75** (2), 73–82 (in Japanese, with English abstract).

Kanamori, H. (1971) Seismological evidence for a lithospheric normal faulting — the Sanriku earthquake of 1933, *Physics of the Earth and Planetary Interiors*, **4**, 289–300.

Kanamori, H. (1972) Mechanism of tsunami earthquakes, *Physics of the Earth and Planetary Interiors*, **6**, 246–259.

Kanamori, H. (1977) The energy release in great earthquakes, *Journal of Geophysical Research*, **82** (20), 2981-2987.

Kansai University (2016) Development of method for tsunami source estimation based on tsunami deposit (218 pp, in Japanese)

Kitamoto, A. (2018) Digital typhoon. <http://www.digital-typhoon.org/>.

Kitamura, N., Kotaka, T., Kataoka, J. (1961) Coastal Region between Ofunato and Shizukawa (Geological Observations of the Sanriku Coastal Region damaged by the Tsunami due to the Chile Earthquake in 1960), *Contributions from the Institute*

of Geology and Paleontology Tohoku University, **52**, 28-40 (in Japanese, with English Abstract).

Koketsu, K., Yokota, Y., Kato, T. (2012) Identification and simulation of seismic supercycles along the Japan Trench including the 2011 Tohoku earthquake, *EGU General Assembly Conference Abstracts*, **14**, 9357.

Komatsubara, J., Fujiwara, O. (2007) Overview of Holocene Tsunami Deposits along the Nankai, Suruga, and Sagami Troughs, Southwest Japan, *Pure and Applied Geophysics*, **164**, 493-507.

Komatsubara, J., Fujiwara, O., Takada, K., Sawai, Y., Aung, T. T., Kamataki, T. (2008) Historical tsunamis and storms recorded in a coastal lowland, Shizuoka prefecture, along the Pacific coast of Japan, *Sedimentology*, **55**, 1703–1716.

Komatsubara, J. (2012) A review on criteria for tsunami deposits recognition in shallow marine sand coastal lowlands from geological records, *Journal of Sedimentological Society of Japan*, **71** (2), 119–127.

Kon'no, E. (1961) Preface and Abstract (Geological Observations of the Sanriku Coastal Region damaged by the Tsunami due to the Chile Earthquake in 1960), *Contributions from the Institute of Geology and Paleontology Tohoku University*, **52**, 1-3 (in Japanese, with English Abstract).

Kortekaas, S., Dawson, A. G. (2007) Distinguishing tsunami and storm deposits: an example from Martinhal, SW Portugal, *Sedimentary Geology*, **200**, 208–221.

Koshimura, S., Hayashi, S. (2012) Tsunami flow measurement using the video recorded during the 2011 Tohoku tsunami attack, *Proceeding international Geoscience and Remote Sensing Symposium (Munich)*, IEEE, 6693-6696, doi: 10.1109/IGARSS.2012.6352063.

Kosugi, M. (1986) Paleocological Analysis Based on Terrestrial Diatoms, and Its

- Implications -Introduction to Japan and Its Prospects-, *Japanese Journal of Historical Botany*, **1**, 29-44 (in Japanese).
- Kosugi, M. (1988) Classification of Living Diatom Assemblages as the Indicator of Environments, and Its Application to Reconstruction of Paleoenvironments, *The Quaternary Research*, **27** (1), 1-20.
- Krumbein, W. C. (1938) Size frequency distributions of sediments and the normal phi curve, *Journal of Sedimentary Petrology*, **8**, 84-90.
- Kunitomi, S. (1933) Off Sanriku earthquake and tsunami on March 3, 1933, *Quarterly Journal of Seismology*, **7**, 111–153 (in Japanese with English abstract).
- Kusumoto, S., Goto, T., Sugai, T., Omori, T., Satake, K. (2018) Geological evidence of tsunamis in the past 3800 years at a coastal lowland in the Central Fukushima Prefecture, Japan, *Marine Geology*, **404**, 137-146.
- Li, L., Huang, Z., Qiu, Q., Natawidjaja, D. H., Sieh, K. (2012) Tsunami-induced coastal change: scenario studies for Painan, West Sumatra, Indonesia, *Earth Planets Space*, **64**, 799-816.
- Lowe, R. L. (1974) Environmental Requirements and pollution tolerance of fresh-water diatoms, *National Environmental Research Center*, 333p.
- Matsumoto, H. (1984) Beach ridge ranges on Holocene coastal plains in northeast Japan the formative factors and periods. *Geographical review of Japan*, **57** ((Ser. A)-10), 720–738 (in Japanese with English abstract).
- Matsumoto, H., Ito, A. (1998) Proceedings of the general meeting of the Association of Japanese Geographers. In: Proceedings of the 1998 General Meeting of the Association of Japanese Geographers, **53**, 392–393 (in Japanese).
- Matsuo, H. (1933) Report on the survey of the 1933 Sanriku tsunami, *Report of the Civil Engineering Laboratory*, **24**, 83–136 (in Japanese).

- Minami-soma City Education Committee, Fukushima Prefecture (2009) Basic Plan for Urajiri Kaizuka Historical Park. (47 pp., in Japanese).
- Minami-soma City Education Committee, Fukushima Prefecture (2010) Urajiri kaizuka. pp. 4 (217 pp., in Japanese).
- Minoura, K., Imamura, F., Sugawara, D., Kono, Y., Iwashita, T. (2001) The 869 Jogan tsunami deposit and recurrence interval of large-scale tsunami on the Pacific coast of northeast Japan, *Journal of Natural Disaster Science*, **23** (2), 83–88.
- Minoura, K., Nakaya, S. (1991) Traces of Tsunami Preserved in InterTidal Lacustrine and Marsh Deposits: Some Examples from Northeast Japan, *Journal of Geology*, **99**, 265-287.
- Minoura, K., Nakaya, S., Sato, H. (1987) Traces of Tsunamis Recorded in Lake Deposits -An Example from Jusan, Shiura-mura, Aomori-, *Zishin*, **40** (2), 183-196 (in Japanese, with English Abstract).
- Minoura, K., Nakaya, S., Uchida, M. (1994) Tsunami deposits in a lacustrine sequence of the Sanriku coast, northeast Japan, *Sedimentary Geology*, **89**, 25-31.
- Miyoshi, H. (1987) True Run-up Heights Reached by the Huge Tsunami of 1896, *Journal of the Oceanographical Society of Japan*, **43**, 159-168 (in Japanese with English abstract).
- Mori, N., Takahashi, T., The 2011 Tohoku Earthquake Tsunami Joint Survey Group (2012) Nationwide post event survey and analysis of the 2011 Tohoku earthquake tsunami. *Coastal Engineering Journal*, **54** (27 pp.).
- Morrison, F. A. (2013) *An Introduction to Fluid Mechanics*, Cambridge University Press.
- Morton, R. A., Gelfenbaum, G., Jaffer, B. E. (2007) Physical criteria for distinguishing sandy tsunami and storm deposits using modern examples, *Sedimentary Geology*,

200, 184–207.

Namegaya, Y., Satake, K., Yamaki, S. (2010) Numerical simulation of the AD 869 Jogan tsunami in Ishinomaki and Sendai plains and Ukedo river-mouth lowland, *Annual Report on Active Fault and Paleoearthquake Researches*, **10**, 1–21 (in Japanese, with English abstract).

Namegaya, Y., Satake, K. (2014) Reexamination of the A.D. 869 Jogan earthquake size from tsunami deposit distribution, simulated flow depth, and velocity, *Geophysical Research Letters*, **41**, 2297-2303.

Namegaya, Y., Yata, T. (2014) Tsunamis which affected the Pacific coast of eastern Japan in medieval times inferred from historical documents, *Zishin*, **66**, 73-81 (in Japanese with English abstract).

Nanayama, F., Shigeno, K., Satake, K., Shimokawa, K., Koitabashi, S., Miyasaka, S., Ishii, M. (2000) Sedimentary differences between the 1933 Hokkaido-nansei-oki tsunami and the 1959 Miyakojima typhoon at Taisei, southwestern Hokkaido, northern Japan, *Sedimentary Geology*, **135**, 255–264.

Nanayama, F., Shigeno, K., Soeda, Y., Furukawa, R., Okahashi, H., Saito, K., Yokoyama, Y., Satake, K., Nakagawa, M. (2003a) Tsunami traces in the 17th century and evaluations of their inundation limits from distribution of event deposits along the southern Tokachi coasts, eastern Hokkaido, northern Japan, *Annual report on active fault and paleoearthquake researches*, **3**, 297-314 (in Japanese, with English Abstract).

Nanayama, F., Satake, K., Furukawa, R., Shimokawa, K., Atwater, B. F., Shigeno, K., Yamaki, S. (2003b) Unusually large earthquakes inferred from tsunami deposits along the Kuril trench, *Nature*, **424**, 660-663.

Nanayama, F., Shigeno, H. (2006) Inflow and outflow facies from the 1993 tsunami in

southwest Hokkaido, *Sedimentary Geology*, **187**, 139-158.

National Police Agency of Japan (2018) Police Countermeasures and Damage Situation associated with 2011Tohoku district - off the Pacific Ocean Earthquake. https://www.npa.go.jp/news/other/earthquake2011/pdf/higaijokyo_e.pdf

Nishimura, Y. (2009) Researches of past earthquakes based on time-space distribution of tsunami deposits. *Zisin* 61, s497–s508 (in Japanese, with English abstract).

Oikawa, K., Takao, M., Usami, M., Miyawaki, R. (2011) Tsunami deposit investigation in the Fukushima coastal area, In: *Abstract of Japan Geoscience Union Meeting 2011 Japan Geoscience Union, Tokyo* (SSS032-P25 in Japanese).

Okada, Y. (1985) Surface displacement due to shear and tensile faults in a half-space, *Bulletin of the Seismological Society of America*, **75** (4), 1135-1154.

Okazaki, H., Ooki, J. (2012) Tsunami Deposits and Coastal Change in Kujukuri Coast at the 2011 Tohoku Earthquake, *Journal of the Natural History Museum and Institute, Chiba*, **12** (1), 1-15 (in Japanese with English abstract).

Onuki, Y., Shibata T., Mii, H. (1961) Coastal Region between Taro and Kamaishi (Geological Observations of the Sanriku Coastal Region damaged by the Tsunami due to the Chile Earthquake in 1960), *Contributions from the Institute of Geology and Paleontology Tohoku University*, **52**, 16-27 (in Japanese, with English Abstract).

Oota, K., Hoyanagi, K. (2014) Study of sedimentary process by facies classification about 3.11 tsunami deposit at Minami-Souma City. In: Abstract of Annual Meeting of the Geological Society of Japan 2011 Joint Annual Meeting of Japan Association of Mineralogical Sciences and the Geological Society of Japan, Ibaraki, (R11-O-1. in Japanese).

Oota, K., Ishizawa, T., Hoyanagi, K. (2017) Formation processes of tsunami deposits

following the 2011 Tohoku-oki earthquake in the estuary of Odaka District, Minamisoma City, Fukushima Prefecture, Northeast Japan, *Journal of Sedimentological Society of Japan*, **76** (1), 3–16.

Peters, R., Jaffe, B. E. (2010) Identification of tsunami deposits in the geologic record: developing criteria using recent tsunami deposits. *In: US Geological Survey Open-File Report*, (2010-1239: 39 pp.).

Ponce, V. M. (1989) *Engineering Hydrology: Principles and Practices*, Prentice Hall.

Reimer, P. J., Bard, E., Bayliss, A., Beck, J. W., Blackwell, P. G., Bronk Ramsey, C., Grootes, P. M., Guilderson, T. P., Hafliðason, H., Hajdas, I., Hattž, C., Heaton, T. J., Hoffmann, D. L., Hogg, A. G., Hughen, K. A., Kaiser, K. F., Kromer, B., Manning, S. W., Niu, M., Reimer, R. W., Richards, D. A., Scott, E. M., Southon, J. R., Staff, R. A., Turney, C. S. M., van der Plicht, J. (2013) IntCal13 and Marine13 radiocarbon age calibration curves 0–50,000 years cal BP, *Radiocarbon*, **55** (4), 1869-1887.

Richmond, B. M., Buckley, M., Etienne, S., Chagué-Goff, C., Clark, K., Goff, J., Dominey-Howes, D., Strotz, L. (2011) Deposits, flow characteristics, and landscape change resulting from the September 2009 South Pacific tsunami in the Samoan islands. *Earth Science Review*, **107**, 38–51.

Richmond B. M., Szczuciński, W., Goff, C. C., Goto, K., Sugawara, D., Witter, R., Tappin, D. R., Jaffe B., Fujino, S., Nishimura, Y., Goff, J. (2012) Erosion, deposition and landscape change on the Sendai coastal plain, Japan, resulting from the March 11, 2011 Tohoku-oki tsunami, *Sedimentary Geology*, **282**, 27-39.

Rubin, C. M., Horton, B. P., Sieh, K., Pilarczyk, J. E., Daly, P., Ismail, N., Parnell, A. C. (2017) Highly variable recurrence of tsunamis in the 7,400 years before the 2004 Indian Ocean tsunami, *Nature, Commun.* **8**, 16019.

- Satake, K. (1995) Linear and Nonlinear Computations of the 1992 Nicaragua Earthquake Tsunami, *Pure and Applied Geophysics*, **144** (3/4), 455-470.
- Satake, K., Fujii, Y., Harada, T., Namegaya, Y. (2013) Time and space distribution of coseismic slip of the 2011 Tohoku earthquake as inferred from tsunami waveform data, *Bulletion of the Seismological Society of America*, 103:2B, 1473–1492. <https://doi.org/10.1785/0120120122>.
- Satake, K., Fujii, T., Yamaki, S. (2017) Different depths of near-trench slips of the 1896 Sanriku and 2011 Tohoku earthquakes, *Geoscience Letters*, 4:33, <https://doi.org/10.1186/s40562-017-0099-y>.
- Satake, K., Nanayama, F., Yamaki, S. (2008) Fault models of unusual tsunami in the 17th century along the Kuril trench, *Earth Planets Space*, **60** (9), 925–935.
- Sato, S., Okayasu, A., Yeh, H., Fritz, H.M., Tajima, Y., Shimozono, T. (2014) Delayed survey of the 2011 Tohoku tsunami in the former exclusion zone in Minami-Soma, Fukushima Prefecture. *Pure and Applied Geophysics*, **171**, 3229–3240.
- Sawai, Y., Okamura, Y., Shishikura, M., Matsu'ura, T., Aung, T. T., Komatsubara, J., Fujii, Y. (2006) Historical tsunamis recorded in deposits beneath Sendai Plain -inundation areas of the A.D. 1611 Keicho and the A.D. 869 Jogan tsunamis-, *Chishitsu News*, **624**, 36-41.
- Sawai, Y., Shishikura, M., Okamura, Y., Takada, K., Matsu'ura, T., Aung, T. T., Komatsubara, J., Fujii, Y., Fujiwara, O., Satake, K., Kamataki, T., Sato, N. (2007) A study on paleotsunami using handy geoslicer in Sendai Plain (Sendai, Natori, Iwanuma, Watari, and Yamamoto), Miyagi, Japan. In: Annual Report on Active Fault and Paleoeearthquake Researches, **7**, 47–80 (in Japanese with English abstract).
- Sawai, Y., Fujii, Y., Fujiwara, O., Kamataki, T., Komatsubara, J., Okamura, Y., Satake, K., Shishikura, M. (2008) Marine incursions of the past 1500 years and evidence of

tsunamis at Sujin-numa, a coastal lake facing the Japan Trench, *The Holocene*, **18** (4), 517-528.

Sawai, Y., Namegaya, Y., Okamura, Y., Satake, K., Shishikura, M. (2012a) Challenges of anticipating the 2011 Tohoku earthquake and tsunami using coastal geology, *Geophysical Research Letter*, **39**, L21309, doi:10.1029/2012GL053692.

Sawai, Y., Shishikura, M., Namegaya, Y., Fujii, Y., Miyashita, Y., Kagohara, K., Fujiwara, O., Tanigawa, K. (2012b) Diatom assemblages in tsunami deposits in a paddy field and on paved roads from Ibaraki and Chiba Prefectures, Japan, generated by the 2011 Tohoku tsunami, *Diatom*, **28**, 19-26.

Sawai, Y., Namegaya, Y., Tamura, T., Nakashima, R. (2015) Shorter intervals between great earthquakes near Sendai: scour ponds and a sand layer attributable to AD 1454 overwash, *Geophysical Research Letter*, **42**, 4795–4800.

Shields, A. (1936) Application of Similarity Principles and Turbulence Research to Bedload Movement, Hydrodynamics Laboratory, California Institute of Technology Pasadena Publication No. 167.

Shinozaki, T., Fujino, S., Ikehara, M., Sawai, Y., Tamura, T., Goto, K., Sugawara, D., Abe, T. (2015) Marine biomarkers deposited on coastal land by the 2011 Tohoku-oki tsunami, *Nature Hazards*, **77**, 445-460.

Shishikura, M., Echigo, T., Kaneda, H. (2007) Marine reservoir correction for the Pacific coast of central Japan using ^{14}C ages of marine mollusks uplifted during historical earthquake, *Quaternary Research*, **67**, 286-291.

Shishikura, M., Sawai, Y., Okamura, Y., Komatsubara, J., Aung, T. T., Ishiyama, T., Fujiwara, O., Fujino, S. (2007) Age and distribution of tsunami deposit in the Ishinomaki Plain, Northeastern Japan. *Annual Report on Active Fault and Paleoseismicity Researches*, **7**, 31–46 (in Japanese, with English abstract).

- Shuto, N. (1985) Effectiveness and limit of tsunami control forests, *Proceedings of Coastal Engineering, JSCE*, **32**, 465-469 (in Japanese).
- Shuto, N. (2007) Damage and Reconstruction at Okushiri Town Caused by the 1993 Hokkaido Nansei-oki Earthquake Tsunami, *Journal of Disaster Research*, **2** (1), 44-49.
- Soulsby, R. (1997) Dynamics of marine sand, Thomas *Telford Publications, London*, 270pp.
- Soulsby, R. L., Whitehouse, R. J. S. (1997) Threshold of sediment motion in coastal environments. In: Pacific Coasts and Ports '97: Proceedings of the 13th Australasian Coastal and Ocean Engineering Conference and the 6th Australasian Port and Harbour Conference, 1. Centre for Advanced Engineering, University of Canterbury, pp. 145.
- Sugawara, D., Minoura, K., Imamura, F. (2001) Sedimentation associated with the AD 869 Jogan tsunami and its numerical reconstruction, *Research Report of Tsunami Engineering*, **18**, 1-10.
- Sugawara, D., Goto, K., Imamura, F., Matsumoto, H., Minoura, K. (2012) Assessing the magnitude of the 869 Jogan tsunami using sedimentary deposits: Prediction and consequence of the 2011 Tohoku-oki tsunami, *Sedimentary Geology*, **282**, 14-26.
- Sugawara, D., Goto, K., Jaffe, B. E. (2014a) Numerical models of tsunami sediment transport — Current understanding and future directions, *Marine Geology*, **352**, 295-320.
- Sugawara, D., Takahashi, T., Imamura, F. (2014b) Sediment transport due to the 2011 Tohoku-oki tsunami at Sendai: Results from numerical modeling, *Marine Geology*, **358**, 18-37.
- Szczuciński, W., Kokociński, M., Rzeszewski, M., Goff, C. C., Cachão, M., Goto, K.,

- Suagwara, D. (2012) Sediment sources and sedimentation processes of 2011 Tohoku-oki tsunami deposits on the Sendai Plain, Japan — Insights from diatoms, nannoliths and grain size distribution, *Sedimentary Geology*, **282**, 40-56.
- Takada, K., Shishikura, M., Imai, K., Ebina, Y., Goto, K., Koshiya, S., Yamamoto, H., Igarashi, A., Ichihara, T., Kinoshita, H., Ikeda, T., River Division Department of prefectural Land Development, Iwate Prefecture Government. (2016) Distribution and ages of tsunami deposits along the Pacific Coast of the Iwate Prefecture, *Annual Report on Active Fault and Paleoearthquake Researches*, **16**, 1-52.
- Takahashi, T., Imamura, F., Shuto, N. (1992) Development of tsunami calculation method with sediment transport, *Proceeding of Coastal Engineering*, **39**, 231-235 (in Japanese).
- Takahashi, T., Imamura, F., Shuto, N. (1993) Applicability and reproducibility of tsunami sediment transport model, *Proceeding of Coastal Engineering*, **40**, 171-175 (in Japanese).
- Takahashi, T., Shuto N., Imamura, F., Asai D. (1999) A movable bed model for tsunamis with exchange rate between bed load layer and suspended layer, *Proceeding of Coastal Engineering*, **46**, 606–610 (in Japanese).
- Takahashi, T., Shuto, N., Imamura, F., Asai, D. (2000) Modeling sediment transport due to tsunamis with exchange rate between bed load layer and suspended load layer 2000, *Proceedings of International Conference of Coastal Engineering*, 1508–1519.
- Takahashi, J., Goto, K., Oie, T., Yanagisawa, H., Imamura, F. (2008) Inundation and topographic Change due to the 2004 Indian Ocean Tsunami at the Kirinda port, Sri Lanka, *Journal of Hydraulic Engineering*, **55**, 251-255 (in Japanese, with English Abstract).
- Takahashi, T., Kurokawa, T., Fujita, M., Shimada, H. (2011) Hydraulic Experiment on

Sediment Transport due to Tsunamis with Various Sand Grain Size, *Journal of JSCE, B2 (Coastal engineering)*, **67** (2), 231-235.

Tanaka, H., Yoshitake, Y., Shuto, N. (1989) Numerical simulation of bottom deposit classification in wave and flow coexisting field, *Proceeding of Coastal Engineering*, **36**, 264–268 (in Japanese).

Tang, H., Weiss, R. (2015) A model for tsunami flow inversion from deposits (TSUFLIND), *Marine Geology*, **370**, 55-62.

Tanioka, Y., Satake, K. (1996a) Fault parameters of the 1896 Sanriku tsunami earthquake estimated from tsunami numerical modeling. *Geophysical Research Letter*, **23**, 1522–1549.

Tanioka, Y., Satake, K. (1996b) Tsunami generation by horizontal displacement of ocean bottom, *Geophysical Research Letters*, **28** (17), 3389-3392.

The Headquarters for Earthquake Research Promotion, MEXT, Japan (2006) Research report of High-priority Observation and Survey on Miyagi-oki Earthquakes, 2005 fiscal year, 89 pp. (in Japanese).

The Headquarters for Earthquake Research Promotion, MEXT, Japan (2007) Research report of High-priority Observation and Survey on Miyagi-oki Earthquakes, 2006 fiscal year, 112 pp. (in Japanese).

The Headquarters for Earthquake Research Promotion, MEXT, Japan (2008) Research report of High-priority Observation and Survey on Miyagi-oki Earthquakes, 2007 fiscal year, 166 pp. (in Japanese).

The Headquarters for Earthquake Research Promotion, MEXT, Japan (2009) Research report of High-priority Observation and Survey on Miyagi-oki Earthquakes, 2008 fiscal year, 157 pp. (in Japanese).

The Headquarters for Earthquake Research Promotion, MEXT, Japan (2010) Research

report of High-priority Observation and Survey on Miyagi-oki Earthquakes, 2009 fiscal year, 171 pp. (in Japanese).

Tokyo Electric Power Company Holdings (2012) Report for the Fukushima Nuclear Accident. (352 pp., in Japanese).

Tsuji, Y., Satake, K., Ishibe, T., Kusumoto, S., Harada, T., Nishiyama, A., Kim, Y.H., Ueno, T., Murotani, S., Oki, S., Sugimoto, M., Tomari, J., Heidarzadeh, M., Watada, S., Imai, K., Choi, B.H., Yoon, S.B., Bae, J.S., Kim, K.O., Kim, H.W. (2011) Field Surveys of tsunami heights from the 2011 off the Pacific Coast of Tohoku, Japan Earthquake, *Bulletin of the Earthquake Research Institute, University of Tokyo*, **86**, 29–279 (in Japanese with English abstract).

Tsuji, Y., Satake, K., Ishibe, T., Harada, T., Nishiyama, A., Kusumoto, S. (2014) Tsunami Heights along the Pacific Coast of Northern Honshu Recorded from the 2011 Tohoku and Previous Great Earthquakes, *Pure and Applied Geophysics*, **171**, 3183–3215.

Tuttle, M. P., Ruffman, A., Anderson, T., Jeter, H. (2004) Distinguishing tsunami from storm deposits in eastern North America: the 1929 Grand Banks tsunami versus the 1991 Halloween storm, *Seismological Research Letter*, **7**, 117–131.

Unohana, M., Ota, T. (1988) Disaster records of Meiji Sanriku tsunami by Soshin Yamana, Research Report of the Tsunami Disaster Prevention Laboratory, Faculty of Civil Engineering, Tohoku University, **5**, 57–379 (in Japanese).

Usami, T. (1966) Descriptive table of major earthquakes in and near Japan which were accompanied by damages, *Bulletin of the Earthquake Research Institute, University of Tokyo*, **44**, 1571–1622 (in Japanese).

Usami, T. (2003) Catalog of Damaging Earthquakes in the World (through 1989). (Tokyo, 243 pp., in Japanese).

- Usami, T. (2003) Materials for Comprehensive List of Destructive Earthquakes in Japan, [416]-2001, *University of Tokyo Press*, 605 pp. (in Japanese).
- Utsu, T. (1979) Seismicity of Japan from 1885 through 1925, *Bulletin of the Earthquake Research Institute, University of Tokyo*, **54** (2), 253–308.
- Utsu, T. (1990) Materials for Comprehensive List of Destructive Earthquakes in Japan, [416]-2001. University of Tokyo Press (605 pp., in Japanese).
- Utsu, T. (1994) Aftershock activity of the 1896 Sanriku earthquake, *Zisin*, **47** (1), 89–92 (in Japanese).
- van Rijn, L.C. (1984a) SEDIMENT TRANSPORT, PART I: BED LOAD TRANSPORT, *Journal of Hydraulic Engineering*, **110**, 1431-1456.
- van Rijn, L.C. (1984b) SEDIMENT TRANSPORT, PART II: SUSPENDED LOAD TRANSPORT, *Journal of Hydraulic Engineering*, **110**, 1613-1641.
- van Rijn, L.C. (1993) Principles of sediment transport in rivers, estuaries and coastal areas, *Aqua Publications, Amsterdam*.
- Watanabe, A., Maruyama, Y., Shimizu, T., Sakakiyama, T. (1984) Numerical prediction model of three-dimensional beach transformation due to installed structures, *Proceeding of Coastal Engineering*, **31**, 406-410 (in Japanese).
- Watanabe, H. (2000) The source area of the 869 Jogan Tsunami, *Research Report of Tsunami Engineering*, **17**, 27-37. (in Japanese).
- Watanabe, H. (2001) Is it possible to clarify the real state of past earthquakes and tsunamis on the basis of legends? As an example of the 869 Jogan earthquake and tsunami, *Rekishi-Zishin*, **17**, 130–146.
- Watanabe, M., Bricker, J. D., Goto, K., Imamura, F. (2017) Factors responsible for the limited inland extent of sand deposits on Leyte Island during 2013 Typhoon Haiyan, *Journal of Geophysical Research: Oceans*, **122**, 2795–2812,

doi:10.1002/2016JC012023

- Watanabe, M., Goto, K., Bricker, J. D., Imamura, F. (2018) Are inundation limit and maximum extent of sand useful for differentiating tsunamis and storms? An example from sediment transport simulations on the Sendai Plain, Japan, *Sedimentary Geology*, **364**, 204–216.
- Wentworth, C. K. (1922) A scale of grade and class terms for clastic sediments, *The Journal of Geology*, **30**, 377-392.
- Wessel, P., Smith, W. H. F. (1998) New, improved version of the generic mapping tools released, *Eos. Transactions, American Geophysical Union*, **79** (47), 579, <https://doi.org/10.1029/98EO00426>.
- Yamada, M., Fujino, S. (2013) Sedimentary characteristics of the onshore tsunami deposits formed by the 2011 Tohoku-oki tsunami in coastal lowlands, Ibaraki and Chiba prefectures, *Journal of Sedimentological Society of Japan*, **72** (1), 13-25 (in Japanese with English abstract).
- Yamana, S. (1896) Disaster records of Meiji Sanriku tsunami, reproduced by Unohana and Ota (1988), Research Report of the Tsunami Disaster Prevention Laboratory, *Faculty of Civil Engineering, Tohoku University*, **5**, 57–379 (in Japanese).
- Yoneda, M., Uno, H., Shibata, Y., Suzuki, R., Kumamoto, Y., Yoshida, K., Sasaki, T., Kawahata, H. (2007) Radiocarbon marine reservoir ages in the western Pacific estimated by pre-bomb molluscan shells, *Nuclear Instruments and Methods in Physics Research*, **B:259**, 432–437.